

University of Nebraska - Lincoln

DigitalCommons@University of Nebraska - Lincoln

---

Mechanical (and Materials) Engineering --  
Dissertations, Theses, and Student Research

Mechanical & Materials Engineering,  
Department of

---

Fall 10-2019

## SMART ADDITIVE MANUFACTURING: IN-PROCESS SENSING AND DATA ANALYTICS FOR ONLINE DEFECT DETECTION IN METAL ADDITIVE MANUFACTURING PROCESSES

Mohammad Montazeri

University of Nebraska - Lincoln, [mmontazeri@huskers.unl.edu](mailto:mmontazeri@huskers.unl.edu)

Follow this and additional works at: <https://digitalcommons.unl.edu/mechengdiss>



Part of the [Materials Science and Engineering Commons](#), and the [Mechanical Engineering Commons](#)

---

Montazeri, Mohammad, "SMART ADDITIVE MANUFACTURING: IN-PROCESS SENSING AND DATA ANALYTICS FOR ONLINE DEFECT DETECTION IN METAL ADDITIVE MANUFACTURING PROCESSES" (2019). *Mechanical (and Materials) Engineering -- Dissertations, Theses, and Student Research*. 148. <https://digitalcommons.unl.edu/mechengdiss/148>

This Article is brought to you for free and open access by the Mechanical & Materials Engineering, Department of at DigitalCommons@University of Nebraska - Lincoln. It has been accepted for inclusion in Mechanical (and Materials) Engineering -- Dissertations, Theses, and Student Research by an authorized administrator of DigitalCommons@University of Nebraska - Lincoln.

SMART ADDITIVE MANUFACTURING:  
IN-PROCESS SENSING AND DATA ANALYTICS  
FOR ONLINE DEFECT DETECTION IN  
METAL ADDITIVE MANUFACTURING PROCESSES

by

Mohammad Montazeri

A DISSERTATION

Presented to the Faculty of  
The Graduate College at the University of Nebraska  
In Partial Fulfillment of Requirements  
For the Degree of Doctor of Philosophy

Major: Engineering  
(Materials Engineering)

Under the Supervision of Prahalada Rao, Ph.D.

Lincoln, Nebraska

October 2019

SMART ADDITIVE MANUFACTURING  
IN-PROCESS SENSING AND DATA ANALYTICS FOR ONLINE DEFECT  
DETECTION IN METAL ADDITIVE MANUFACTURING PROCESSES

Mohammad Montazeri, Ph.D.

University of Nebraska, 2019

Advisor: Prahalada Rao

The goal of this dissertation is to detect the incipient flaws in metal parts made using additive manufacturing processes (3D printing). The key idea is to embed sensors inside a 3D printing machine and conclude whether there are defects in the part as it is being built by analyzing the sensor data using artificial intelligence (machine learning). This is an important area of research, because, despite their revolutionary potential, additive manufacturing processes are yet to find wider acceptance in safety-critical industries, such as aerospace and biomedical, given their propensity to form defects. The presence of defects, such as porosity, can afflict as much as 20% of additive manufactured parts. This poor process consistency necessitates an approach wherein flaws are not only detected but also promptly corrected inside the machine. This dissertation takes the critical step in addressing the first of the above, i.e., detection of flaws using in-process sensor signatures.

Accordingly, the objective of this work is to develop and apply a new class of machine learning algorithms motivated from the domain of spectral graph theory to analyze the in-process sensor data, and subsequently, detect the formation of part defects. Defects in additive manufacturing originate due to four main reasons, namely, material, process parameters, part design, and machine kinematics. In this work, the efficacy of the graph theoretic approach is determined to detect defects that occur in all the above four contexts. As an example, in Chapter 4, flaws such as lack-of-fusion porosity due to poor choice of process parameters in additive manufacturing are identified with statistical accuracy exceeding 80%. As a comparison, the accuracy of existing conventional statistical methods is less than 65%.



This research is funded by the following grant awarded to the dissertation adviser,  
Dr. Prahalada Rao, from the United States National Science Foundation (NSF).

**NSF CMMI 1752069**

*CAREER: Smart Additive Manufacturing  
Fundamental Research in Sensing, Data Science, and Modeling Toward Zero Part Defects.*

This student (Mohammad Montazeri) also appreciates the travel grant awarded by the  
NSF to present a part of his work from this dissertation at the  
2018 ASME Manufacturing Science and Engineering Conference (MSEC 2018).

## Table of Contents

---

1	Introduction	1
1.1	Goal, Objective, and Hypothesis	1
1.2	Overview of the Additive Manufacturing Technology	4
1.2.1	Introduction to Powder Bed Fusion and Directed Energy Deposition	7
1.2.2	Motivation of the Research	10
1.2.3	Defects in Metal AM	12
1.2.4	Analytical Methods for Process Monitoring in Metal AM	17
1.3	Contribution of the Graph Theoretical Approach	22
1.4	Structure of the Dissertation	25
2	Build Condition Monitoring in LPBF	32
2.1	Goal, Objective, and Hypothesis	32
2.2	Prior Work and Challenges in Sensor-Based Monitoring in LPBF	35
2.2.1	Melt pool Monitoring Systems in PBF	36
2.2.2	Layer-Wise Imaging or Staring Configuration Systems in PBF	38
2.3	Experimental Setup and Data Acquisition	41
2.3.1	Measurement System and Test Artifact	41
2.3.2	Visualization of the Representative Data Acquired	45
2.4	Proposed Methodology	49
2.4.1	Previous Work in Spectral Graph Theory	49
2.4.2	Overview of the Approach	51
2.4.3	Application of the Approach to Synthetically Generated Signals.	62
2.5	Results and Discussions	65
2.6	Conclusions	70
3	Detecting Material Contamination in LPBF	73
3.1	Goal, Objective, and Hypothesis	73
3.2	Prior Work and Challenges in Material Contamination in LPBF	76
3.3	Experimental Setup and Data Acquisition	82
3.3.1	Experimental Procedure	82
3.3.2	Sensor Integration and In-Process Data Acquisition	89

3.4	Proposed Methodology	91
3.4.1	Overview of the Approach	91
3.4.2	Applying Spectral Graph Theory to the LPBF Photodetector data	94
3.5	Results and Discussion	103
3.5.1	Offline X-Ray Computed Tomography Analysis of the Build	103
3.5.2	Online Spectral Graph-Theoretic Analysis of the Signal	107
3.5.3	Verification with Statistical Time Series Analysis	115
3.5.4	Consistency Between Spectral Graph Theory and XCT	117
3.6	Conclusions	119
4	Detecting Lack-of-Fusion Porosity in LPBF	121
4.1	Goal, Objectives, and Hypothesis	121
4.2	Prior Work and Challenges at Optical Spectroscopy in LPBF	122
4.3	Experimental Setup and Data Acquisition	124
4.3.1	Part Build Conditions	124
4.3.2	Sensor Instrumentation	127
4.3.3	X-Ray Computed Tomography (XCT) of Test Parts	128
4.4	Proposed Methodology	133
4.5	Results and Discussion	144
4.5.1	Quantifying Porosity from X-Ray Computed Tomography (XCT)	144
4.5.2	Visualization of Sensor Data	146
4.5.3	Classifying the Severity of Pores into Discrete Levels	147
4.5.4	Estimating the Value of the Normalized Porosity Level	152
4.6	Conclusions	153
5	Detecting Lack-of-Fusion Porosity in DED	155
5.1	Goal, Objective, and Hypothesis	155
5.2	Prior Work and Challenges in In-process Sensing in DED	157
5.3	Experimental Setup and Data Acquisition	164
5.3.1	Experimental Test Conditions	164
5.3.2	In-Process Heterogeneous Sensor Setup and Data Acquisition	166
5.4	Proposed Methodology	169

5.5	Results and Discussion	174
5.5.1	Offline Statistical Analysis of Porosity from XCT Slices	174
5.5.2	Online Detection of Defects from In-Process Sensor Data	179
5.6	Conclusions	182
6	Conclusions and Future Work	185
6.1	Research Summary	185
6.2	Future Work	189
	References	191

## List of Figures

---

Figure 1-1: The five fundamental aspects of smart additive manufacturing.	2
Figure 1-2: The schematic of the laser powder bed fusion (LPBF) process.	7
Figure 1-3: A schematic of a powder feed directed energy deposition (DED) process.	8
Figure 1-4: Example of process inconsistency in laser powder bed fusion.	10
Figure 1-5: Illustration of the four major causes of defects in metal AM parts.	14
Figure 1-6: X-ray Computed Tomography of a titanium alloy DED part at different layers showing presence of systematic and random (stochastic) flaws.	30
Figure 2-2: Schematic layout of sensors installed on the LPBF machine at NIST.	42
Figure 2-3: The part schematic with 40.5° overhang angle.	45
Figure 2-4: Distinctive melt pool shape for bulk and overhang areas.	46
Figure 2-5: Two representative high-speed video images taken during the process.	47
Figure 2-6: Photodetector signal windows for the overhang and bulk features.	48
Figure 2-7: The three steps in the proposed spectral graph-theoretic approach.	53
Figure 2-8: The four different Rössler systems used for testing the approach.	63
Figure 2-9: Fiedler number pattern for the various signals.	67
Figure 3-1: Optical image of an etched and polished Inconel 625 specimen showing the effect of contamination.	74
Figure 3-2: The schema used for introducing contamination during the build.	86
Figure 3-3: A schematic of the open architecture LPBF platform at EWI.	87
Figure 3-4: Post recoating optical images after tungsten contamination under different conditions.	88
Figure 3-5: The horizontal and vertical hatch patterns implemented during the printing process.	90
Figure 3-6: Graphical overview of the proposed spectral graph-theoretic approach.	93
Figure 3-7. Three-dimensional reconstruction of the XCT scan image for the specimen contaminated with tungsten powder particles.	103
Figure 3-8. The cross sectional XCT views of the Inconel 625 specimen contaminated by the tungsten particles.	105
Figure 3-9: The microstructure of the inconel 625 specimen contaminated with tungsten particles.	106

Figure 3-10: The cross-sectional views of the Inconel 625 specimen contaminated by the Aluminum powder particles.	107
Figure 3-11: The photodetector signal associated with the six levels of contamination.	109
Figure 3-12: The Phase 1 spectral Hotelling $T^2$ control chart related to six levels of contamination.	111
Figure 3-13: The Phase 2 spectral Hotelling $T^2$ control chart applied to two replications of the data for the remaining two iterations, for each of the six levels of contamination.	113
Figure 3-14: (a) The color coded $T^2$ values of the spectral graph Fourier coefficients.	118
Figure 4-1: The relative location of the discs A through E on the build platen.	125
Figure 4-2: The five discs used for analysis in this work.	126
Figure 4-3: Schematic of the multispectral sensor installed within the AM machine.	127
Figure 4-4: Image processing steps to extract the porosity from XCT slices.	129
Figure 4-5: Illustration of the approach taken to window the signal.	135
Figure 4-6: The pore extraction procedure as applied to the XCT.	145
Figure 4-7: The probability mass functions for three different porosity metrics.	146
Figure 4-8: The distribution of 50,000 randomly selected measurements of the line-to-continuum ratio for one layer (layer 60) of Disc A through D.	147
Figure 4-9: The actual vs. predicted normalized porosity levels ( $\mu$ ) along the whole dataset using the graph Fourier coefficients (method 2).	152
Figure 5-1: The XCT scans at the same layer for ten selected printing conditions.	165
Figure 5-2: The image of the spectrometer and plume camera integrated into the DED machine.	166
Figure 5-3: the probability distributions of the sensor signatures.	168
Figure 5-4: The image processing steps for the extraction of pores from XCT slices.	175
Figure 5-5: The flaws extracted from the XCT.	177
Figure 5-6: Main effects plots each DED process parameter.	177

## List of Tables

---

Table 1-1: Comparison between LPBF and DED processes.	9
Table 1-2: Classification of defects in metal additive manufacturing processes.	13
Table 1-3: Overview of the analytical approaches in metal AM.	18
Table 1-4: The categories used for analyzing the fidelity of defect detection.	25
Table 2-1: The information related to all sensors used in the LPBF process.	43
Table 2-2: Scanning parameters in the LPBF of the overhang structure.	44
Table 2-3: List of major mathematic symbols and notations used in this work.	55
Table 2-4: Evaluation of the proposed approach for the Rössler system.	64
Table 2-5: The confusion matrix for distinguishing the four Rössler systems.	64
Table 2-6: Comparing the graph-theoretic approach against six other approaches.	65
Table 2-7: F-score results from applying the proposed approach.	69
Table 2-8: The confusion matrix for detecting the two conditions (overhang and bulk) from the thermal camera, high-speed camera, and photodetector.	69
Table 3-1. The build layout and contamination pattern.	86
Table 3-2: The algorithm accuracy in comparison with traditional approaches.	114
Table 4-1: The build conditions for the five disks used in this study.	125
Table 4-2: Approximate number of data points available per layer.	134
Table 4-3: The mean value of the three metrics $\rho_1$ , $\rho_2$ , and $\rho_3$ .	145
Table 4-4: Performance of two proposed algorithms in comparison with one that uses statistical features for predicting the normalized porosity level ( $\mu$ ).	149
Table 4-5: A representative confusion matrix for normalized porosity level ( $\mu$ ) based on the Laplacian eigenvectors (graph Fourier coefficients).	151
Table 4-6: The goodness of fit in exact porosity prediction using a shallow neural network with graph features as inputs.	153
Table 5-1: Boundary conditions and input parameters in DED processes.	158
Table 5-2: The information related to the spectrometer and plume camera used in the DED machine.	166
Table 5-3: Printing conditions of 10 parts and their estimated average and maximum pore length.	178
Table 5-4: (a) Confusion Matrix for two-level and three-level porosity detection.	181
Table 5-4: (b) Confusion Matrix for two-level and three-level porosity detection.	181

Table 5-5: Performance of the graph classification approach in comparison with the statistical feature's classification for the 2-level and 3-level porosity detection. 182

Table 5-6: Performance of the graph classification approach in comparison with the statistical features classification using the maximum pore length. 184

## 1 Introduction

### 1.1 Goal, Objective, and Hypothesis

The overarching goal of this work is to detect and correct the incipient defects in parts made using additive manufacturing (AM) processes. The fundamental research aspects necessary to usher such a *smart additive manufacturing* paradigm are as follows:

- (1) *Pragmatic Experimentation*: Conduct experiments designed to initiate a specific type of process phenomena or part defects, such as porosity. Characterize the quality of the parts thus built using offline measurements, e.g., an X-ray computed tomography.
- (2) *In-Process Heterogeneous Sensing*: Integrate different types of sensors inside the additive manufacturing machine and acquire sensor data as the part is being built.
- (3) *Big Data Analytics and Artificial Intelligence*: Advance novel analytical approaches to extract and correlate signatures from the large volume of heterogeneous in-process sensor data to specific defects.
- (4) *Process Knowledge (Modeling)*: Develop theoretical models to explain the fundamental physics of how and why defects are formed in the parts.
- (5) *Process Innovation*: Suggest manufacturing strategies to avoid defects in future parts with minimal experimentation. For instance, devise closed-loop controls to ensure that the defect in a layer is corrected before the next layer is deposited.

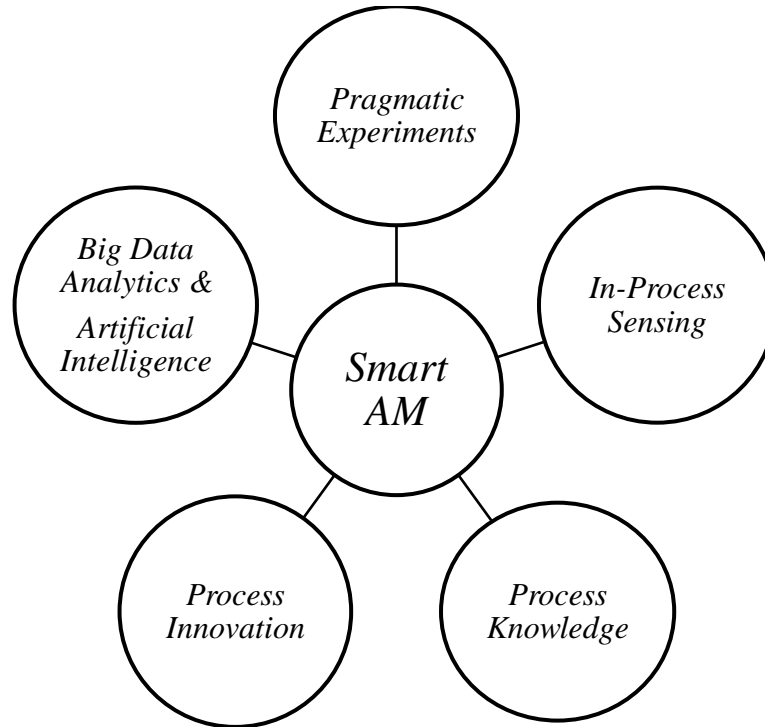


Figure 1-1: The five fundamental aspects of smart additive manufacturing.

In pursuit of the ultimate goal of smart additive manufacturing, this dissertation focuses on the first three of the five foregoing aspects, namely, (i) conducting experiments that focus on creating and studying a particular type of part defect, such as porosity; (ii) acquisition of in-process sensor data; and (iii) devising new approaches to analyze the in-process sensor data, and thereby identify and isolate part defects created during the process. Specifically, the objective of this work is to develop and apply a spectral graph theoretic approach to analyze the process signatures acquired from sensors integrated into a metal AM system for online detection of part flaws.

The central hypothesis of this work is that the spectral graph-theoretic signatures – called Laplacian eigenvalues and eigenvectors – extracted from the in-process sensor data are statistically significant discriminants of defects formed during the additive manufacturing process. In other words, the hypothesis entails that using the Laplacian

eigenspectra (eigenvalues and eigenvectors) as derived signatures from the in-process sensor data, AM part defects are detected with significantly higher statistical accuracy compared to the conventional signal processing algorithms.

This hypothesis is tested based on four practical implementations of spectral graph theory for process monitoring in two metal AM processes, called laser powder bed fusion (LPBF) and directed energy deposition (DED). These studies, which use a multitude of sensors, such as high-speed video cameras, infrared thermal sensors, and photodetectors integrated inside LPBF and DED machines, demonstrate that phenomena that are symptomatic of defect formation in AM are captured within the Laplacian eigenspectra of the acquired signals.

The resulting ability to detect defects using such a spectral graph-theoretic approach is shown to be several times faster and statistically more accurate than existing conventional signal processing techniques. For instance, in Chapter 0, the use of Laplacian eigenvectors for detecting the presence of material contamination in LPBF is illustrated. Accordingly, instances of material contamination were detected within 1 millisecond, with statistical accuracy exceeding 95% (Type II error  $< 5\%$ ) using the proposed spectral graph-theoretic approach. In contrast, conventional time series-based approaches had an error exceeding 20% and computation time of about 1 second.

Currently, metal AM parts are inspected post-process using X-Ray Computed Tomography (XCT). This is a tedious and expensive process, which becomes progressively cumbersome and costly with the size and density of the part. Instead of cumbersome post-process X-ray Computed Tomography (XCT) scanning and expensive destructive material

testing, the proposed approach uses sensor data to detect the formation of defects, so that appropriate corrective action can be taken. This research thus provides a pathway to ensure that the part quality in AM processes meets the required specifications. For instance, from a more conventional quality assurance perspective, the sensor signatures, in terms of Laplacian eigenspectra for a few defect-free parts, can be mapped after the part has been cross-examined through XCT. These sensor signatures belonging to defect-free parts can then be demarcated as a nominal baseline.

This schema can be further extended in the future to closed-loop feedback control in AM, wherein, once a defect has been detected and isolated from sensor signatures and process parameters, for example, the laser power and scan speed can be changed to correct or rectify the defect. This dissertation thus establishes the foundational step to realize a concept called *correct-as-you-build* in AM, wherein defects are detected, isolated, and removed before they are sealed in by subsequent layers.

## 1.2 Overview of the Additive Manufacturing Technology

Prior to elaborating on the challenges associated with in-process sensors and data analytics in additive manufacturing, a broader view of the scientific motivation and rationale of this research is taken. Additive manufacturing (AM), also colloquially referred to as 3D printing, is an umbrella term to represent seven different types of processes where parts are built by layer-upon-layer deposition of material as opposed to subtractive (machining) and formative (e.g. forging, casting) processes [1]. The manufacturing process in AM can be summarized in eight steps as follows [1]:

*Step 1:* Prepare the solid model of the desired part through a Computer-aided Design (CAD) software or a scanning device.

*Step 2:* Convert the CAD file into the STL (an abbreviation of *stereolithography*) file format that specifies the external surface of the part.

*Step 3:* Transfer the STL file to the AM machine language (called G-Code).

*Step 4:* Set the printing parameters on the 3D printer such as laser power, scan velocity, layer thickness, etc.

*Step 5:* Build the part layer by layer, after running the G-code on the AM machine.

*Step 6:* Remove the part from the machine build plate.

*Step 7:* Complete the extra post-processing step to clean the part and extra support material.

*Step 8:* Obtain the final product using machining, grinding, painting, and assembly with other components.

The unique ability of the AM process to selectively place material allows transcending some of the inherent boundaries of traditional subtractive and formative processes. For instance, the following *freedoms* are all described in the AM processes [2]:

- Freedom of shape and design complexity. It takes the same effort to make simple Euclidean geometries or complex lattice-like structures.
- Freedom of scale. The design of larger or smaller objects (within limits) does not cost more in terms of new tooling and machines.

- Freedom from highly skilled labor. The printing process runs almost supervision-free, irrespective of the geometry. Hence, highly skilled technicians, such as those required for machining operations are not needed.
- Freedom from material constraints and changes. Ideally, the process does not change drastically when production switches from one type of material to another. For instance, switching from steel to aluminum can be accomplished by adjusting a few parameters, as opposed to changing the expensive tooling.
- Freedom from assemblies and multiple processes. It is possible to form a part entirely with one type of AM process, without the need for intervening steps. This reduction in multiple steps is advantageous from both the cost and part integrity perspective.

An example of these freedoms is the often-used engine nozzle additively manufactured by General Electric as part of its LEAP engine. In this fuel nozzle, all 20 parts are combined into a single unit and weigh 25% less than its traditionally manufactured counterpart [3].

As another example, the buy-to-fly ratio (i.e., the ratio of raw material used to produce one pound of finished part in the aerospace industry) with traditional manufacturing is typically 15:1 to 20:1. In other words, for making a finished part weighing one pound, nearly 20 pounds of raw material is required. This buy-to-fly ratio can be drastically reduced to as small as 4:1 with AM technology [4, 5]. If this level of material and weight savings can be realized consistently by producing parts that meet stringent quality standards, it will revolutionize strategic manufacturing industries such as aerospace, automotive, biomedical, and energy generation. Now, the two (of the eight) additive

manufacturing processes that are the central focus of this dissertation are going to be introduced, namely, laser powder bed fusion and directed energy deposition.

### 1.2.1 Introduction to Powder Bed Fusion and Directed Energy Deposition

Powder bed fusion (PBF) refers to a family of AM processes in which thermal energy selectively fuses regions of a powder bed [6]. A schematic of the PBF process is shown in Figure 1-2. A layer of powder material is spread across a build plate. Certain areas of this layer of powder are then selectively melted (fused) with an energy source, such as a laser or electron beam. The bed is lowered and another layer of powder is spread over it and melted [1]. This cycle continues until the part is built.

The schematic of the PBF process shown in Figure 1-2 embodies a laser power source for melting the material; accordingly, the convention is to refer to the process as laser powder bed fusion (LPBF). A galvanic mirror scans the laser across the powder bed. The laser is focused on the bed with a spot size on the order of about  $100\ \mu\text{m}$ , and the linear scan speed of the laser is typically varied in the  $10^2 - 10^3\ \text{mm/s}$  range [1].

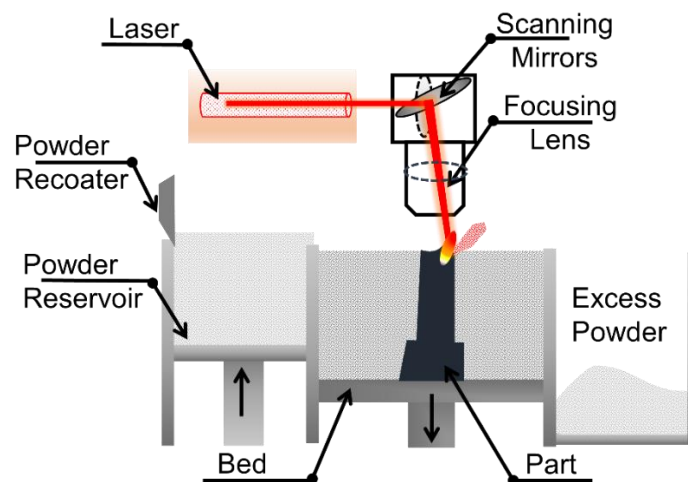


Figure 1-2: The schematic of the laser powder bed fusion (LPBF) process.

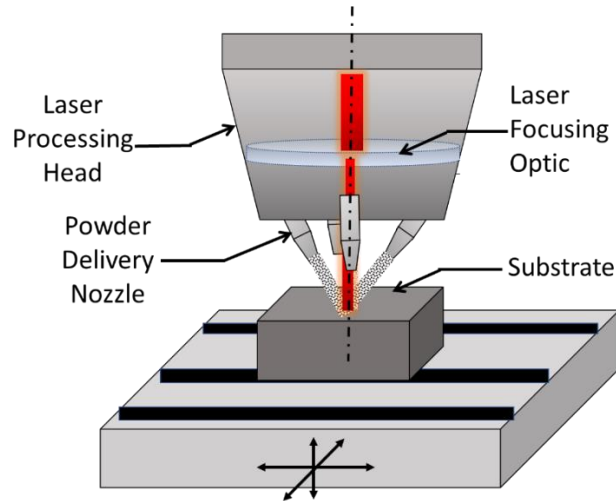


Figure 1-3: A schematic of a powder feed directed energy deposition (DED) process.

The second metal AM process investigated in this dissertation is the directed energy deposition (DED) process. Figure 1-3 illustrates a DED process. As opposed to LPBF, in DED the powder is not fused on a powder bed, but instead, the metal is sprayed from an arrangement of nozzles. A focused heat source, such as a laser, melts the feedstock material. The nozzle and table move relative to each other akin to the spindle and table of a CNC machine tool, and the part is built layer-upon-layer.

The optical system is typically capable of generating a spot size of 50 microns in diameter for printing small features or scaled up to 25 mm wide for larger parts. In the laser-based DED machines, the laser power can set between 400 and 4,000 W; high power can be achieved in systems with an arc-based energy source [7]. Two of the advantages of the DED process versus LPBF are: (1) it can be used to build on the top of previous features such as repairing the cracks on the surface of the parts, and (2) multiple different materials can be set from the nozzles, as a result of which functionally gradient parts can be made [8]. Table 1-1 represents the main differences between LPBF and DED [1, 8].

Regarding the build speed in metal AM processes, it should be noted that the powder recoating process is omitted in DED which saves a significant building time in comparison with LPBF. Furthermore, as the build plate is not required to be covered with powder, the required material for building a part in DED would be less than LPBF. However, the amount of powder recovered post-process in metal LPBF is significantly larger than in DED.

Table 1-1: Comparison between LPBF and DED processes.

	<b>DED</b>	<b>LPBF</b>
Build Speed	Fast (> 100 g/hr)	Relatively slow.
Feedstock	Powder, Wire	Powder
Heat Source	Laser, Electron Beam, or Arc Plasma	Laser
Material usage	Low	High
Build Volume	Greater than 1.2 m <sup>3</sup>	Less than 0.03 m <sup>3</sup>
Multi-Material Print	Yes	No
Resolution	Poor (Layer height > 250 μm)	Medium to High (Layer height < 50 μm)
Surface finish	Poor (Ra > 25 μm)	Medium (10 μm < Ra < 25 μm)

### 1.2.2 Motivation of the Research

Despite the demonstrated potential of metal AM to revolutionize manufacturing, process repeatability, and part consistency, there remains a consequential and open challenge [9-12]. The quality assurance-related challenges in additive manufacturing are exemplified in Figure 1-4, which shows seven identical parts built simultaneously on a commercial LPBF machine. The parts vary only in their build orientation; all other process conditions are identical. Despite extensive process automation, and besides using the default process parameter settings for the material (stainless steel) recommended by the machine manufacturer, only two parts out of seven were built successfully. The rest of the five builds were afflicted with various other types of defects, which renders them unfit for operational use. Such low process reliability makes LPBF difficult to scale commercially. More pertinently, Figure 1-4 affirms that defects in LPBF are multifarious and result from complex, poorly understood interactions amongst process phenomena, materials, processing conditions, and machine dynamics [13-17].

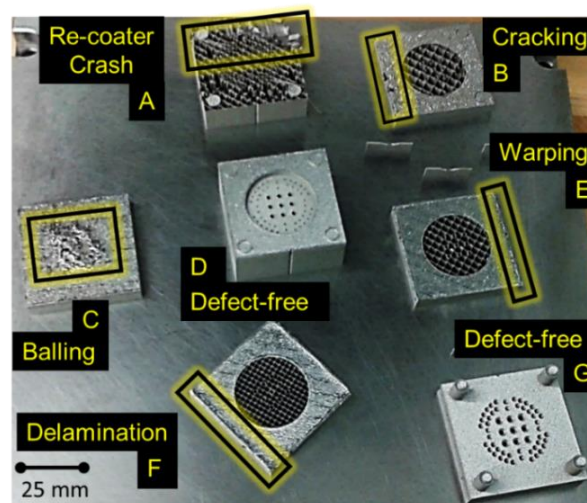


Figure 1-4: Example of process inconsistency in laser powder bed fusion. In this picture, out of the seven different orientations of the same part geometry built under identical process conditions on a commercial LPBF machine, only two (part D and part G) were completed without any visible defects. Each of the rest of the five parts had different types of failures.

Accordingly, there are two motivating reasons for in-process, sensor-based process quality monitoring in AM [18, 19]:

1. Quality inspection of LPBF parts, especially those destined for mission-critical aerospace and defense applications, currently relies on post-process scanning using X-Ray Computed Tomography (XCT), which is a cumbersome and expensive process. Moreover, the resolution of XCT scans progressively degrades with the increase in size of the part and density of the material [18]. Hence, XCT-based quality certification for every LPBF part is not viable from an industrial production perspective.
2. Although the critical process parameters, such as laser power ( $P$ , W), hatch spacing ( $H$ , mm), scan velocity ( $V$ , mm/s), and layer height (mm), can be optimized for certain part geometries, and aggregated in terms of the global volumetric energy density ( $E_V = \frac{P}{V \times H \times T}$  J/mm<sup>3</sup>), part defects can still occur as shown in Figure 1-4 [20]. This is because the global energy density does not account for the magnitude and direction of the heat flow in the part (heat flux), which may change depending on the part geometry, orientation, and location on the build plate. Nor does energy density account for the subtle machine-related malfunctions.

It is therefore imperative to establish in-process monitoring approaches in AM. One such strategy is to build a library of sensor signatures corresponding to specific defects for representative parts. Subsequently, this library can be used for the rapid qualification of part quality. If such a strategy for the in-process qualification of build quality assurance is successful, it will lead to a *qualify-as-you-build* paradigm in AM, thus expanding the reach of AM to strategically important sectors [21-25]. For the final step, after anomaly detection,

proper corrective action should be considered. These corrective actions can be described in several ways such as rescanning the surface of the part or removing the defected layer using machining.

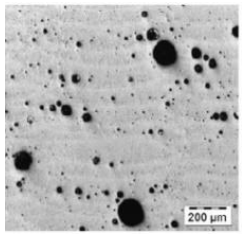
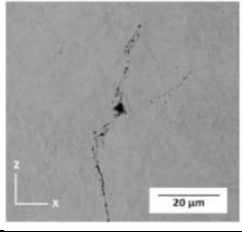
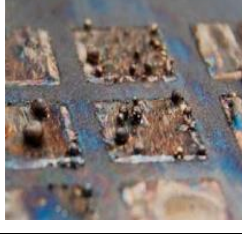
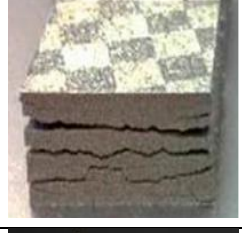
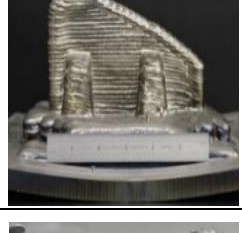
The introduction of hybrid additive manufacturing systems which combine subtractive machining and additive manufacturing in one machine is capable of entirely removing a defect. The hybrid AM technology, coupled with sensing and analytics, provides the opportunity of building defect-free AM parts without implementing the costly and time-consuming quality control inspections such as XCT. Such a *correct-as-you-build* approach is part of the planned future of research by the Laboratory for Advanced Manufacturing Processes and Sensing (LAMPS) by the Rao group at the University of Nebraska-Lincoln.

### 1.2.3 Defects in Metal AM

The two AM processes – LPBF and DED – contain a combination of complicated physics, such as absorption and transmission of laser energy, temperature-dependent properties of the material, nonlinear cooling rates, multi-scale solidification phenomena of molten metal powder, complex and heterogeneous microstructural evolution, capillary action and surface tension phenomena in the molten pool, and materials evaporation, among others [1].

Hence, to achieve a printed part with the highest quality similar to what is designed in its STL file, the printing conditions should be kept within a strictly defined nominal range. For instance, in the LPBF process alone, close to 50 parameters are known to influence the quality of the parts [26, 27]; a change in these parameters may result in a process phenomenon that can cause a defect [28]. The different types and corresponding scales of defects that typically occur in metal AM are summarized in Table 1-2 [14, 27, 29, 30].

Table 1-2: Classification of defects in metal additive manufacturing processes.

<i>Type</i>	<i>Cause</i>	<i>Figure</i>
Porosity (10 $\mu\text{m}$ to 100 $\mu\text{m}$ )	Lack-of-fusion porosity caused due to insufficient melting of powder, and gas porosity due to vaporization can be induced due to improper selection of process parameters, impurities within the powder, and the complex physics of solidification.	
Cracking (> 100 $\mu\text{m}$ )	Separation of solidified metal on the surface or grain boundaries resulting from a high-temperature gradient and residual stress.	
Balling (100 $\mu\text{m}$ to 1 mm)	Solidification of melted material into spheres due to instability in the melt pool surface tension, and wetting dynamics (Plateau-Rayleigh effect and Marangoni Convection).	
Delamination (> 1 mm)	Separation of successive layers because of insufficient overlap with previous underlying solidified layers, and incomplete melting of the powder particles.	
Warping (> 1 mm)	Bending on the sides of the part when the thermal stress in the substrate exceeds the strength of the substrate material	
Geometric (> 1 mm)	Geometric deviations from the nominal model, typically due to shrinkage of the molten metal, and poor calibration of the machine.	

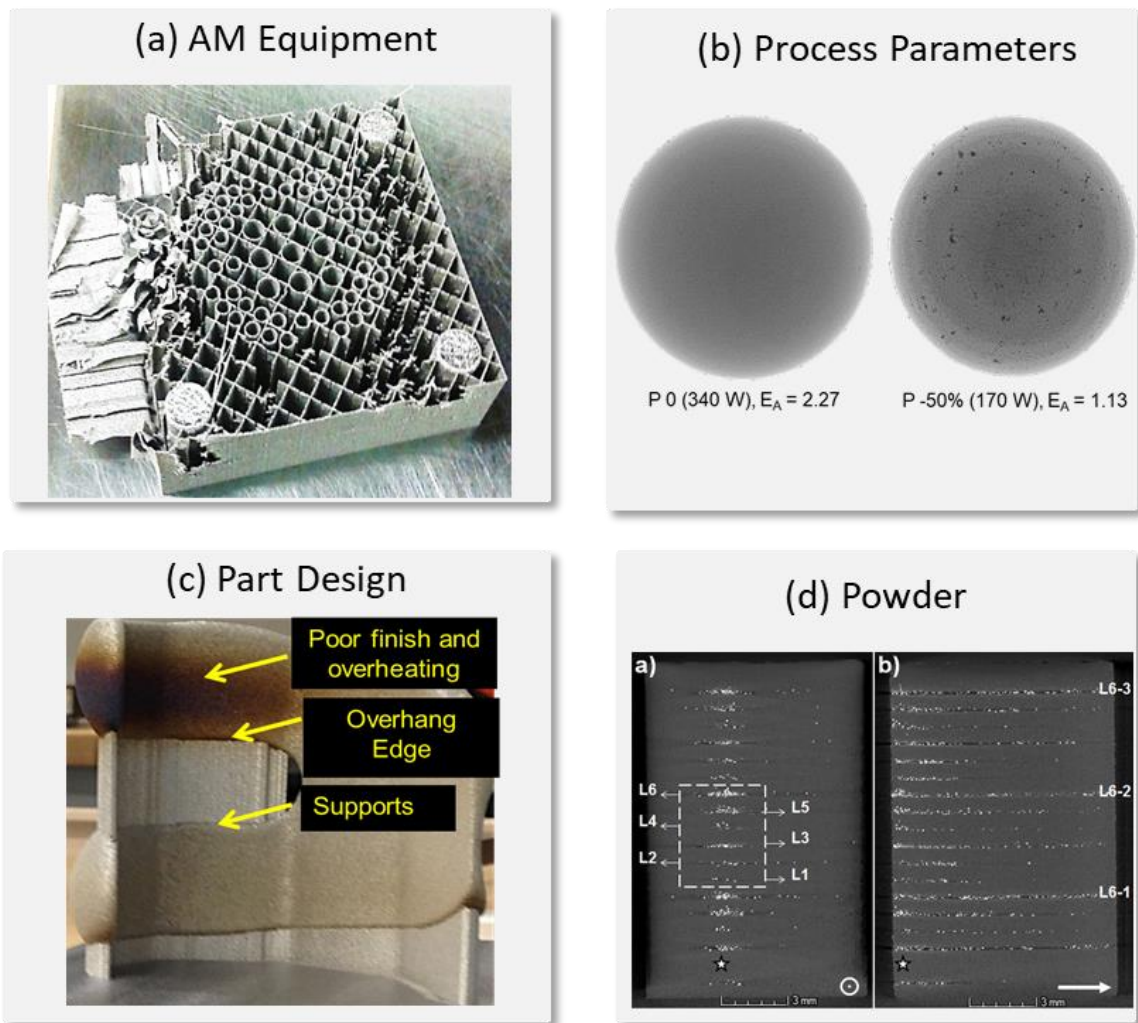


Figure 1-5: Illustration of the four major causes of defects in metal AM parts.

- (a) Build failure resulting from poor calibration of the AM machine, shown here is an instance of recoater crash caused due to unbalanced torquing of the bolts holding down the build plate.
- (b) Poor choice of process parameters, e.g., if the laser power is insufficient to melt the material it will lead to lack-of-fusion defects as seen in this image
- (c) Ill-considered design of the part – shown is a knee implant with a long overhang section which is not adequately supported, which leads to overheating and microstructural heterogeneity
- (d) Poor quality of feedstock materials, such as the presence of contaminants and non-uniform particle size. For instance, this image is an X-ray of a Inconel 625 coupon with tungsten contaminant particles evident as bright particles.

The aforementioned defects in metal AM are separable into four main types [31]. These are summarized in Figure 1-5 and explained in detail below.

(a) AM Equipment. The equipment-induced defects are related to imperfections and improper calibration of AM machine components. The source of this type of defect may be attributed to the laser beam variation, build chamber environmental condition, powder recoating system, and build surface alignment, etc[32]. For instance, in Figure 1-5 (a), a part has failed to build due to contact with the recoater. The reason for the recoater crash is probably associated with the poor calibration of the distance of the recoater blade from the build platen, or due to uneven tightening of the bolts fixing the build platen to the powder bed.

(b) Process Parameters. The interaction between the energy source (laser power), fresh metal powder, and the fused material is capable of initiating process-induced defects. The defects typically result from a combination of printing parameters [33-38]. For instance, energy density (called Andrew Number) – a representative term for the laser energy applied per unit volume of the build ( $\text{J}/\text{mm}^3$ ) – is a key factor in the LPBF and DED process as a function of the laser power (watt), spacing between passes of the laser (mm), scan velocity of the laser (mm/sec), and build layer height (mm). The energy density significantly impacts the physical and mechanical properties of the printed parts [39, 40]. Changing the printing parameters will change the energy density, which in turn will determine the thermal gradients in the part and ultimately the physical properties. Hence, the nominal values associated with each factor should be optimized with respect to the powder material and part design.

Figure 1-5 (b) demonstrates the effect of decreasing laser power by 50% from the nominal point (340 W), which results in the decrease in energy density and formation of lack-of-fusion pores. Other factors such as the effect of inert gas flow within the build chamber are also consequential. For instance, Ferrar, *et al.* investigated the effect of gas flow on the repeatability of the part properties within and between LPBF builds. The results demonstrated that the gas flow variation affects both the value and the range of density as well as compression strength of porous titanium components [41].

(c) Part Design: The components and features included in part design play a fundamental role in the mechanical properties of the manufactured object. These part features, apart from the geometry of the final part, also include the support material, which is a sacrificial material, and the part orientation on the build plate. The supports are generated to ensure down-facing (overhang) regions do not collapse as a result of weight from successive layers, and the part remains fixed in its designed place. Supports are also purposely built to ensure that the heat in the part during the build process is distributed to avoid thermal residual stresses that may warp the part or affect the geometry of the build [10, 42-46]. In Figure 1-5 (c), the overhang edge of a knee implant is affected by the heat accumulation in the overhang region because of the overly thin cross-section area of the supports, which in turn caused the change in the microstructure.

(d) Powder feedstock material. Powder characteristics, namely size, shape, surface morphology, composition, the presence of extraneous impurities, and moisture can lead to defects, such as porosity. For instance, the moisture in the powder may vaporize, leading to pinhole porosity defects. The powder quality is governed by the techniques used for manufacture of the powder, i.e. gas atomization (GA), rotary atomization (RA), and plasma

rotating electrode process (PREP)[29]. Figure 1-5 (d) illustrates the vertical cross-section of the AM parts made from Inconel 625 that is contaminated by the tungsten particle at some designated layers. The impurities can negatively affect the quality and mechanical properties of the parts.

#### 1.2.4 Analytical Methods for Process Monitoring in Metal AM

The application of sensing and in-situ monitoring in two metal AM processes—namely, LPBF and DED—are discussed in detail in each chapter. However, to have a better overview of the diversity of analytical methods applying to the sensor data (signals, images), the following survey is provided. Table 1-3 summarizes a complete range of studies and commercial software, implementing analysis on the sensor data in the online monitoring of AM processes[47, 48].

Clijsters *et al.* [49] used a combination of two optical sensors to monitor the geometric characteristics of the melt pool. Having a pair of photodiode and near-infrared thermal CMOS cameras working with a sampling frequency of 10 kHz to 20 kHz, they studied the monitoring of the part quality based on melt pool characteristics like intensity, area, length, and width. The resulting images generated by this system are representative of melt pool variation that could be attributed to the porosity in the part.

Doubenskaia *et al.* [50] implemented an optical monitoring system in a selective laser melting machine. The online monitoring of temperature was performed using a bi-color pyrometer and a CCD camera integrated with a PHENIX PM-100 device. They found that the variation of temperature at the heat-affected zone could be captured as a result of an improper change in printing parameters, such as printing velocity, hatch distance, and layer thickness.

Table 1-3: Overview of the analytical approaches in metal AM.

Reference	Process Signature	Sensing/Data Generation Approach	Defect / Phenomenon	Analytical Method
Clijsters, 2014[49]	Melt pool shape	Pyrometry	Porosity	position-based visualization (mapping)
Doubenskaia, 2012[50]	Temperature profile	Pyrometry, Optical Imaging	Geometry, Mechanical Properties	Image processing
Kanko, 2016[51]	Track geometry	Interferometric imaging	Process defects (i.e. porosity)	Plotting, Image processing
Mazumdar, 2015[19]	Geometry, temperature, microstructure, and composition	Optical spectroscopy	Geometry, Cracking, Porosity	Supervised (like SVM) and unsupervised techniques with PCA
Li, 2019[52]	Temperature, vibration	thermocouples, infrared sensors, and accelerometers	Surface Roughness	ensemble learning algorithm
Zhang, 2017[53]	Powder spreading	Discrete Element Method (DEM)	Geometry	Neural Network
Gobert, 2018[54]	Powder spreading, fused powder	digital single-lens reflex (DSLR) camera	Porosity, Cracking	ensemble binary classification
Scime, 2018[55]	Powder spreading	Stock Camera	Surface Roughness, Porosity, Part Failure	Computer vision unsupervised learning
Shevchik, 2018[56]	Acoustic waves	Acoustic Sensing	Porosity	Wavelet transform, SCNN
Concept Laser Toolkit[57]	Meltpool, Laser source	Pyrometry, Optical Imaging	Undesired Parameter Change	Computer vision
EOS Toolkit[58]	Meltpool, tomography	Pyrometry, Optical Imaging	Undesired Parameter Change	Computer vision

Kanko et al. [51] introduced the application of a new imaging technique to capture the melt pool morphology and laser track. Inline coherent imaging (ICI), low-coherence interferometric imaging, was used to represent the melt pool dynamics and capture the quality of the laser tracks.

Mazumdar [19] implemented a new design for metal additive manufacturing processes to certify the quality of the parts. Having a closed loop feedback system equipped with optical sensors, he gathered the process signatures related to the part temperature, microstructure, and composition to certify the compliance of the part. The optical emission spectroscopy signal was used for detecting the porosity and cracks using supervised and unsupervised machine learning techniques. At the same time, the plasma signal was used in a multiple parameter algorithm to define the composition and phase change of the part.

Li et al. [52] studied the improvement of the surface morphology in additive manufactured parts. They introduced a data driven system to predict the surface roughness using multiple sensors incorporated into a fused filament fabrication (FFF) machine, including thermocouples, infrared, and accelerometers. The temperature and vibration data represented in the time and frequency domain were used for training an ensemble algorithm to predict the surface roughness with high accuracy.

Powder spreading is one of the important steps in the powder bed fusion process which is not studied well in the literature. Zhang *et al.* [53] investigated the effect of powder spreading parameters, such as spread speed, on the structure and quality of the powder layer. Given the fact that the simulation of the spreading process is expensive and time

consuming, they used a Discrete Element Method (DEM) to simulate a few layers and fed the results into a machine learning algorithm to predict the rest of the process.

Grobert *et al.* [54] studied the in-situ monitoring of powder bed fusion using optical imaging. A digital single-lens reflex (DSLR) camera was used to capture the build plate before and after each recoating phase. Using a binary classification technique like the support vector machine, the authors distinguished between two types of build structures—namely, flaw and normal build conditions. In order to generate the ground truth or labels of each layer, a high resolution CT was performed on the manufactured parts. These X-ray images were used to identify anomalies like lack of fusion, cracks, or inclusions with their XYZ locations. The online detecting algorithm could reach an accuracy of 80% in a two-level classification problem.

Scime *et al.* [55] introduced a comprehensive real time monitoring system in an LPBF machine. The stock camera and lighting configurations added to the LPBF machine were used to generate the optical images after spreading a layer. They specified eight anomalies related to the powder recoating process that were used for labeling the optical images. To analyze the data, a computer vision and unsupervised machine learning technique (K-means) were implemented that resulted in more than 80% classification accuracy.

Shevchik *et al.* [56] investigated the application of acoustic emission sensors for quality monitoring of selective laser melting (SLM). They generated different levels of porosity in the workpiece by changing the process parameters. To capture the acoustic signal, a fiber Bragg grating sensor was installed into a commercial SLM machine. The feature, extracted from the acoustic signal using a standard wavelet packet transform

(WPT), was used in spectral convolutional neural networks (SCNN) to classify the severity of the pores with 83% to 89% accuracy.

Some of the LPBF machine developers started to introduce different types of process monitoring toolkits. These modules generally focus on the in-situ monitoring of the process and provide users with post process reports. As a result, the output of the toolkits cannot directly be attributed to the defects and further analysis and algorithms are required to provide an automatic alarm for the occurrence of a defect.

Concept laser, which is one of the main leading providers of AM machines, has developed a quality management (QM) system suit that incorporates several modules. The QM Meltpool 3D module is designed to monitor melt pool characteristics, such as area and intensity, using a photodiode and a camera. Some of the other modules in the toolkit are QM coating, fiber power, atmosphere focusing on the monitoring of powder dose factor, laser power, and oxygen concentration respectively [57].

EOS, another global AM technology leader, has provided the EOSTATE Meltpool for real-time monitoring of the process as an extension to the EOS M290 machine. The incorporated sensors capture the melt pool light emission to display the melting process. The process lighting is also separated from the reflected laser light to eliminate the noise data. This toolkit is equipped with other modules to monitor other aspects of the process. The EOSTATE powder bed records the quality of coating and the exposure phase using a camera. The other valuable module that eliminates the requirement of post process scanning is EOSTATE Exposure OT which provides complete optical tomography throughout the part [58].

### 1.3 Contribution of the Graph Theoretical Approach

In this section, two mathematical justifications of using the graph theoretical eigenspectra (Laplacian eigenvalues and eigenvectors) are described as to why the Laplacian eigenspectra are appropriate quantifiers for monitoring the process states:

- a) An analogy with the Fourier transform from the statistical signal processing is proffered.
- b) An explanation is given from the network topology perspective.

#### a) A Justification from the Signal Processing Viewpoint

The following properties of the normalized Laplacian matrix  $\mathcal{L}_n$  are important. Because  $\mathcal{L}_n$  is a diagonally dominant symmetric matrix with non-positive off-diagonal elements (called the Steiltjes matrix) [59] it leads to the following properties:

- $\mathcal{L}$  is symmetric, positive semi-definite, (i.e.  $\mathcal{L} \geq 0$ ).
- The eigenvectors of  $\mathcal{L}$  are orthonormal to each other.

Based on the orthogonality of the Laplacian eigenvectors, a link between the graph transform  $\mathcal{L}_X(\lambda^*, \mathbf{v})$  and the fast Fourier transform (FFT) can be made, where  $\mathcal{X}$  is a sequence of sensor data (time series or images). It is apparent that the eigenvectors of the Laplacian are essentially like a Fourier basis.

In other words, the so-called graph Fourier coefficients  $c_i$  are multiples of the eigenvalues  $\lambda^*$  of the Laplacian. In summary, a mapping of  $\mathcal{X} \mapsto \mathcal{L}_X(\lambda^*, \mathbf{v})$  can be achieved in which the dynamics are characterized using the Laplacian eigenvectors ( $\mathbf{v}$ ). Instead of tracking statistical features of the signal in the time and frequency domain, the

proposed graph-theoretic approach entails monitoring the topology of the network graph ( $G$ ) in terms of the Laplacian eigenvectors ( $\mathbf{v}$ ).

As a result, the graph theoretical transform eliminates intermediate signal filtering steps and provides multi-dimensional signals. It does not require mining statistical features, such as mean, standard deviation, etc., from the data as the presented approach is feature-free.

In addition, the approach does not require predefined basis functions similar to the sinusoidal basis for the Fourier transform, or a predefined probability distribution as in typical stochastic modeling schemas; and the need for a rigid model structure is eliminated (e.g., the number of hidden layers and nodes in a neural network).

#### b) A Justification from the Network Topology Viewpoint

The first justification in the literature is from Belkin and Niyogi [60, 61] who substantiated the intuition that the graph Laplacian, indeed, captures the complex spatiotemporal dynamics of high dimensional data in a low dimensional space—namely, the graph  $G(V, E, W)$ —based on the theory of Laplace-Beltrami operators on Riemannian manifolds. Elucidating this justification is beyond the scope of the current work.

The second justification is motivated from a spectral graph segmentation area. It is based on the normalized Laplacian and was proved by Shi and Malik [62]. Shi and Malik showed that the Laplacian eigenvector  $\mathbf{v}_2$  (Fiedler vector) is the most efficient means to partition a graph  $G \equiv (V, E, W)$ . Partitioning a graph is analogous to the number of edges that must be broken to cut a graph into two. The eigenvector  $\mathbf{v}_2$  is the shortest way to

partition a graph (to sever the least amount of edges); the eigenvector  $\boldsymbol{v}_3$  is longer, and so on ( $\boldsymbol{v}_1$  is merely a vector of ones and corresponds to an eigenvalue of 1). In other words, the Laplacian eigenvectors and eigenvalues are not merely statistics but are *topological invariants* that are representative of the signal structure in the graph space.

The specific mathematical implication of Shi and Malik's work is that the graph segmentation (or cutting) problem has an efficient discrete solution in the Rayleigh quotient of the Laplacian matrix  $\mathcal{L}$  [62]. Consequently, on using the Courant-Fischer theorem (see Ref. [63]), which gives minimum and maximum bounds on the Rayleigh quotient, Shi and Malik arrived at the following solution to a discretized modification of the graph segmentation problem, where  $\mathbf{x}$  is a vector in the span of  $\mathcal{L}$ , and the left hand side terms are Rayleigh quotients of the Laplacian:

$$\arg \min_{\mathbf{x}_j} \frac{\mathbf{x}_j^T \mathcal{L} \mathbf{x}_j}{\mathbf{x}_j^T \mathbf{x}_j} = \boldsymbol{v}_2, \quad \min_{\mathbf{x}_j} \frac{\mathbf{x}_j^T \mathcal{L} \mathbf{x}_j}{\mathbf{x}_j^T \mathbf{x}_j} = \lambda_2; \text{ and} \quad (1-1)$$

$$\arg \max_{\mathbf{x}_j} \frac{\mathbf{x}_j^T \mathcal{L} \mathbf{x}_j}{\mathbf{x}_j^T \mathbf{x}_j} = \boldsymbol{v}_k, \quad \max_{\mathbf{x}_j} \frac{\mathbf{x}_j^T \mathcal{L} \mathbf{x}_j}{\mathbf{x}_j^T \mathbf{x}_j} = \lambda_k$$

Therefore, the Fiedler vector ( $\boldsymbol{v}_2$ ) solves the graph segmentation (cutting) problem, with the Fiedler number ( $\lambda_2$ ) as the minimum attained [62]. The highest eigenvalue ( $\lambda_k$ ) is the maxima. Thus, the Laplacian eigenvectors are linked to the inherent structure in the signal.

## 1.4 Structure of the Dissertation

Table 1-4: The categories used for analyzing the fidelity of defect detection.

Chapter	Source of Anomaly	Collaborators	Status
Chapter 2 Build Condition Monitoring in LPBF	Part Design (Overhang)	<i>Dr. Brandon Lane</i> NIST Engineering Laboratories	Published in ASME Transactions
Chapter 3 Material Contamination Monitoring in LPBF	Powder Contamination	<i>Mr. Paul Boulware</i> Edison Welding Institute (EWI)	Published in ASME Transactions
Chapter 4 Porosity Monitoring in LPBF	Process Parameters	<i>Dr. Abdalla Nassar</i> Applied Research Laboratory	Published in Institute of Industrial and Systems Engineers
Chapter 5 Porosity Monitoring in DED	Process Parameters, and possibly AM machine	<i>Dr. Abdalla Nassar</i> Applied Research Laboratory Pennsylvania State University	Published in Additive Manufacturing

Table 1-4 summarizes the outcomes from this research; we provide a brief summary of each chapter herewith. Given the quality-related impediments, manufacturers are reluctant to use AM parts in mission-critical applications. An approach to overcome these bottlenecks in metal AM is to rapidly qualify the part quality *in situ* – inside the machine – instead of offline using XCT, by means of in-process sensing and data analytics. Indeed, such a sensor-based approach for quality assurance in AM has been identified as a research priority in roadmap reports by federal agencies, national labs, and in research articles [9, 12, 14]. To investigate different types of anomalies in metal AM and build a dictionary of sensor signatures, specific experiments must be conducted to isolate the origin of each type of defect in terms of sensor signatures.

Accordingly, a series of experimental datasets in collaborations with researchers at national labs, industries, and universities have been used. Table 1-4 represents four different experiments performed based on the origins of the design, powder, process parameters, and AM machine for defect formation.

Regarding the design-based errors in metal AM, the experiments in Chapter 2 are conducted at the Engineering Laboratory of the National Institute of Standards and Technology (NIST) by Dr. Brandon Lane and Dr. Jarred Heigel. The goal of this work is to monitor the LPBF process using an array of heterogeneous sensors so that a record may be made of those temporal and spatial build locations where there is a high probability of defect formation. In pursuit of this goal, a commercial LPBF machine was integrated with three types of sensors, namely, a photodetector, high-speed visible camera, and shortwave infrared (SWIR) thermal camera with the following objectives: (1) to develop and apply a spectral graph-theoretic approach to monitor the LPBF build condition from the data acquired by the three sensors, and (2) to compare results from the three different sensors in terms of their statistical fidelity in distinguishing between different build conditions.

The first objective will lead to the early identification of incipient defects from heterogeneous sensor data. The second objective will ascertain the monitoring fidelity tradeoff involved in replacing an expensive sensor, such as a thermal camera, with a relatively inexpensive, low-resolution sensor, e.g., a photodetector. As a first-step towards detection of defects and process irregularities that occur in practical LPBF scenarios, this work focuses on capturing and differentiating the distinctive thermal signatures that manifest in parts with overhang features. Although not a defect, overhang features can

significantly decrease the ability of laser heat to diffuse from the heat source. This constrained heat flux may lead to an issue such as poor surface finish, distortion, and microstructure inhomogeneity. In this work, experimental sensor data was acquired during LPBF of a part having an overhanging angle of  $40.5^\circ$ .

The second experiment described in Chapter 3 is specifically focused on analyzing the feedstock material-induced defects. Experiments for this chapter were conducted on the open architecture LPBF platform at Edison Welding Institute (EWI) directed by Mr. Paul Boulware [64, 65]. In this study, the goal was to detect the onset of material cross-contamination in the LPBF AM process using data from *in-situ* sensors. Material cross-contamination refers to trace foreign materials that may be introduced in the powder feedstock used in the process due to reasons such as poor cleaning of the AM machine after previous builds, or inadequate quality control during production and storage of the feedstock powder material. Material cross-contamination may lead to deleterious changes in the microstructure of the AM part and consequently affect its functional properties.

The objective of the work described in Chapter 3 was to develop and apply a spectral graph-theoretic approach to detect the occurrence of material cross-contamination in real time during the build using in-process sensor signatures, such as those acquired from a photodetector. The central hypothesis is that decomposing the process signals acquired from the photodetector in the spectral graph domain leads to early and more accurate detection of material cross-contamination in LPBF compared to the traditional stochastic delay-embedded time series analysis techniques, such as autoregressive (AR) and autoregressive moving average (ARMA) modeling. To test this hypothesis, Inconel alloy

625 test parts were made on a custom-built LPBF apparatus integrated with multiple sensors, including a photodetector with the wavelength range of 300 nm to 1100 nm.

The third experiment described in Chapter 4 was performed at the Applied Research Laboratory at Pennsylvania State University by Dr. A. R. Nassar. The goal of this research was to detect the onset of defects such as porosity in additively manufactured metal parts using data acquired from in-process sensors. As a step towards this goal, this study focuses on the analysis of in-process sensor data to detect lack-of-fusion porosity in titanium alloy (Ti-6Al-4V) parts made using the DED metal additive manufacturing process. This avenue of research is consequential to ensure the production-scale viability of additive manufacturing processes, which despite their significant and revolutionary advantages over conventional subtractive and formative manufacturing processes, are currently impeded by their lack of part consistency and quality.

To realize this objective, Inconel 718 cylinders were built on a commercial LPBF machine (3D systems ProX 200) with different process settings. Optical emissions were monitored using a multispectral photodetector array to estimate the line-to-continuum emissions around 520 nm. The line-to-continuum ratios were subsequently related, on a layer-by-layer basis, to the level of porosity in the part obtained from offline XCT scans. The link between the in-process multispectral sensor and XCT data was made via the spectral graph Laplacian eigenvectors and eigenvalues extracted from the photodetector signals.

In chapter 5, equipment and parameter-induced lack-of-fusion defects, were investigated using a dataset acquired from an Optomec MR-7 DED machine from the Applied Research Laboratory at Pennsylvania State University by Dr. A. R. Nassar. The objective of this work was to detect *in situ* the occurrence of lack-of-fusion defects in titanium alloy (Ti-6Al-4V) parts made using the DED process. For realizing this objective, the data from two types of in-process sensors, namely, a spectrometer and a visible spectrum optical camera are used which was integrated into an Optomec MR-7 DED machine. Both these types of sensors were focused on capturing the dynamic phenomena in the melt pool region. Specifically, the spectrometer measures the line-to-continuum ratio of the optical emission corresponding to atomically excited titanium atoms (Ti I) in the 430 nm and 520 nm wavelength regions, while the optical camera captures the images of the melt pool plume.

To detect lack-of-fusion porosity from this sensor data, an approach is devised to fuse (combine) the data from the in-process sensors, invoking the concept of Kronecker product of graphs. Accordingly, this work demonstrated the use of heterogeneous in-process sensing and online data analytics for *in situ* detection of defects in DED metal AM processing.

The critical need for an in-process monitoring strategy to detect porosity in DED is exemplified in Figure 1-6, which shows five slices of X-ray computed tomography (XCT) images taken in the X-Y plane, perpendicular to the build direction (Z-axis), of a cuboid-shaped titanium alloy (Ti-6Al-4V) test coupon made in this study.

The part in Figure 1-6 shows the intermittent occurrence of lack-of-fusion type porosity. For instance, layers 1 and 2 were found to be discernably free of flaws; however, in layer 6 prominent lack-of-fusion type pores were observed along the seams of two adjacent hatches made by the laser, which are termed as *systematic flaws*. In layer 9, a large pore (> 50  $\mu\text{m}$  diameter) was observed whose root-cause was not readily explicable – these are termed as *random flaws*. Continuing with the deposition, layer 13 was again demonstrably free of flaws.

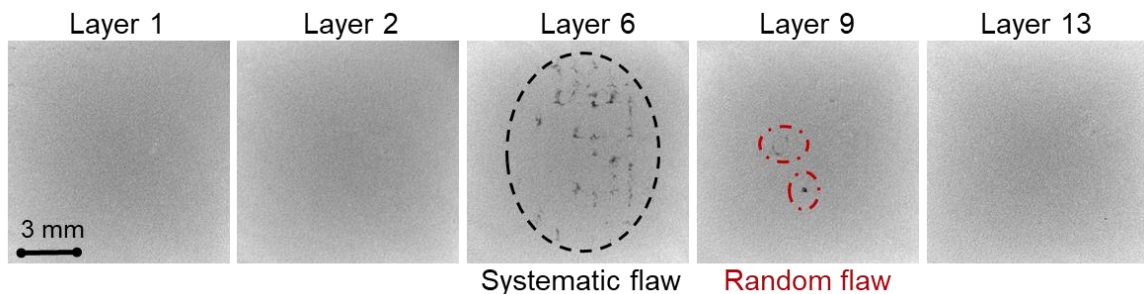


Figure 1-6: X-ray Computed Tomography of a titanium alloy DED part at different layers showing presence of systematic and random (stochastic) flaws.

In this part the first few sequences of layers are devoid of observable flaws (flaw-free state) followed by the sudden appearance of systematic and random flaws, before returning to a flaw-free state.

Based on the observations tendered in Figure 1-6, the scientific rationale for this work is as follows: defects in metal AM processes, such as DED can occur despite offline empirical optimization. This is due to the complex, and yet not completely understood, intricate interactions between part design, process parameters, and material behavior that influence the thermal physics of the process, and which in turn governs defect formation. Additionally, noise factors, such as impurities in the feedstock, inaccuracies in the machine, and changes in the environmental conditions are known to influence the quality and consistency of AM parts.

### Note to the Reader

A literature review chapter is not provided in this dissertation. Instead, a contextual approach was chosen by providing a literature review in each chapter. In principle, Chapters 2 through 5 are meant to be standalone descriptions of the work; each of these four chapters have now been published as peer-reviewed archival journal articles.

## 2 Build Condition Monitoring in LPBF

### 2.1 Goal, Objective, and Hypothesis

The goal of this work is to monitor the laser powder bed fusion (LPBF) process using in-process sensor signatures so that a record may be made of those temporal and spatial build locations where there is a high probability of defect formation. This goal is termed as build condition monitoring. In pursuit of this goal, a commercial LPBF machine was integrated with three sensors, namely, a photodetector (spectral response 300 nm to 1200 nm), high-speed visible spectrum video camera (4,000 frames per second, spectral response 300 nm to 950 nm), and shortwave infrared (SWIR) thermal camera (1,800 frames per second, spectral response 1350 nm to 1600 nm, thermally calibrated from 500 °C to 1025 °C) with the following two objectives:

*Objective 1:* Develop and apply a spectral graph-theoretic approach to monitor the build condition in LPBF from the data gathered by the aforementioned three sensors. The intent is to detect the onset of deleterious phenomena such as unexpected variations in the thermal history (cooling rate) which would lead to inconsistent properties [66-68]. In the worst case, these may ultimately result in build failures. The proposed approach is extensible to other AM processes and sensor systems.

*Objective 2:* Assess the statistical fidelity of the three different sensors, namely, high-speed camera, infrared thermal camera, and a photodetector in monitoring the LPBF build condition by capturing the differences in the thermal signature of the part as it is being built. The intent is to ascertain the monitoring fidelity tradeoffs when replacing a relatively expensive, high-fidelity sensor such as a thermal camera with an inexpensive, low-fidelity sensor, e.g., a photodetector.

Realizing these objectives will lead to the following consequential impacts:

1) In-process quality monitoring in LPBF.

Unfortunately, even with the high level of process automation in commercial equipment, print defects are common in LPBF, which hinders the use of LPBF parts in mission-critical applications, such as aerospace and defense [12, 69]. While there is an abundance of pioneering literature on sensor integration and hardware aspects for monitoring AM processes, there is a persistent research gap in seamlessly integrating the in-process sensor data with approaches for online signal analytics [70, 71]. This gap has been pointed out in roadmap reports published by federal agencies and national labs [9, 12, 72-74]. Addressing this need for online data analytics is critical to mitigate the poor repeatability and reliability in LPBF, and more generally in AM.

2) Layer-wise analysis of sensor data to reduce expensive testing.

To ensure compliance, the norm is to subject LPBF parts to X-Ray computed tomography (XCT) or destructive materials testing. This is prohibitively expensive and time-consuming [18, 75]. However, if a layer-by-layer sensor data record is available, then this data, instead of destructive testing or XCT scanning, can be used to rapidly qualify the part quality, leading to considerable cost savings [21, 76].

Furthermore, because AM phenomena and concomitant defects occur at multiple scales, there is also the need to combine data from multiple sensors. The challenge with this concept of using sensor data for layer-wise quality assurance in AM – termed *certify-as-you-build* by Professor Jyoti Mazumder [19] – is that sensors may differ in resolution, sensitivity, or bandwidth appropriate to detect particular process signatures. The limited

fidelity of a single sensor limits the variety of defects that it may be able to detect if any at all.

In closing this section, it should be noted that researchers in the AM area prefer the term *qualify-as-you-build* over *certify-as-you-build*, based on the reasoning that certification is typically done by a third-party in the quality assurance paradigm. In the same vein, Sigma Labs, Inc., of New Mexico, has trademarked the term in-process quality assurance (IPQA) in reference to their PrintRite3D software that combines process monitoring, data analysis, and feedback control in AM [77, 78].

Each type of build defect in LPBF relates to a specific process phenomenon. The onset of such defect-causing phenomena may manifest in statistically distinctive signatures from appropriately designed and utilized sensors [79-81]. Hence, by tracking the signatures from in-process sensor data, it is hypothesized that the defects in the LPBF process can be discriminated. The hypothesis tested in Sec. 2.5 is that the spectral graph-theoretic approach forwarded in this work leads to higher statistical accuracy for distinguishing the build condition compared to popular machine learning approaches, such as neural networks and support vector machines. The statistical accuracy is measured in terms of the statistical F-score, which combines both the Type I (false alarm) and Type II (failing to detect) statistical errors.

The applicability of the different sensors and the proposed analysis methodology was tested by building an overhang part. While not a defect, the LPBF of overhang features is a challenging proposition due to the following reason. As the thermal conductivity of the powder is roughly one-third of a solid part, heat tends to accumulate within the overhang

area, i.e., the thermal flux through an overhang is restricted [67]. Constriction of heat to a relatively small area leads to inconsistent thermal gradients within the overhang features compared to the bulk material, which ultimately manifests in distorted builds, poor surface finish, or heterogeneous microstructures [29, 46]. In this work, the distinctive thermal signature representative of overhang features was used as a means to discriminate the build condition. Furthermore, the present work provides an avenue for online monitoring of in-process signals through analysis in the spectral graph domain.

The understanding of thermal aspects of overhang geometries is also consequential in the related context of design for additive manufacturing. For instance, recent studies emphasize the need for an evolved approach for support design depending upon the severity of the overhang feature [45].

The rest of this study is organized as follows: Sec. 2.2 summarizes the recent developments in sensing and monitoring in LPBF. Sec. 2.3 describes the experimental LPBF studies carried out at NIST. Sec. 2.4 elucidates the spectral graph-theoretic approach and illustrates its application to a synthetic signal. Sec. 2.5 discusses the results from the application of the spectral graph-theoretic approach to analyze the thermal imaging, high-speed videography, and photodetector signals acquired during the build process. In closure, the conclusions from this work and avenues for further research are discussed in Sec. 2.6.

## 2.2 Prior Work and Challenges in Sensor-Based Monitoring in LPBF

Tapia and Elwany [82] have conducted a comprehensive review of sensor-based process monitoring approaches, specifically focused on metal AM processes. More recently, Foster *et al.* [83], Purtonen *et al.* [84], Mani *et al.* [73], Everton *et al.* [85], and

Grasso and Colosimo [14] provided excellent reviews of the status quo of sensing and monitoring focused in metal AM. However, there is a persistent gap in analytical approaches to synthesize this data and extract patterns that correlate with specific process conditions (build status) and defects [86]. Chua *et al.* in a recent article have placed emphasis on the need for (a) data mining, (b) data processing, and (c) data analysis to monitor and subsequently translate the sensor signatures into actionable feedback control [70]. From the hardware vista, two methods were predominantly used in the literature towards monitoring the PBF — namely, melt pool monitoring (MPM) systems and layer-wise imaging (staring) systems. The relevant works under these respective headings are summarized in the following two sections, Sec. 2.2.1 and Sec. 2.2.2, respectively.

### 2.2.1 Melt pool Monitoring Systems in PBF

The AM group at the Catholic University of Leuven, Belgium has published several influential articles in the area of quality monitoring and control in LPBF, as well as in the general area of AM; a select few of these are cited herewith [80, 81, 87-90]. The common theme in these prior works is in extracting features from the data from one sensor at a time, typically, in terms of a statistical moment (mean, variation) of image-based grayscale values, and correlating these features with controlled flaws based on the offline analysis[91-93]. However, to take these pioneering works in sensing forward into the domain of real-time closed-loop process control and further to defect correction, there is a need to translate the signals into decisions in real time. In turn, this work addresses a necessary and critical step to realize real-time decision-making by translating the process signatures in a form tractable for build condition monitoring.

Craeghs *et al.* [90] explained the need for a melt pool imaging system, which was also coupled with sensors capable of monitoring the status of process inputs. Although the melt pool was valuable for monitoring the local thermal aspects, it was difficult to translate the melt pool information quickly into a corrective action since process dynamics are relatively faster than current technologies for sensor acquisition, processing, and feedback control. In other words, Craeghs *et al.* [90] recommended that a heterogeneous sensor suite be used for process monitoring PBF processes. The work reported in the study assessed the fidelity of using different sensors for process monitoring.

For monitoring the melt pool, a photodiode and (complementary metal oxide semiconductor) CMOS camera coaxial with the laser and equipped with infrared (IR) filters were used by Craeghs *et al.* [90]. This constrained the wavelength of light in the region of 780 nm to 950 nm. The upper limit was at around 1000 nm to block out the laser wavelength from entering the detectors. The sampling rate was 10 kHz. This translated to a sample every 100  $\mu\text{m}$ , considering a 1000 mm/sec scan speed. Using image processing techniques, the authors ascertained the melt pool area and the length to width ratio of the melt pool and used these for tracking the process. They found that these melt pool features were related to defects such as balling – however, the statistical significance of these studies has not been reported [94, 95].

Chivel and Smurov [96] implemented a coaxial charge-coupled device (CCD) camera (perpendicular to the powder bed through the optical track of the machine) and a two-color pyrometer (900 nm and 1700 nm) setup to monitor the melt pool morphology (100  $\mu\text{m}$  local, focal diameter) and temperature in the powder bed fusion process. The temperature distribution and intensity of the melt pool (from processing the CCD camera data) were

correlated with the laser power. A linear trend in laser power at three levels (50 W, 100 W, 150 W) and melt pool surface temperature was observed (viz., between approximately 1800 °C and 2000 °C). In the work predating Chivel and Smurov [96], Bayle and Doubenskaia [97] used a similar setup with an IR camera along with a pyrometer with an active wavelength of 1000 nm to 1500 nm mounted on a laser powder bed fusion machine. Pyrometer readings were obtained over time for different layer thicknesses and hatch spacing settings. The IR camera was used to monitor the dynamics of melt pool particles and spatter patterns as they interacted with the laser beam.

Two recent reports by Sigma Labs described a heterogeneous sensing system to relate the thermal aspects of the LPBF process to physical properties of the part, namely, the part density (porosity) [77, 78]. One of these reports described a hardware system incorporating four *in-situ* sensors consisting of two photodetectors, one pyrometer, and one position sensor to map the sensor signatures vis-à-vis the density of titanium alloy samples made under different laser power and velocity conditions [78]. The connection between the sensor signatures and part density was made via a trademarked proprietary metric called Thermal Emission Density (TED<sup>TM</sup>). The TED<sup>TM</sup> metric is reported to have a nearly one-to-one correlation with the part density. While this work demonstrated the efficacy and need for combining data from multiple sensors for online monitoring, the mathematical details of the data fusion process were not revealed, and the statistical error was not assessed.

### 2.2.2 Layer-Wise Imaging or Staring Configuration Systems in PBF

Jacobsmuhlen *et al.* [66] implemented an image-based monitoring approach specifically for detecting build super-elevation effects. Builds are said to be super-elevated

if the prior solidified layers protrude out of a freshly deposited powder bed due to distortion. Super-elevated builds will cause the recoater to make contact with the part as the powder is raked across the bed, leading to damage to the part and/or the recoater. To detect this condition Jacobsmuhlen *et al.* coupled a CCD camera with a tilt-shift lens and mounted the camera assembly on a geared head. This setup had the ability to traverse the camera in three axes, and the tilt-shift lens allowed corrections of perspective distortions and enabled the camera to maintain focus on the powder bed.

The central theme of Jacobsmuhlen *et al.*'s work was to visually detect these super-elevated regions and compare the results with a reference, which would eventually allow adjustment of process parameters, such as laser power and hatch spacing. The experimental results of Jacobsmuhlen *et al.* indicated that super-elevations could be reduced by decreasing laser power and increasing hatch distance. By detecting the occurrence of super-elevation at an earlier stage, the layer height could be corrected, or the build could be canceled. The drawback of the cited work is that the analysis for this work used image processing techniques, namely the Hough transform and areal operations, on images (connectivity thresholding), which are exceedingly sensitive to image processing-related parameters. The ability to translate these image processing techniques to different build geometries and defects remains to be ascertained.

In a recent work, Cheng *et al.* used a near-infrared thermal camera to correlate the effect of laser scan speed and layer height on the melt pool dimensions during LPBF of Inconel 718 material [98]. The intent was to use these melt pool measurements to monitor the build condition. While the melt pool length and width were reported to change with the laser scan velocity (in three levels, 400 mm/sec, 600 mm/sec, and 800 mm/sec), the

consequence of layer height on melt pool dimensions were negligible. While very valuable and foundational towards understanding the effect of process conditions on melt pool dynamics in LPBF, in this study by Cheng *et al.*, the test artifact was a rectangular test coupon devoid of specific features. Furthermore, the test artifact was not examined for defects, such as porosity – which might result from changes in the scan velocity. This is because, the energy density (called Andrew Number) is inversely proportional to the laser velocity, and at low energy density levels the powder particles may fail to fuse together, and consequently, lead to porosity.

Krauss *et al.* [99, 100] incorporated a microbolometer-type infrared camera operating in the long wave infrared (LWIR) region, specifically in the 8,000 nm to 14,000 nm range. The IR camera was mounted on the outside of the build chamber and looked down on the powder chamber at an angle of 45° through a germanium window. This setup allowed measurement of a larger area of the powder bed, as opposed to small local areas as in coaxial measurement systems. The central theme of the authors' work was to obtain the area and morphology of the heat affected zone (HAZ). They correlated the changed in-process parameters, such as laser power, scan velocity hatch distance, and layer thickness with the melt pool area, aspect ratio (length to width ratio). These correlations served as the basis on which build quality could be monitored. For instance, the authors deliberately induced large flaws in the build (voids), as opposed to pores that typically occur in the 20-100  $\mu\text{m}$  range. The measured melt pool morphology during the defective build with induced voids was compared with an ideal state. A significant difference was reported in the irradiance profile recorded for the ideal build versus the defective build.

To reiterate, the practical applicability of these pioneering and early works is overshadowed by the offline analysis of data from a single sensor. To realize the qualify-as-you-build paradigm in AM, these foregoing studies should be coupled with emerging machine learning techniques from the big data analytics domain that can combine data from multiple sensors.

## 2.3 Experimental Setup and Data Acquisition

### 2.3.1 Measurement System and Test Artifact

This section describes the sensor suite instrumented on a commercial LPBF machine (EOS M270) at NIST. The machine was integrated with three types of sensors, namely, a shortwave infrared thermal camera, a high-speed visible camera, and a photodetector. Table 2-1 summarizes the location and relevant specifications of the sensors. The SWIR thermal camera and photodetector captured the thermal aspects of the melt pool, whereas the high-speed video camera captured its shape and surrounding spatter pattern. Photodetector data was acquired at a sampling rate of 1 MHz, in addition to frame pulses from each camera indicating the time each frame was acquired. Figure 2-1 shows the schematic and actual implementation of the setup. The detailed explanation of the setup is available in Ref. [101, 102].

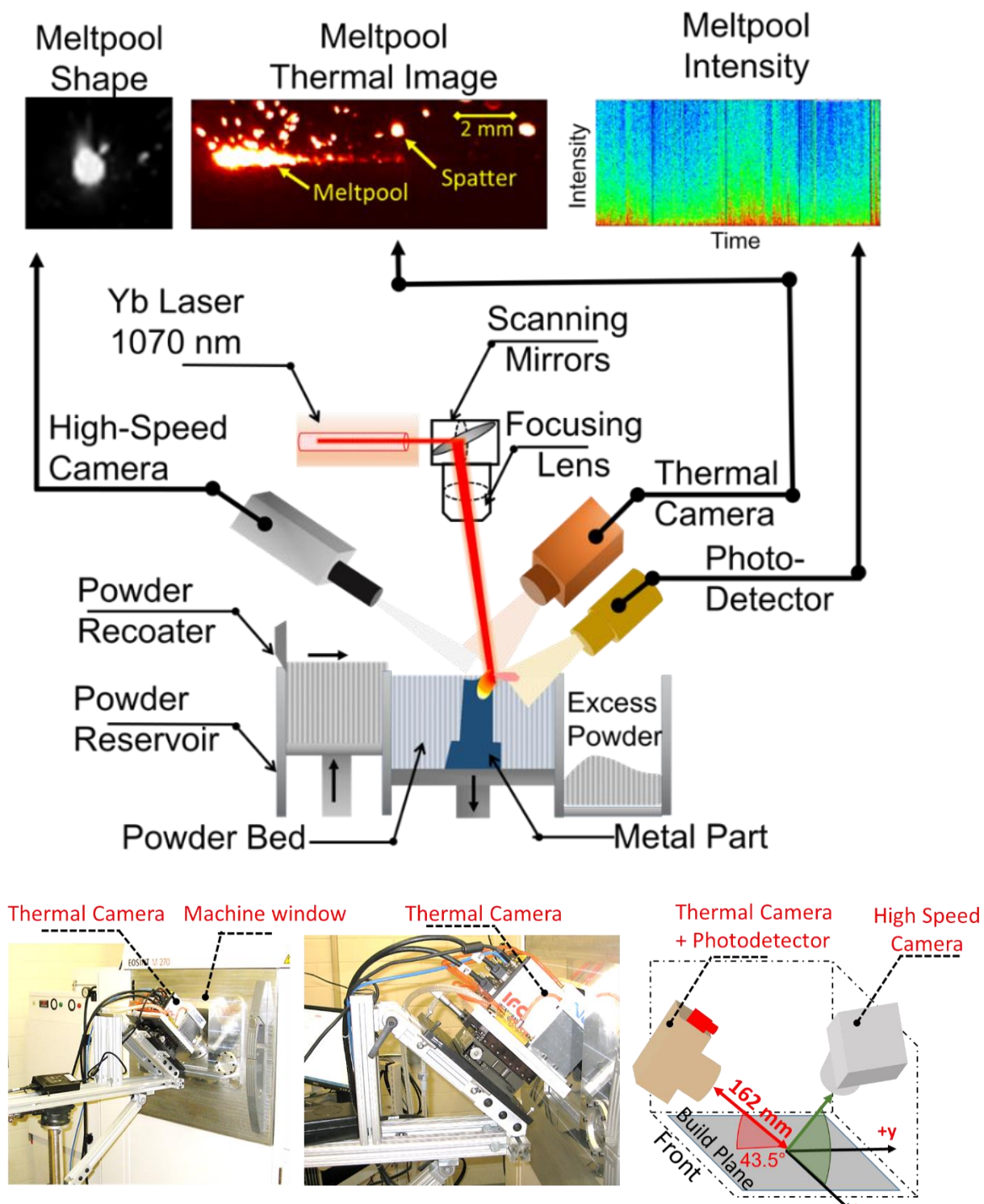


Figure 2-1: Schematic layout of sensors installed on the LPBF machine at NIST.

Table 2-1: The information related to all sensors used in the LPBF process.

Sensor	Type	Location	Details
Short Wave Infrared Thermal camera	Stirling cooled. extended range Indium Antimonide (InSb) detector with Cameralink connection. 1 megapixel.	Behind the machine door, inclined at an angle of $43.7^{\circ}$ with the build plane.	Frame rate: 1,800 frames per second. Wavelength: 1,350 nm – 1,600 nm. Shutter speed/Integration time: 40 $\mu$ s. Calibration range: [500, 1025] $^{\circ}$ C. Instantaneous field of view (iFoV): 36 $\mu$ m per pixel.
High-Speed Visible Camera	Silicon-based array. 1.2 megapixel.	Inside the build chamber (Upper right corner).	Frame rate: 4,000 frames per second.
Photodetector	Lensed. silicon-based photodiode.	Parallel with the thermal camera.	Spectral response: 300 nm to 1,200 nm. Cutoff frequency: 141.5 kHz. Sampling rate: 1 MHz.

The test artifact, which was made from nickel alloy 625 (tradename Inconel 625, UNS designation N06625), had an overhang of  $40.5^{\circ}$ , and did not include a support structure. In this work, sensor information was analyzed at three examples build heights, namely, 6.06 mm, 7.90 mm, and 9.70 mm. These example layers included the formation of the overhang structure. The process parameters are shown in Table 2-2. The overarching aim was to distinguish the thermal patterns that emerge during melting of the overhang.

The overhang here was specifically defined as being the last two scan vectors prior to or just after forming the edge, not including the pre- or post-contour scan as shown in Figure 2-2. The rest of the scans, apart from the pre- or post-contour scans, were considered to belong to the bulk volume of the part. A stripe pattern scan strategy was used and is shown in Figure 2-2(c and d); hence the laser scanned along the overhang four times (four stripes) for each layer past the 4 mm build height. The stripe orientation shifted  $90^{\circ}$  between layers, and the three example layers demonstrated a vertical stripe pattern such

that each scan vector within a stripe was horizontally aligned with the thermal camera field of view.

Admittedly, the part design studied herein was a simple unsupported overhang geometry and bereft of the complex geometrical features that could be created with LPBF. The test artifact shown in Figure 2-2 was chosen by researchers at NIST to study the physical aspects of the melt pool when building overhang geometries so that the thermal phenomena could be explained using physical modeling. The relatively compact dimensions and tractable geometry of this test artifact allowed researchers at NIST to avoid de-focusing concerns with the infrared camera – the precision of the thermal measurements would be deleteriously affected if a large object was observed, given that the field of view of the thermal camera is limited. In other words, because the sensors used in this study were not coaxial with the laser but were in the staring configuration, hence, if a bigger and more complex object was monitored, the details of the melt pool shape would be occluded due to blurring if the field of view was increased.

We reiterate that this work takes the first step in a series of forthcoming research that will focus on sensor-based monitoring of defects in AM using spectral graph theory.

Table 2-2: Scanning parameters in the LPBF of the overhang structure.

<b>Print Parameter</b>	<b>Value</b>
Hatch distance (spacing)	0.1 mm
Stripe width	4 mm
Stripe overlap	0.1 mm
Layer thickness	20 $\mu$ m
Scan speed	800 mm/s
Laser power	195 W (infill) 100 W (pre-contour) 120 W (post-contour)

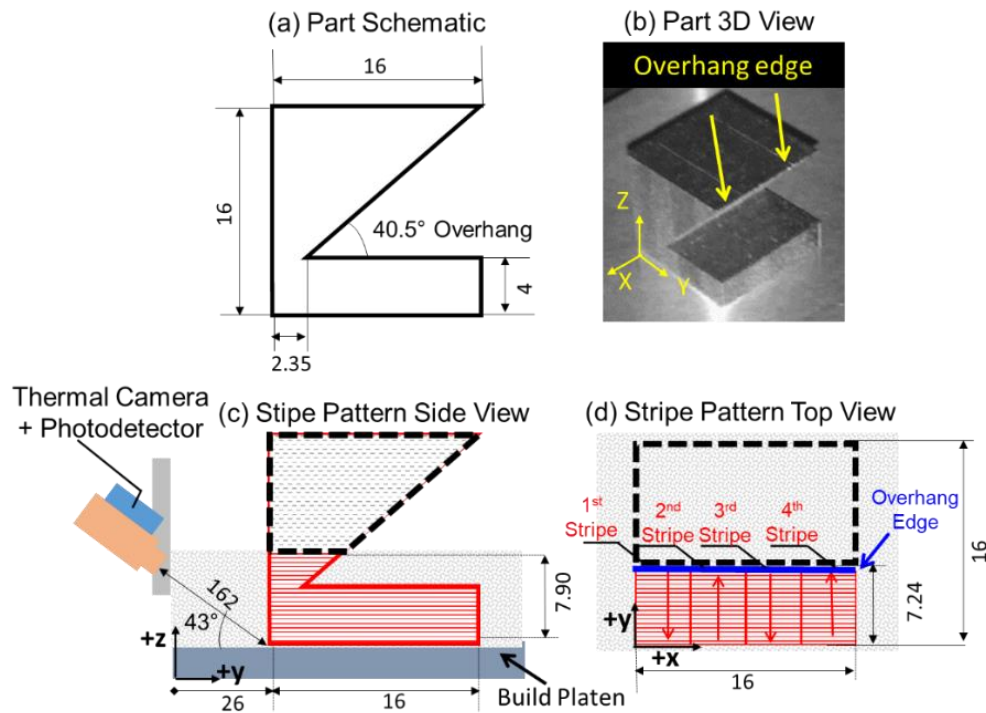


Figure 2-2: The part schematic with  $40.5^\circ$  overhang angle. (b) as-built without supports, (c and d) Side-view and top views of the stripe pattern at the build height of 7.9 mm in the context of the thermal camera position.

### 2.3.2 Visualization of the Representative Data Acquired

This section describes the qualitative differences in the three types of sensor data acquired while scanning the overhang and bulk features.

#### 1) Thermal Camera Images

Thermal video files were captured as raw 14-bit digitized data. These images were pre-processed and converted to radiance temperature values through a calibration procedure described in one of NIST articles [103]. Radiance temperature, not to be confused with true temperature, is the equivalent temperature measured if the emitting surface has an emissivity of  $\epsilon = 1$ . The image pixel values were multiplied by a factor of 10 and then stored as unsigned 16-bit integers to reduce the file size; hence there was a loss in numerical precision of  $0.1^\circ\text{C}$ . Each thermal frame was a two-dimensional matrix of 128

pixels  $\times$  360 pixels. The data captured in a frame was an average of over 40  $\mu$ s of data. This was related to the integration time (or shutter speed) of the camera. In this work, an analysis was conducted on the binary transformation of the thermal images, because the temperature recorded by the thermal camera was a radiance temperature, which had not been corrected using emissivity values to obtain the true thermodynamic surface temperature. However, this did not inhibit the analysis techniques described to observe the relative effect of build conditions on a thermal video signal.

For example, the melt pool images taken with a SWIR thermal camera (sensor) while scanning the bulk and overhang sections of a test artifact used in this work are shown in Figure 2-3(a) and (b), respectively. Figure 2-3(b) reveals that melting of the overhang section manifests in distinctive melt pool shapes[66, 67]; the melt pool for the overhang features, was roughly 1.5 times larger in length than its bulk counterpart. This was likely due to the residual heat in the overhang section stemming from the poor heat flux therein. Consequently, it was posited that correlation of the melt pool signature with the build condition facilitated in the isolation of process variation.

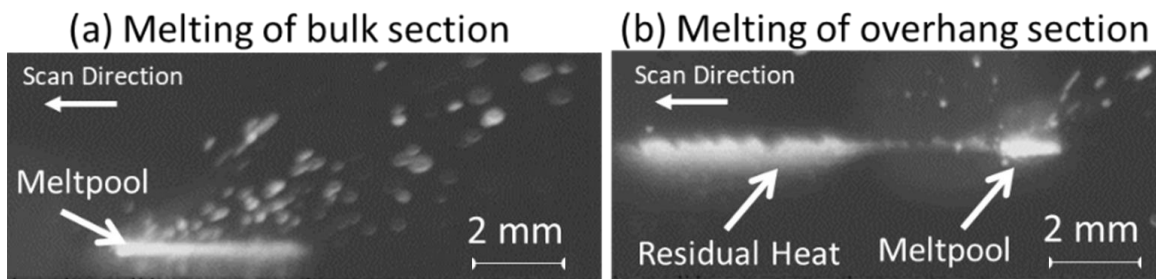


Figure 2-3: Distinctive melt pool shape for bulk and overhang areas. Note the residual heat for the overhang area resulting from the previously scanned stripe.

## 2) High-speed Visible Camera Imaging

The high-speed visible camera images were windowed to 256 pixels  $\times$  256 pixels. Images were acquired at 1,000 frames per second. Representative images for the overhang and bulk build features are shown in Figure 2-4 (a) and (b) respectively. The difference in the melt pool characteristics between overhang and bulk features in high-speed visible camera images, although discernible, was not as prominent as in the corresponding thermal images shown in Figure 2-3.

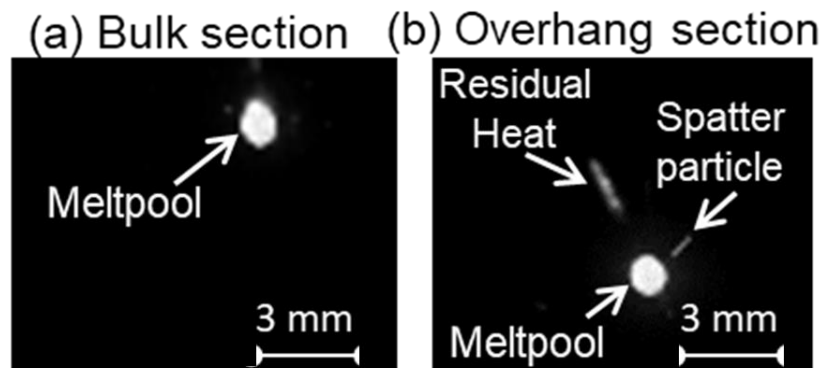


Figure 2-4: Two representative high-speed video images taken during the process. (a) bulk build conditions (b) overhang build condition corresponding to the frames in Figure 2-3.

## 3) Photodetector Signal (Time Series Data)

The photodetector signal was acquired as a time series sampled at 1 MHz; the response was in voltage. To ensure photodetector and both thermal and visible camera signals could be synchronized during analysis, both the photodetector raw signal and frame pulses (a 5 V square pulse indicating when a frame was captured) from the camera were collected on the same data acquisition system.

Furthermore, in analysis of the photodetector signal, the number of data points corresponding to the frame rate of the thermal camera must be taken into consideration. This was obtained by dividing the sampling rate of the photodetector (1 MHz) by the frame

rate of the thermal camera (1800 frames per second). This equated to 555 data points (roughly 555  $\mu$ s) measured by the photodetector within one frame period of the thermal camera. A representative trace juxtaposing the photodetector signal for the overhang and bulk build features is shown in Figure 2-5(a).

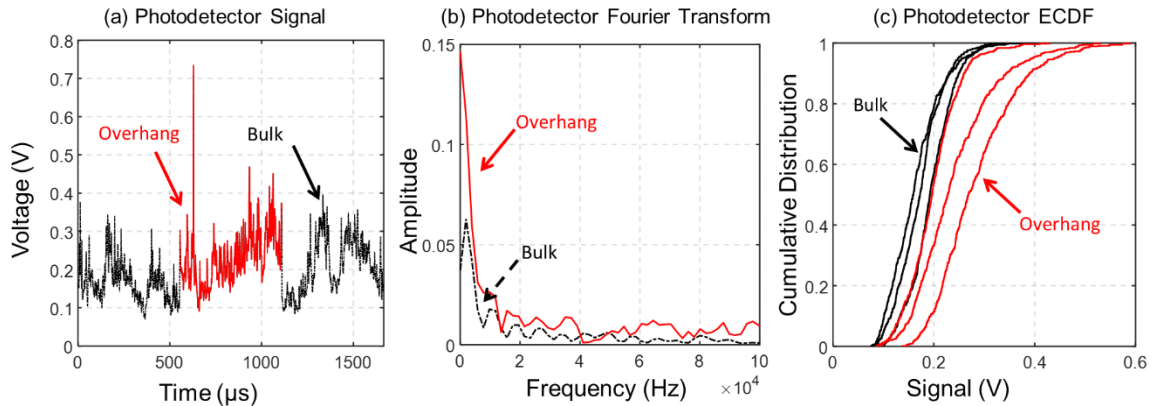


Figure 2-5: Photodetector signal windows for the overhang and bulk features. (a) intensity, (b) Fourier transform, and (c) empirical cumulative distribution function (ECDF) for three consecutive layers.

A spike in the photodetector signal for the overhang condition was observed. Some typical difficulties with using existing statistical signal processing approaches in the context of the LPBF photodetector sensor data from this work are exemplified in Figure 2-5. Figure 2-5(b) shows the Fourier transform of the same photodetector signal for the time series for the overhang and bulk features described in Figure 2-5(a). The difference in the spectral profile of the signal for the two build conditions (i.e., overhang and bulk) was scarcely distinguishable; only one clear peak was observed despite the high sampling rate (1 MHz). Analysis of the power spectrum revealed that the two build states were not statistically distinguishable.

The cumulative probability distribution of the photodetector trace for the overhang and bulk features over several frames (or 555 data points) is mapped in Figure 2-5(c). The large

shifts in the distribution shape and spread over different frames, evocative of the inherent non-stationarity of the LPBF process, curtailed any attempt to fit a fixed parametric statistical distribution to the data.

## 2.4 Proposed Methodology

The aim of this section is to develop a spectral graph-theoretic approach for analysis of multidimensional signals. This approach is used later to capture the differences in the thermal signatures during the melting of the overhang and bulk features of the test artifact shown in Figure 2-2. Application of graph-theoretic approaches for signal processing is a nascent domain with recent notable review articles by Hammond *et al.* [104], Sandryhaila *et al.* [105], and Shuman *et al.* [106, 107]. Niyogi *et al.*, in a series of seminal articles, proposed embedding high dimensional data as an undirected graph, and subsequently projecting the data into the eigenvector space of the graph Laplacian [60, 61, 108].

### 2.4.1 Previous Work in Spectral Graph Theory

This work builds upon Laboratory for Advanced Manufacturing Processes and Sensing (LAMPS) previous research in spectral graph theory for manufacturing applications [109-113]. These previous works are enumerated below.

- 1) Spectral graph theory to differentiate between different types of surfaces in ultraprecision semiconductor chemical mechanical planarization (CMP) process [109]. The spectral graph-theoretic invariant Fiedler number ( $\lambda_2$ ), viz., the second eigenvalue of the spectral graph Laplacian matrix, described later in Sec. 2.4.2 in Eq. (2-9) and (2-10), was used as a discriminant to track changes in the surface that were not detected using statistical surface roughness parameters [109].

- 2) The preceding work was extended to online monitoring of the surface finish in conventional machining. A CCD camera was used to take images of a rotating shaft as it was being machined. The machined surface images were analyzed online, and the Fiedler number ( $\lambda_2$ ) was correlated with the surface roughness [110].
- 3) The spectral graph-theoretic approach was used for detection of change points from the sensor data. The Fiedler number ( $\lambda_2$ ) from different types of planar graphs was monitored using a multivariate control chart to capture the onset of anomalous process conditions in ultraprecision machining (UPM) and chemical mechanical planarization (CMP) processes [111].
- 4) The Fiedler number was used to differentiate the geometric integrity of fused filament fabrication (FFF) AM parts made using different materials [113] based on laser-scanned point cloud data. This work was further extended to parts made under different FFF conditions using several spectral graph Laplacian eigenvalues and not just the Fiedler number.

This work differs from the authors' previous works in the following manner. It is the first to report the application of Laplacian eigenvectors for the diagnosis of process conditions in AM. The approach is integrated within a learning framework for online monitoring of process conditions. None of the previous studies by the authors had an online learning capability for state detection from sensor signals. This is not a trivial extension because the Laplacian eigenvectors present a multi-dimensional challenge to classification. Furthermore, the previous works were based on converting a signal into an unweighted and undirected graph. This required using thresholding functions, which in turn led to loss of information. In this current work, such a threshold is not required as the graph constructed

is of the weighted and undirected type. A brief overview of the approach is provided in the forthcoming Sec. 2.4.2.

### 2.4.2 Overview of the Approach

Before describing the mathematical intricacies of the approach, a high-level overview is provided. The mathematical convention is to denote matrices and vectors with bold typesets. Suppose a sequence of sensor data,  $\mathcal{X}$  (time series or images) is gathered from a process. Further, consider that the process manifests in  $n$  different known process conditions or build states labelled as  $s_1, s_2, s_i \dots s_n$ . In LPBF these states could refer to different process conditions, such as melting of bulk, overhang, thin sections, etc. This allows the sensor data  $\mathcal{X}$  associated with each condition  $s_i$  to be represented with the symbol  $\mathbf{x}_i$ . The aim is to identify the system state  $s_i$  from which an unlabeled signal  $y$  is observed (i.e., if a signal  $y$  is observed, the purpose is to find the process condition  $i$  to which it belongs). From the LPBF perspective, for instance, the intent is to conclude from one frame of the high-speed video camera whether there is an impending build failure; or given a photodetector signal sample, infer if the onset of distortion is imminent. The signal  $\mathbf{x}_i$  can take various forms depending on the type of sensor data acquired.

- Temporal data  $[\mathbf{x}_i]^{m \times d}$  where each column of  $\mathbf{x}_i$  is a type of sensor, and each row is a measurement in time  $t = \{1 \dots m\}$  for the  $d$  sensors; each  $a_j^t$  is a data point for sensor  $j = \{1 \dots d\}$  at time instant  $t$ . In the context of LPBF this matrix could represent multiple photodetector signals acquired simultaneously, where each column of  $\mathbf{x}_i$  is the data from a photodetector. It is restated that  $\mathbf{x}_i$  is associated with a specific process state  $s_i$ .

$$\mathbf{x}_i = \begin{bmatrix} a_1^1 & a_1^2 & \dots & a_1^d \\ a_t^1 & & \ddots & a_t^d \\ \vdots & & & \vdots \\ a_m^1 & \dots & & a_m^d \end{bmatrix} \quad (2-1)$$

- Spatiotemporal data such as high-speed visible camera or thermal camera, where each  $\mathbf{x}_i^t$  is an image frame captured at time instant  $t$  for a state  $i$ . The matrix  $\mathbf{x}_i$  must be further qualified with a time index  $t$  because data is acquired in discrete frames. Thermal and video camera data are in such a format; the signal in this instance is a three-dimensional array. Each  $\mathbf{x}_i^t$  is an array of image pixels. For a frame of a thermal camera image, each pixel corresponds to the intensity of light converted to a radiant temperature value using the thermal calibration; for the high-speed video camera each pixel records the intensity of light.
- Purely spatial point cloud data where  $\mathbf{x}_i$  contains information of coordinate related to the locations. An example is the 3D point cloud data, such as those obtained from a laser or structured light scanner. This information is obtained as spatial coordinate indexed information.

The approach involves the following three broad steps (see Figure 2-6); the detailed steps and mathematics are explained later.

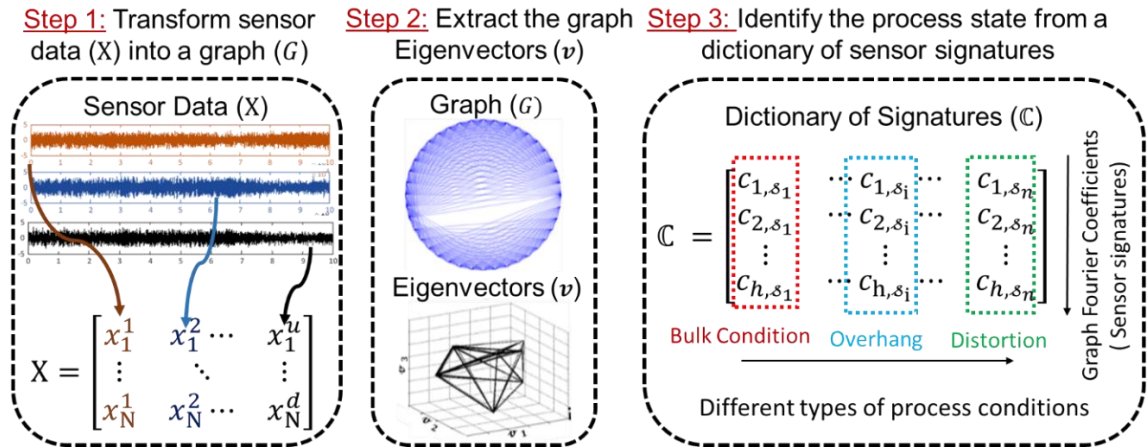


Figure 2-6: The three steps in the proposed spectral graph-theoretic approach.

Step 1: Transform the signals  $x_i$  corresponding to each pre-labeled state  $s_i$  into an undirected, weighted network graph  $G_i(V, E, W)$ , where  $V$  and  $E$  are the vertices and edges of the graph and  $W$  is the weight between the edges.

Step 2: The spectral graph Laplacian matrix  $\mathcal{L}_i$  is computed from the graph  $G_i$ . The first non-zero  $n$  graph Laplacian eigenvectors  $v_i$  are used as an orthogonal basis set corresponding to the process state  $s_i$ .

Step 3: Each  $x_i$  is decomposed by taking an inner product  $x_i^T \cdot v_i$  akin to a Fourier transform into a set of coefficients  $c_i$  called graph Fourier coefficients.

- The graph Fourier coefficients are written in block matrix form as  $\mathbb{C} = [[c_1^T] \ [c_2^T] \ \dots \ [c_i^T] \ \dots \ [c_n^T]]$  corresponding to different states  $s_1, s_2, s_i \dots s_n$ . The matrix  $\mathbb{C}$  is called the *dictionary*.
- Given an unlabeled signal  $y$ , an inner product  $p_i = y^T \cdot v_i$  is taken with each of the  $n$  basis vector sets one at a time; where  $n$  are the different states. The matrices  $p_i^T$  are called the candidate coefficients. Each  $p_i^T$  is compared with the corresponding  $c_i^T$  in

the dictionary  $\mathbb{C}$  in terms of the squared error  $e_i$ . The comparison resulting in the least error is the designated state of  $y$ .

The advantages of the approach are as follows:

1. The graph Fourier transform eschews intermediate signal filtering steps and accommodates multi-dimensional signals. It does not require mining statistical features, such as mean, standard deviation, etc., from the data. Hence the presented approach is feature-free. Given an unlabeled signal  $y$  belonging to an unknown state  $s_i$ , a computationally simple inner product is needed for classification. This is apt for online monitoring applications.
2. The approach does not require *a priori* defined basis functions akin to the sinusoidal basis for the Fourier transform; nor does it rely on a predefined probability distribution as in typical stochastic modeling schemas; and lastly the need for a rigid model structure is eliminated (e.g., number of hidden layers and nodes in a neural network).

The disadvantages of this approach are:

1. As with all supervised classification models, a pre-labeled data set is needed.
2. All the sensor data  $[\mathbf{x}_i]^{m \times d}$ , if they are temporal sensors, must have the same sampling rate. This assumption can be relaxed by signal smoothing steps.

Frequent symbols and notations are noted in Table 2-3. Each of the three steps of the approach is next described in detail.

Table 2-3: List of major mathematic symbols and notations used in this work.

Symbol	Description
$\mathcal{X}$	Sequence of sensor data (time series or images)
$\mathcal{s}_1, \mathcal{s}_2, \mathcal{s}_i \dots \mathcal{s}_n$	Process conditions or build states
$\mathbf{x}_i$	Sensor data $\mathcal{X}$ associated for each state $\mathcal{s}_i$
$p \in \{1 \dots h\}$	Number of windows
$q \in \{1 \dots k\}$	Length of windows
$\vec{\mathbf{x}}_q, \vec{\mathbf{x}}_r$	Two rows of the signal window $\mathbf{x}_i^p$
$w_{qr}$	Pairwise comparison of $\vec{\mathbf{x}}_q$ and $\vec{\mathbf{x}}_r$
$G_i(V, E, W)$	Undirected, weighted graph with, nodes $V$ , edges $E$ and weights $W$
$\mathbf{S}$	Symmetric similarity matrix
$\mathbf{D}$	Diagonal degree matrix
$\mathcal{L}_i$	Spectral graph Laplacian matrix for each state $\mathcal{s}_i$
$\mathbf{v}_i$	Graph Laplacian eigenvectors
$\mathbf{V}_{\mathcal{s}_i}$	Single universal basis for a system $\mathcal{s}_i$
$n$	The number of eigenvectors in the universal basis
$G(\mathcal{X})$	Spectral graph transform on a signal $\mathcal{X}$
$\mathbb{C}$	Graph Fourier coefficients
$\mathbb{P}$	Candidate coefficients
$e_{\mathcal{s}_1}$	Sum of square errors for classification of a system $\mathcal{s}_i$

1) *Step 1: Converting a signal into a Network Graph.*

The aim of this step was to represent a sequence  $\mathcal{X}$  of sensor data (time series, images) as a weighted, undirected network graph  $G$ , i.e., achieve the mapping  $\mathcal{X} \mapsto G(V, E, W)$  with nodes (vertices)  $V$ , edges (links)  $E$ , and edge weights  $W$ . The graph  $G(V, E, W)$  is a lower dimensional representation of  $\mathcal{X}$ . Consider an  $m$ -data point long signal  $\mathbf{x}_i$  corresponding to a known state  $s_i$ ,  $i = \{1 \dots n\}$  as per the matrix shown in Eq. (2-1). This signal is divided into  $h$  windows of length  $k (= m/h)$  data points each. Let each window be represented as a  $k \times d$  matrix  $\mathbf{x}_i^p$ ,  $p \in \{1 \dots h\}$ ,  $\mathbf{x}_i$  is written in block matrix form as,

$$\mathbf{x}_i = \begin{bmatrix} \mathbf{x}_i^1 \\ \vdots \\ \mathbf{x}_i^p \end{bmatrix} \quad (2-2)$$

For each  $\mathbf{x}_i^p$  the following graph transform procedure is followed. First, pairwise comparisons  $w_{ij}$  are computed using a kernel function  $\Omega$ ; in Eq. (2-3),  $\vec{\mathbf{x}}_q$  and  $\vec{\mathbf{x}}_r$  are two rows of the signal window  $\mathbf{x}_i^p$

$$w_{qr} = \Omega(\vec{\mathbf{x}}_q, \vec{\mathbf{x}}_r) \quad \forall q, r \in (1 \dots k). \quad (2-3)$$

Different types of kernel functions  $\Omega$  may be used, such as the Gaussian (Eq. (2-4)) and Mahalanobis (Eq. (2-5)) kernel shown below:

$$w_{qr} = e^{-\left[\frac{\|\vec{\mathbf{x}}_q - \vec{\mathbf{x}}_r\|}{\sigma}\right]^2} \quad (2-4)$$

$$w_{qr} = (\vec{\mathbf{x}}_q - \vec{\mathbf{x}}_r) C^{-1} (\vec{\mathbf{x}}_q - \vec{\mathbf{x}}_r) \quad (2-5)$$

The weight of an edge connecting a node  $q$  with another node  $r$  is  $w_{qr}$ . It is apparent that the topology of the graph  $G$  depends on the kernel  $\Omega$ . In this work, the Mahalanobis kernel, Eq. (2-5) with  $C$  as the variance-covariance matrix is used exclusively. The mathematical implication of using the Mahalanobis kernel is as follows:

$$\lim_{\vec{x}_q - \vec{x}_r \rightarrow 0} w_{qr} = 0 \quad (2-6)$$

In other words, given two data points  $\vec{x}_q$  and  $\vec{x}_r$ , the more similar  $\vec{x}_q$  and  $\vec{x}_r$  are, the *weaker* is the connection between the two. The symmetric *similarity matrix*  $\mathbf{S}^{k \times k} = [w_{qr}]$  represents a weighted and undirected network graph  $G$ ; each row and column of  $\mathbf{S}^{k \times k}$  is the vertex  $V$  (or node) of the graph, and the relationship between two nodes is indexed by edges, in terms of its connection status  $E$ , and weight  $W$ . The graph is then represented as  $G \equiv (V, E, W)$ . The following notational additions are made:  $\mathbf{S}_{x_i^p}$  and  $G_{x_i^p}$ , where  $x_i^p$  relates to a specific window  $x_i$  for the signal  $p$ .

An analogy can be drawn between a graph network with an electrical circuit with resistors. Indeed, there is an equivalence in literature between the Laplacian Matrix and the Kirchhoff Matrix of electrical circuits [114]. The node  $V$  of a graph corresponds to the node or common point in the circuit; the edge  $E$  of the graph is a branch in the circuit; and the resistance on the branch is the weight  $W$ . The smaller the weight of the edge connecting two nodes, the smaller the resistance between them.

Knowing that the electric current takes the path of shortest resistance, an electrical network can be characterized in terms of the path taken by the current; if the resistance along a branch changes, the path taken may also change. Hence, by tracking changes in the

path taken by the current, drastic changes that may have occurred in the circuit can be detected. This very idea carries over to the presented approach. A signal is redrawn as a graph and the different paths on a graph are tracked in terms of the eigenvectors of the Laplacian Matrix.

2) *Step 2: Extracting topological information for the graph surface*

The aim of this step was to extract topological information from the graph  $G$ . Once the data  $x_i^p$  in a particular window is represented as a graph  $G_{x_i^p}$ , the Laplacian eigenvectors are computed. This topological information is subsequently used to capture the process dynamics contained in the signal  $x_i$ . Going back to  $x_i^p$ , the *degree*  $d_q$  of a node  $q$ ,  $q = \{1 \dots k\}$  is computed, which is a count of the number of edges that are incident upon the node. The node degree is the sum of each row in the similarity matrix  $\mathbf{S}^{K \times K}$  and the diagonal *degree matrix*  $\mathbf{D}$  structured from  $d_q$  is obtained as follows,

$$d_q = \sum_{r=1}^k w_{qr} \quad \forall q, r = \{1 \dots k\} \quad (2-7)$$

$$\mathbf{D}^{k \times k} \stackrel{\text{def}}{=} \text{diag}(d_1, \dots, d_k). \quad (2-8)$$

This leads to the normalized Laplacian  $\mathcal{L}_n$  of the graph  $G$ , which is defined as,

$$\mathcal{L}_n \stackrel{\text{def}}{=} \mathbf{D}^{-\frac{1}{2}} \times (\mathbf{D} - \mathbf{S}) \times \mathbf{D}^{-\frac{1}{2}}, \quad (2-9)$$

where,  $\mathbf{D}^{-\frac{1}{2}} = \text{diag}\left(\frac{1}{\sqrt{d_1}}, \dots, \frac{1}{\sqrt{d_k}}\right)$ .

An alternative is the random walk Laplacian  $\mathcal{L}_r$  of the graph  $G$  defined as,

$$\mathcal{L}_r \stackrel{\text{def}}{=} \mathbf{D}^{-1} \times (\mathbf{D} - \mathbf{S}), \quad (2-10)$$

Simplifying the notation, both Laplacians are represented with the symbol  $\mathcal{L}$ . Thereafter, the eigenspectrum of  $\mathcal{L}$  is computed as,

$$\mathcal{L}\mathbf{v} = \lambda^*\mathbf{v}. \quad (2-11)$$

At the end of Step 2 a spectral graph transform on a signal  $\mathcal{X}$  is defined;

$$G(\mathcal{X}) \rightarrow \mathcal{L}_{\mathcal{X}}(\lambda^*, \mathbf{v}). \quad (2-12)$$

In other words, the information in the signal  $\mathcal{X}$  was captured in the form of the eigenvectors ( $\mathbf{v}$ ) and eigenvalues ( $\lambda^*$ ) of the Laplacian matrix.

### 3) Step 3: Classification of Process States

The aim of this step was to find out or classify the process state  $s_i$ , given a signal  $y$ . For instance, given a frame of the thermal image, the intent was to ascertain if there was an impending build fault. This is a type of a supervised classification approach, where a set of labeled data is assumed to exist *a priori*. This presumption of labeled data is one of the disadvantages of this approach. It will be relaxed with new graph-theoretic unsupervised learning approaches in the authors' future work.

Step 3.1: This step applied the graph transform from Eq. (2-12) to the signal  $x_i$  corresponding to a state  $s_i$ , as follows, where  $h$  is the number of windows in the signal,

$$G(\mathbf{x}_i) = \begin{bmatrix} \mathcal{L}_{x_i^1} \\ \vdots \\ \mathcal{L}_{x_i^h} \end{bmatrix}. \quad (2-13)$$

This means that the signal  $\mathbf{x}_i^p$  corresponding to a state  $s_i$ , at window  $p$  is associated with a Laplacian eigenvector basis  $\mathbf{v}_{x_i^p}$  through the spectral graph transform. Each  $\mathbf{v}_{x_i^p}$  is a  $k$ -long column vector.

Step 3.2: Next, the aim was to learn a single universal basis  $\mathbf{V}_{s_i}$  for a system  $s_i$  as data is continuously acquired (consider that the signal  $\mathbf{x}_i$  arrives in discrete chunks as a window). This was done through a simple update schema, akin to the delta update rule frequently used in machine learning [115]. For each window, the basis vectors are updated as follows,

$$\mathbf{V}_{x_i^{p+1}} = \mathbf{v}_{x_i^p} + \Delta (\mathbf{v}_{x_i^{p+1}} - \mathbf{v}_{x_i^p}), p = \{1 \dots h\} \quad (2-14)$$

initialized with  $\mathbf{V}_{x_i^1} = \mathbf{v}_{x_i^1}$  with  $\Delta$  set to a small value ( $\Delta = 0.01$  in this work). To make the process computationally simpler a smaller subset of the Laplacian eigenvalues was updated; typically, the first 10 non-zero eigenvectors of the Laplacian  $\mathcal{L}_{x_i^p}$  were found to be adequate. Hence, the universal basis  $\mathbf{V}_{s_i}^{k \times n}$  is the matrix obtained when  $\mathbf{V}_{x_i}$  converges, that is  $\mathbf{V}_{s_i} = \mathbf{V}_{x_i^h}$ , where  $n$  is the number of non-zero eigenvectors updated.

Step 3.3: The spectral graph Fourier transform, which is analogous to the discrete Fourier transform is now defined. A spectral graph Fourier transform  $\hat{G}(\cdot)$  on a signal  $\mathbf{x}^{N \times 1}$  (consider  $d = 1$  for simplicity) can be defined assuming that the Laplacian matrix ( $\mathcal{L}$ ) is not defective (i.e., the graph has no isolated nodes) as follows,

$$\begin{aligned} \hat{G}(\mathbf{X}) &= [\mathbf{x}^T \cdot \mathbf{V}_1 = c_1 \quad \dots \quad \mathbf{x}^T \cdot \mathbf{V}_N = c_N] \\ \mathbf{x} &= \sum_{i=0}^{i=n} \hat{G}(\mathbf{x}) \cdot \mathbf{V}_i \end{aligned} \quad (2-15)$$

Applying this analogy to the signal  $x_i$  across each of the  $h$  windows by taking the product  $(\mathbf{x}_i^p)^T \cdot \mathbf{V}_{s_i} \forall p = \{1 \dots h\}$  leads to the coefficient matrix  $\hat{G}(\mathbf{x}_i)$ .

$$\hat{G}(\mathbf{x}_i) = \left[ [(\mathbf{x}_i^1)^T (\mathbf{V}_{s_i}) = \mathbb{C}_{1,s_i}^{d \times n}] \quad \dots \quad [(\mathbf{x}_i^h)^T (\mathbf{V}_{s_i}) = \mathbb{C}_{h,s_i}] \right] \quad (2-16)$$

Essentially, each term  $\mathbb{C}_{p,s_i}$  is a matrix that is  $d \times n$  long, where  $n$  is the number of eigenvectors in the universal basis  $\mathbf{V}_{s_i}$  selected for analysis; the universal basis  $\mathbf{V}_{s_i}$  has dimensions  $k \times n$ . If this procedure is repeated for all  $n$  systems  $s_1 \cdots s_n$ , then a dictionary of coefficients can be formed, written in block matrix form  $\mathbb{C}^{(h \times n)}$ , and partitioned by  $\mathbb{C}_{1,s_i}^T$  each of which has dimensions  $n \times d$ :

$$\mathbb{C}^{(h \times n)} = \begin{bmatrix} \mathbb{C}_{1,s_1}^T & \cdots & \mathbb{C}_{1,s_i}^T & \cdots & \mathbb{C}_{1,s_n}^T \\ \mathbb{C}_{2,s_1}^T & \cdots & \mathbb{C}_{2,s_i}^T & \cdots & \mathbb{C}_{2,s_n}^T \\ \vdots & & \vdots & & \vdots \\ \mathbb{C}_{h,s_1}^T & \cdots & \mathbb{C}_{h,s_i}^T & \cdots & \mathbb{C}_{h,s_n}^T \end{bmatrix} \quad (2-17)$$

Step 3.4: Given an unknown signal  $\mathbf{y}$  with  $k \times d$  data points, an inner product  $(\mathbf{y})^T \cdot \mathbf{V}_{s_i}$  is taken with each of the  $n$  universal basis vector sets  $\mathbf{V}_{s_i}$  one at a time. This gives a *candidate set* populated by block matrices  $[\mathbf{p}_{s_i}]^{d \times n}$ , as follows,

$$\mathbb{P} = [[\mathbf{p}_{s_1}^T], \cdots [\mathbf{p}_{s_n}^T]]. \quad (2-18)$$

Step 3.5: The next step was to compare each of the candidate block matrices  $\mathbf{p}_{s_1}$  with the dictionary of coefficients  $\mathbb{C}_{p,s_i}$  in Eq. (2-17) having the corresponding label  $s_i$ . In other words, find the error between  $\mathbf{p}_{s_i}$  and corresponding  $\mathbb{C}_{p,s_1} \forall p$ . This is done by taking the sum of square errors,

$$e_{s_1} = \sum_{p=1}^{p=h} \|(\mathbb{C}_{p,s_i}^T - \mathbf{p}_{s_i}^T)\|^2. \quad (2-19)$$

The label assigned to  $\mathbf{y}$  is the one which has the minimum sum of square errors, i.e.,  $\operatorname{argmin}_{s_i} e_{s_i}$ .

### 2.4.3 Application of the Approach to Synthetically Generated Signals.

The aim of this section is to test the efficacy of the spectral graph approach in classifying signals from a nonlinear deterministic Rössler time series [116]. The Rössler system  $\varphi(t; a, b, c)$  shown below in Eq. (2-20) is a set of interlinked nonlinear differential equations, whose behavior is governed by three constants:  $a$ ,  $b$ , and  $c$ . A slight change in these constants leads to markedly different behavior of the system. It is an archetypical nonlinear dynamic system, which shows sensitivity to initial conditions. Four types of systems were generated by setting the constant  $a$  to four different values, namely,  $a = 0.16$ ;  $0.17$ ;  $0.19$ ; and  $0.21$ . These four systems were labelled  $s_1$ ,  $s_2$ ,  $s_3$ , and  $s_4$ . The generated signals were 20,000 data points long for each  $x(t)$ ,  $y(t)$ , and  $z(t)$ , which were initialized at  $\{0,0,0\}$ . Each  $x(t)$ ,  $y(t)$  and  $z(t)$  was considered a signal, each of which occupied one column in Eq. (2-1). Different values of the constant  $a$  led to different  $\varphi(t)$ .

The following procedure was used: four different levels of Gaussian white noise ( $\eta$ ) were added to the system;  $\eta = \{0.5\%, 10\%, 20\%\}$ . From each of the four systems 125 samples each 20,000 data points long were selected. Referring to Eq. (2-1), the dimensions are  $d = 3$  for the Rössler system, and  $m = 20,000$ . Three different window sizes of length  $k = 500, 750$ , and  $1000$  data points were evaluated. The classification fidelity on applying the graph-theoretic approach in terms of the F-score was recorded. The F-score is an aggregate measure of the statistical Type I (false alarm) and Type II (failing to detect) errors. The higher the F-score the better. The process was repeated five times, i.e., a five-fold replication study. The result from this analysis is shown in terms of the F-score contingent on the noise level ( $\eta$ ) and window size in Table 2-4.

$$\varphi(t; a, b, c) = \left\{ \begin{array}{l} \frac{d}{dt} \mathbf{x}(t) = -(\mathbf{y}(t) + \mathbf{z}(t)) \\ \frac{d}{dt} \mathbf{y}(t) = \mathbf{x}(t) + a\mathbf{y}(t) \\ \frac{d}{dt} \mathbf{z}(t) = b + \mathbf{x}(t) \cdot \mathbf{z}(t) - c\mathbf{z}(t) \end{array} \right\} \quad (2-20)$$

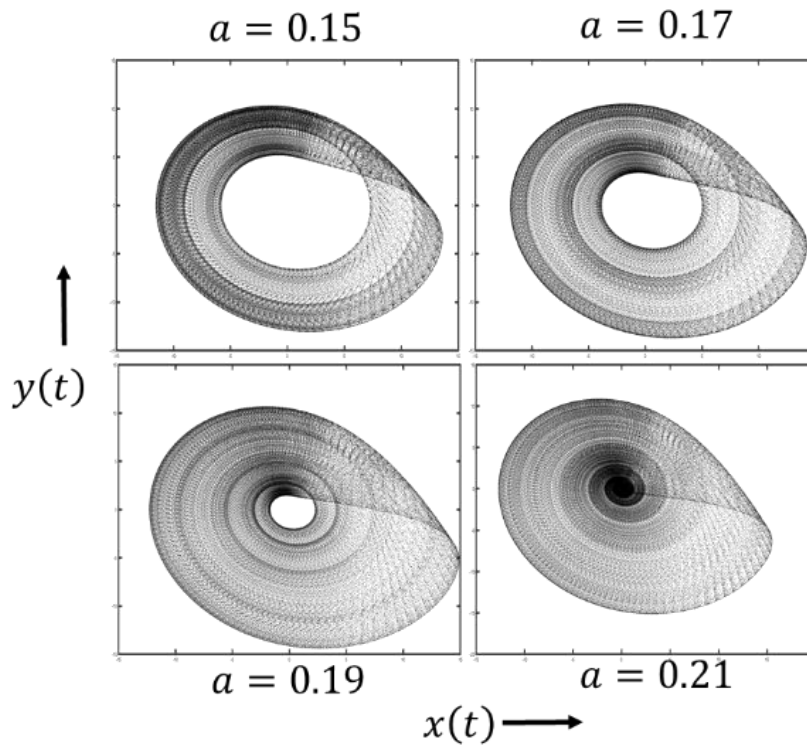


Figure 2-7: The four different Rössler systems used for testing the approach.

From Table 2-4 it is evident that window  $k = 750$  gave a consistently higher F-score. Remarkably, the addition of noise to the system did not lead to significant changes in the F-score, which underscored the robustness of the proposed approach to noise. The reason a window size of  $k = 750$  led to the best results is because it was neither too short to be afflicted with temporal correlation, nor too large to be affected by noise. The so-called confusion matrix for  $k = 750$  is shown in

Table 2-5 along with a sample calculation for the F-score. The approach is compared against seven other popular classifiers in Table 2-6.

The inputs to these classifiers are eight statistical moments: mean, median, standard deviation, skewness, kurtosis, minimum, maximum, and inter-quartile range. These features were extracted for each of the three components,  $x(t)$ ,  $y(t)$ , and  $z(t)$ , of the Rössler system, and principal components (capturing 99% of the variation) are used within the seven different machine learning approaches. The results presented in Table 2-6, indicate that the proposed approach with Laplacian eigenvectors outperforms these other approaches.

Table 2-4: Evaluation of the proposed approach for the Rössler system. Percentage F-score results (higher the better) for distinguishing between the four Rössler systems. The numbers in parenthesis are the standard deviations from a five-fold classification study.

Noise Level ( $\eta\%$ )	Window Sizes ( $k$ in Eq. (2-2))		
	$k = 500$	$k = 750$	$k = 1000$
$\eta = 0\%$	0.8 (0.05)	0.83 (0.04)	0.81 (0.04)
$\eta = 10\%$	0.77 (0.02)	0.83 (0.05)	0.84 (0.03)
$\eta = 15\%$	0.77 (0.05)	0.83 (0.04)	0.81 (0.04)
$\eta = 20\%$	0.74 (0.04)	0.83 (0.03)	0.79 (0.05)

Table 2-5: The confusion matrix for distinguishing the four Rössler systems.

		Predicted Process Condition				False Negative Rate (FNR, Type II error)
		$\delta_1$	$\delta_2$	$\delta_3$	$\delta_4$	
Actual Process Condition	$\delta_1$	122	3	0	0	3/125 = 2.4%
	$\delta_2$	26	93	6	0	32/125 = 25.6%
	$\delta_3$	5	11	99	10	26/125 = 20.8%
	$\delta_4$	0	0	23	102	23/125 = 18.4%
False Positive Rate (FPR, Type I error)		31/375 = 8.2%	14/125 = 11.2%	29/125 = 23.2%	10/125 = 8%	Avg. FNR ( $\beta$ ) = 16.8% Avg. FPR $\alpha = 12.5\%$
F-score = $1 - 2 \frac{\alpha + \beta}{\alpha \times \beta} = 0.821$ (82.1%)						

Table 2-6: Comparing the graph-theoretic approach against six other approaches. The numbers in the table are the F-scores (larger is better) along with the standard deviation over five replications in the parentheses.

Noise Level ( $\eta$ )	Classifier							
	Linear Discriminant (LD)	K-Nearest Neighbors (KNN)	Decision Tree	Support Vector Machines (SVM)	Boosted Trees (BT)	Neural Network (NN)	Quadratic Discriminant Analysis (QDA)	Proposed Graph-Theoretic Approach
0%	0.81(0.01)	0.79(0.02)	0.76(0.03)	0.83(0.02)	0.80 (0.02)	0.79 (0.01)	0.81(0.01)	0.83 (0.04)
10%	0.74 (0.01)	0.63(0.02)	0.72(0.03)	0.75 (0.03)	0.78 (0.02)	0.75 (0.02)	0.78 (0.02)	0.83 (0.05)
15%	0.73(0.02)	0.6 (0.03)	0.77(0.02)	0.72 (0.03)	0.78 (0.02)	0.73 (0.02)	0.75 (0.02)	0.83 (0.04)
20%	0.72(0.03)	0.58(0.04)	0.7 (0.04)	0.7 (0.04)	0.75 (0.02)	0.72 (0.03)	0.75 (0.02)	0.83 (0.03)

## 2.5 Results and Discussions

The aim of this section is to apply the spectral graph approach described in Sec. 2.4 to discriminate between the overhang and bulk build conditions. Data from each of the three type of signals, thermal images, high-speed video frames and the photodetector time traces were analyzed, and their ability to distinguish between the two build conditions (overhang and bulk) was statistically assessed in terms of the F-score. A critical parameter that needed to be determined *a priori* was the window length  $k$ . In the thermal video and IR images the window size was 1 frame; for the photodetector, the window size was selected to be 555 data points (acquired over a time interval of 555  $\mu$ s) long to correspond to one thermal image frame, as explained before.

For the thermal and video images, each pixel row corresponded to a row on the matrix  $x_i$ , shown in Eq. (2-1), whereas, the photodetector signal was a column vector. Using Eq. (2-5), the weight matrix  $w_{qr}$  was obtained, and the steps in Eq. (2-7) – Eq. (2-9) were followed. This gave the eigenspectrum  $(\lambda^*, v)$ . The eigenvalues  $\lambda^*$  were plotted to illustrate visually the manner in which the signals for different build conditions, namely, the melting

of overhang and bulk features, were distinguishable in the spectral graph domain. These plots are shown in Figure 2-8, based on which of the following inferences were drawn:

- Figure 2-8 (a) traces the second eigenvalue ( $\lambda_2$ ), also called the Fiedler number, across 5000 thermal camera frames for one layer (9.70 mm layer height) of the process. Distinctive peaks are evident in the plot where the overhang sections were built. The smoothed trend line in the figure was obtained using a seventh order Savitzky-Golay filter taken over a window size of 101 data points to accentuate the patterns in the data.
- Corresponding to the same 5,000 frames in Figure 2-8 (a), in Figure 2-8 (b) the  $L^2$  norm of the eigenvalues ( $\lambda^*$ ) is given by  $\|\lambda_2^2, \lambda_3^2, \dots, \lambda_k^2\|$  for the photodetector signal. This is because the Fiedler number alone failed to show any clear peaks. The trends were not as visually prominent as those obtained from the thermal camera. Indeed, some of the peaks in the photodetector signal did not seem to align with those of the thermal camera. This was most likely due to the sensitivity of the photodetector to the direction of the scan. As the laser melted material nearer to the photodetector, higher amplitude peaks were observed, compared to the instances where the laser was farther away. A count of the (periodic) peaks in Figure 2-8 (b) reveals that they correspond to the number of hatches. Given this variation in the signal characteristics it is reasonable to expect a lower detection fidelity for the photodetector signal compared to the thermal camera.

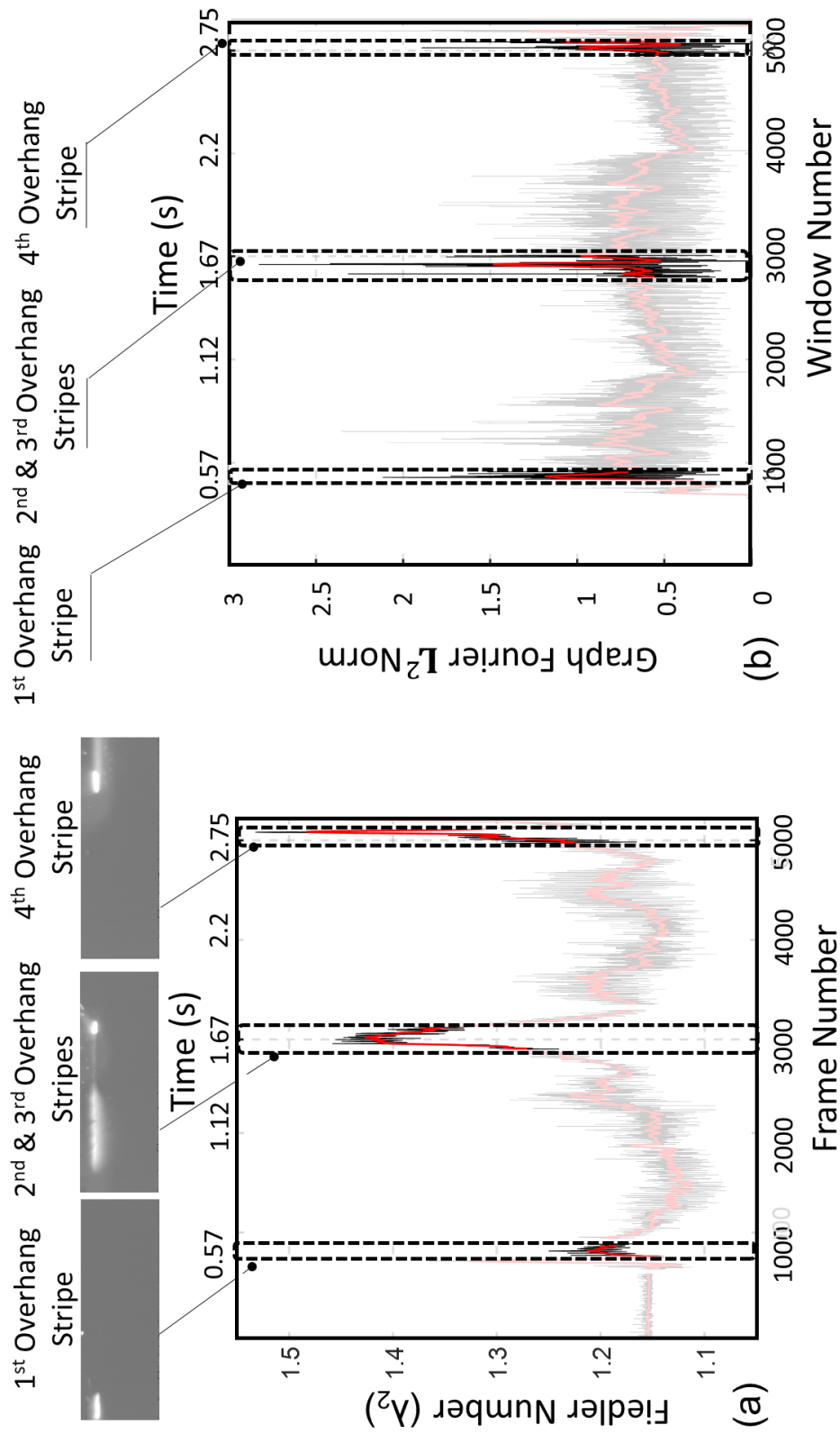


Figure 2-8: Fiedler number pattern for the various signals.  
 (a) One frame of the thermal camera (b) Second norm of graph Fourier coefficients of photodetector.

Continuing with the analysis, the approach was applied to the data acquired by the three sensors for distinguishing between the overhang and bulk build conditions. The approach was compared against seven other popular machine learning approaches following the procedure described in Sec. 2.4.3. For brevity, the parameter settings are encapsulated in the Appendix, noting that for the photodetector signal, the random walk Laplacian for Eq. (2-11) was used. Table 2-7 represents the performance of the spectral analysis algorithm for all three types of sensor signals in terms of F-score value. Based on Table 2-7 and

Table 2-8 the following inferences are tendered:

- 1) The proposed spectral graph-theoretic approach outperforms all the other approaches tested; this holds for all sensing scenarios (Table 2-7). An F-score in the range of 80-95% is possible with the proposed approach while it is at best 60% with the other approaches, i.e., little better than a random guess.
- 2) The prediction results from the photodetector signal are inferior for the spectral graph-theoretic approach compared to the same approach applied to other sensor signals. Nonetheless, the F-score results are within 20% of the highest resolution sensor (i.e., the thermal camera). The confusion matrix based on 250 randomly selected samples — a sample is a frame for the thermal and video images and 555  $\mu$ s of data for the photodetector — is shown in
- 3) Table 2-8.
- 4) The detection fidelity is contingent on the analytical approach used. Even a sensor with the highest spatial resolution, such as a thermal camera, when integrated with an ill-suited analytical approach will lead to poor results. For instance, the thermal

camera when combined with a linear discriminant classifier, had a poor F-score (36%) compared to the visible camera (58%) and photodetector (59%).

Table 2-7: F-score results from applying the proposed approach.

to each of the three types of sensor signals. (a) The percentage F-score results for detecting the two process conditions in thermal camera, visible camera and photodetector. The numbers in parentheses represent the standard deviation from a five-fold replication (data from three layers). Acronyms are as follows: LD: Linear Discriminant, KNN: K-Nearest Neighbors, Tree: Decision Tree, SVM: Support Vector Machines, BT: Boosted Trees, NN: Neural Network, QDA: Quadratic Discriminant Analysis.

Sensor	Data Dimension	Proposed Approach	LD	KNN	Tree	SVM	Boosted Trees	NN	QDA
Thermal Camera	2D (128×360)	0.95 (0.01)	0.36 (0.02)	0.5 (0.02)	0.38 (0.03)	0.42 (0.03)	0.43 (0.03)	0.40 (0.02)	0.6 (0.02)
Visible Camera	2D (256×256)	0.83 (0.02)	0.58 (0.02)	0.57 (0.03)	0.61 (0.01)	0.63 (0.02)	0.62 (0.01)	0.54 (0.00)	0.5 (0.01)
Photodetector	1D (555 × 1)	0.79 (0.01)	0.59 (0.02)	0.6 (0.02)	0.62 (0.01)	0.61 (0.01)	0.61 (0.02)	0.6 (0.01)	0.5 (0.01)

Table 2-8: The confusion matrix for detecting the two conditions (overhang and bulk) from the thermal camera, high-speed camera, and photodetector.

The data is for 250 randomly chosen sequences from each build condition.

		Predicted Build Condition		
		Overhang	Bulk	
Actual Process Condition	Thermal Camera	Overhang	250	0
		Bulk	24	226
	Visible Camera	Overhang	250	0
		Bulk	83	167
	Photodetector	Overhang	157	93
		Bulk	9	241

## 2.6 Conclusions

This work proposed a spectral graph-theoretic approach for monitoring the build condition in the laser powder bed fusion (LPBF) additive manufacturing (AM) process via a sensing array consisting of a photodetector, SWIR thermal camera, and high-speed video camera. The central idea of the approach is to convert the sensor data into a lower dimensional manifold, specifically, a weighted and undirected network graph. Specific conclusions are as follows:

1. An LPBF part with a steep overhang feature ( $40.5^\circ$ ) was built without supports. The build was monitored continuously with the aforementioned sensor suite with the intent to detect the difference in signal patterns when the bulk and overhang sections were sintered. Extracting and detecting the difference in sensor signatures for such a simple case was the first-step towards *in-situ* defect detection in AM. The analysis was extended to more sophisticated machine learning approaches, such as neural networks and support vector machines, among others (Sec. 2.5). These approaches had a fidelity (F-score) for distinguishing between the overhang and bulk states in the vicinity of 40-60%.
2. The proposed graph-theoretic approach was applied to the sensor data with the intent to distinguish between the overhang and bulk build states, the F-score obtained was in the region of 80 to 95%, contingent on the type of sensors: F-score  $\sim$  95% for the shortwave infrared thermal camera, F-score  $\sim$  83% for the high-speed video camera, and F-score  $\sim$  79% for the photodetector sensor.

These results led to the following inferences:

- To monitor the LPBF process, in-process sensing must be integrated with new and advanced analytical approaches capable of combining data from multiple sensors. Existing approaches, such as neural networks are ineffective probably due to their inability to discern the subtle and short-lived indications of an incipient fault, and their limitations with accommodating heterogeneous sensors.
- A low fidelity sensor, such as a photodetector, although not as capable in discriminating between build conditions as a high-fidelity sensor, has detection capability still within 20% of the thermal camera. This limitation may be overcome by using multiple photodetector sensors together.

### **Acknowledgements**

The experimental data for this work came from Dr. Brandon Lane and Dr. Jarred Heigel of the Intelligent Systems Division, National Institute of Standards and Technology (NIST), Gaithersburg, MD.

## Appendix

Classification Method	Input type	Setting
Laplacian eigenvector Basis	Thermal camera	No. of eigenvectors: 10 Laplacian matrix: weighted symmetric Kernel Function: MD distance
	Visible camera	No. of eigenvectors: 1 Laplacian matrix: weighted symmetric Kernel Function: MD distance
	Photodetector	No. of eigenvectors: 5 Laplacian matrix: weighted random walk (orthogonalized using Gram Schmidt ) Kernel Function: MD distance
Linear Discriminant (LD)	An array of eight Statistical Features for each dimension/ column:  Mean, Standard Deviation  Range, Skewness,  Kurtosis, Interquartile range,  Min, Max	Linear boundaries between classes
K-Nearest Neighbors (KNN)		numbers of neighbors: 1
Decision Tree		maximum number of splits: 100
Support Vector Machines (SVM)		Gaussian scale: $\sqrt{\text{number of predictors} / 4}$
Boosted Trees (BT)		an ensemble of decision trees (maximum number of splits set to 20) using the AdaBoost algorithm
Neural Network (NN)		number of hidden neurons: 2
Quadratic Discriminant Analysis (QDA)		Elliptical, parabolic, and hyperbolic boundaries between classes

### 3 Detecting Material Contamination in LPBF

#### 3.1 Goal, Objective, and Hypothesis

As a first step to realize the long-term aim of qualify-as-you-build in AM, the goal of this work is to detect the onset of material contamination-related anomalies in LPBF. In pursuit of this goal, the objective is to develop and apply a spectral graph-theoretic approach for real-time detection of material cross-contamination using process signatures acquired by a photodetector sensor.

The central hypothesis is that tracking the signatures acquired from the photodetector in the spectral graph domain leads to early and more accurate detection of material cross-contamination in LPBF, compared to the traditional Box-Jenkins stochastic delay-embedded time series analysis of the signal, such as autoregressive (AR) and autoregressive moving average (ARMA) modeling. This work addresses the following open research question in the context of material cross-contamination in the LPBF process—what process signatures can capture the onset of contamination?

To put the challenge of cross-contamination in pictorial context, Figure 3-1 shows optical images of an etched Inconel 625 AM sample from this work contaminated with varying severities of tungsten and aluminum trace material. These images demonstrate that material cross-contamination changes the basic microstructure of the build and has the proclivity to spread beyond the layer in which they occur.

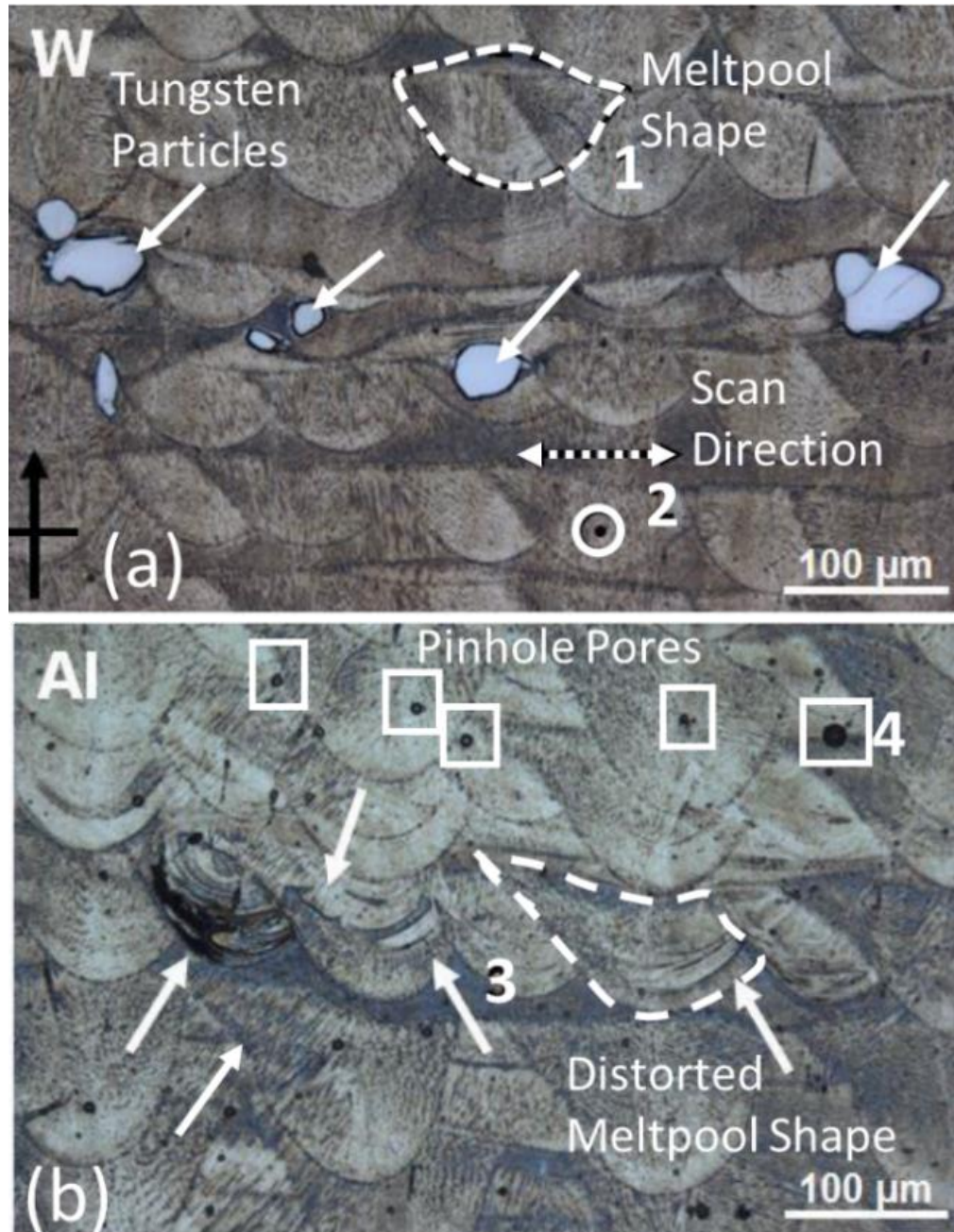


Figure 3-1: Optical image of an etched and polished Inconel 625 specimen showing the effect of contamination.

The black arrow indicates the build direction. (a) Contamination with tungsten, which due to its high melting point does not fuse and tends to cascade through several layers. The dashed-line (1) indicates the shape of a melt pool, penetrating the previously deposited layer. Also, the overlaps between tracks could be recognized. The dashed line and circle (2) shown at the bottom of the tungsten specimen are representative of the hatching directions in the two consecutive layers. (b) The contamination with aluminum is not readily evident as trace particles, but a closer examination of the hatch pattern reveals that aluminum tends to distort the melt pool as indicated by the arrows (3), and (4) vaporization of the aluminum particles causes uniform circular pinhole (gas-induced) porosity of diameter  $\sim 10 \mu\text{m}$ .

In Figure 3-1 (a), contamination with tungsten manifests as unfused particles evident as light-hued inclusions in the darker Inconel 625 matrix. This is probably because: (1) the melting point of tungsten is much higher ( $\sim 3422$  °C) than Inconel 625 ( $\sim 1300$  °C), and (2) tungsten is not an alloying element in Inconel 625. Given these two reasons, tungsten does not dissolve into the Inconel 625 matrix. The contamination of Inconel with tungsten is a critical problem that may lead to premature failure of AM parts. For instance, in a recent publication, Brandão *et al.* hypothesized that given the hardness of tungsten, un-melted tungsten particles tend to become preferred sites for crack initiation under tensile loading[117].

In Figure 3-1 (b), contamination with aluminum does not manifest in clearly distinguishable particle traces; however, it tends to distort the melt pool. This is because of two reasons: (1) Unlike tungsten, aluminum has a much lower melting point ( $\sim 660$  °C) than the melting point of Inconel 625 ( $\sim 1300$  °C). Further, aluminum is also an allowable alloying element in Inconel 625 (maximum 0.4% by mass). Hence, aluminum particles may dissolve into the Inconel 625 matrix. (2) Aluminum particles may vaporize given the higher energy applied to melt Inconel 625. This vaporization of aluminum particles leads to uniform circular pores of diameter  $\sim 10$   $\mu\text{m}$ , which is termed as gas porosity or pinhole porosity in the literature [29].

During the process, two types of foreign contaminant materials, namely, tungsten and aluminum powders under varying degrees of severity were introduced. Offline X-ray Computed Tomography (XCT) and metallurgical analyses of parts indicate that contingent on its severity, contaminant particles may cascade to over eight subsequent layers of the

build and enter up to three previously deposited layers. In this context, this research took the first step towards detecting cross-contamination in AM by tracking the process signatures from the photodetector sensor, hatch-by-hatch, invoking spectral graph transform coefficients. These coefficients were subsequently traced on a Hotelling  $T^2$  statistical control chart to determine the location of contaminants [118].

The rest of this study is organized as follows. The literature in the area of sensing and monitoring in AM is discussed in Sec. 3.2, followed by a description of the experimental methodology to initiate controlled material cross-contamination in Sec. 3.3. The spectral graph-theoretic approach is explained in Sec. 3.4, and subsequently applied to the LPBF process signals in Sec. 3.5, followed by a summary of the conclusions and avenues for future research in Sec. 3.6.

### 3.2 Prior Work and Challenges in Material Contamination in LPBF

Brandão *et al.* reported the effect of high-density tungsten inclusions on the tensile strength and microstructure of LPBF test parts. Although contaminants were not found to influence the mean tensile strength of the specimen, the fracture cracks during testing were found to initiate at the locations where contaminants were present. Furthermore, specimens with cross-contamination tended to have large variability in the tensile strength readings compared to those without contamination.

In the related context of purity and physical characteristics (diameter and shape) of the powder, studies have been conducted to understand the effect of powder reuse on part functional attributes in electron beam PBF (EB-PBF) [119]. This is because, unlike LPBF, in EB-PBF the powder is maintained at a higher temperature [120]. Hence, there is a

practical concern that repeated reuse of the powder in EB-PBF may lead to deviation in powder characteristics and hence the functional performance of the part. These studies have concluded that although the repeated reuse of the powder increases its oxygen content and changes its particle geometry, the impact of powder reuse on mechanical strength was statistically insignificant [119, 120].

The effect of feedstock characteristics on the mechanical properties of LPBF parts was investigated by Ardila *et al.* who found that the effect of reuse of Inconel 718 powder had statistically insignificant effect on material strength, nor did the shape of the powder particles deviate significantly over 14 iterations [121]. Recent studies by Clemon at the University of California, Berkeley attempted to characterize the effect of powder properties on the process performance [122]. Thus, the understanding of the effect of material cross-contamination on part microstructure in LPBF remains to be thoroughly investigated.

The second challenge that this work must tackle lies in the domain of data analytics and modeling in AM. The in-process sensor data in AM processes are heterogeneous (several different sensors are used), acquired at high velocity (the sampling rate of sensors is high), and high in volume (several gigabytes of data are acquired for a build). There is an active and ongoing effort to develop data analytics and modeling approaches to track and monitor these sensor data in real time, and relate the sensor signatures to functional properties [73, 74]. The need for approaches to synthesize the data gathered in AM processes has been explicitly designated as a research priority area in recent roadmap reports [9, 12].

Comprehensive review articles for in-process sensing are available in Ref.[82, 85, 123]. Nassar and Reutzel, *et al.* at Pennsylvania State University experimented with imaging of the LPBF powder bed under various illumination conditions [124]. Defects, such as large voids caused by improper raking of the powder across the bed were identified from these images[125]. They have also used a multispectral photodetector setup that concentrates on observing the line-to-continuum ratio of the laser plume in both the LPBF and DED processes to detect the onset of defects, such as porosity [126, 127]. Lane *et al.* at NIST integrated an LPBF machine (EOS M270) with thermal and high-speed cameras, and a photodetector [101]. Researchers at NIST are currently building customized LPBF testbeds instrumented with multiple sensors, based on findings at Edison Welding Institute (EWI) [65, 101]. A large body of work in sensing and monitoring in LPBF was reported by the Kruth group [80, 81, 87, 128] and Witt group [66, 67, 129, 130] in Europe. The sensing and monitoring approaches for PBF used in these pioneering works are categorized into the following two broad areas:

- Melt pool monitoring: Optical cameras, high-speed cameras, Infrared (IR) cameras, photodetectors, and pyrometers are used to gauge thermal, intensity, and morphological aspects of the melt pool. The visual systems and sensors are either embedded coaxially with the laser; or a system that is either external or internal to the chamber is inclined at an angle to the build platen [73, 74]. The challenge is that the temperature profiles captured by IR systems are a trend and not the actual temperature. This is because the material emissivity has to be factored into the readings, and furthermore, if the sensor is mounted at an angle to the powder bed, the incident thermal radiation is, therefore, not perpendicular to the sensing

elements in the IR camera, which in turn affects the accuracy of the temperature reading.

- Powder bed monitoring: Acoustic (ultrasonic) sensors, vibration (accelerometers), optical cameras, and IR thermal cameras have also been proposed to monitor the powder bed conditions. For instance, Rieder *et al.* built a system with ultrasonic sensors mounted underneath the build platen to detect voids in the build [131]. Vibration sensors were used by Craeghs *et al.* to identify faulty deposition of powder layers resulting from a damaged recoater [81]. Instances of super elevations, poor surface finish, and defective features have been detected using both visual and vibration sensors. In a similar vein, Nassar *et al.* used optical images taken layer-by-layer to detect improper raking of the material and distortion during the process [68].

The work reported by Craeghs *et al.* in Ref. [81] serves as an archetypical example of both melt pool and powder bed monitoring. Craeghs *et al.* [81] incorporated three sensors, namely, a visual camera to ascertain the characteristics of the powder raked by the blade across the build platen (i.e., a powder bed monitoring system); and a photodiode (photodetector) and a camera coaxially aligned with the laser, both of which were used to monitor the melt pool. In the context of monitoring the powder bed raked across the platen, Craeghs *et al.* made two observations. First, the gradual wear of the recoater blade caused streaks to appear across the deposited powder bed. In a similar vein, Abdelrahman *et al.* showed that non-uniform raking of the powder bed may lead to defects[125]. The effect of using a damaged recoater blade leads to discernable streaks on the powder bed surface, which in turn manifests in poor part surface finish. The uneven deposition of the material

resulting from a damaged recoater blade was detected by Craeghs *et al.* using a statistical control chart-type strategy. The grayscale values of the powder bed taken by the visual camera were tracked and used as a feature to discriminate the onset of defects due to improper raking of the powder across the bed. For instance, the grayscale image values for a layer deposited with a damaged blade showed clear spikes compared to when the powder was raked uniformly.

Furthermore, the melt pool was monitored with the photodiode and optical camera system. The optical systems were augmented with filters to constrain the wavelength of acquired light in the region of 780 nm to 950 nm. The sampling rate of the photodiode was 10 kHz, which translates to a sample every 100  $\mu\text{m}$  of the linear distance traversed by the laser, considering that the laser scan velocity was set at 1000 mm/sec. Incidentally, the laser scan velocity and sampling rate of the photodiode used by Craeghs *et al.* [81] were nearly identical to those in this work (see Sec. 3.3). Further, using image segmentation and pixel intensity estimation techniques from the area of image processing, the authors tracked the melt pool area and the length to width ratio of the melt pool. These melt pool image features were the monitoring statistics which could be used in a statistical control chart; they have also shown to be indicative of process phenomena such as *balling* by other researchers [94, 95].

Another example was tendered by Craeghs *et al.* [81] for detecting porosity in LPBF due to process drifts. In this case, abrupt machine errors led to an increase in the part porosity. At certain instances, due to faults in the build platform stage motor, the powder bed was lowered farther than the set layer height. Hence, a powder thickness equivalent to multiple layers was accidentally raked across the bed. This unusually high layer of

thickness led to an increase in porosity, because, the energy applied per unit volume (volumetric energy density) was insufficient to melt the powder. The authors reported that the photodiode signal depicted an inordinate increase in mean and standard deviation corresponding to layers with faulty deposition.

A lacuna of the analysis used in these prior works in sensing and modeling in AM, and as exemplified in the pioneering work of Craeghs *et al.* [81], is that they are largely offline and use approaches such as Fourier transforms or statistical-feature models, which, as it's demonstrated in Sec. 3.5, are not amenable to online monitoring. To take these pioneering works of in-process monitoring in AM forward, it is necessary to develop approaches capable of detecting a wider variety of defects in real time and with greater accuracy. Recent works by Yang *et al.* [69] have attempted to overcome these challenges by resorting to advanced analytics, such as fractal signal analysis, and adaptive clustering and Bayesian modeling.

A drawback with these newer data analytics approaches is that they require well-defined model structures, e.g., a logistic fractal model, tuning of parameters, setting the number of layers and nodes in neural networks, and tuning the number of terms in traditional time series analysis techniques, such as ARMA. Furthermore, the classical time series approaches assume that the statistical moments of the signal do not change over time (stationarity assumption). These assumptions are not tenable in LPBF, wherein the signal may not confirm with well-known distributions, or may change from layer-to-layer and from one part design to the next. The spectral graph-theoretic approach proposed herein has two advantages over existing approaches:

- (1) The approach is feature-free, in that it does not rely on extracting statistical features, such as mean or the frequency power spectrum to detect changes in the process; and
- (2) Spectral graph theory is model-free, i.e., it does not need an *a priori* defined model structure, such as number of time delay parameters as in stochastic time series modeling.

### 3.3 Experimental Setup and Data Acquisition

This section is divided into two parts. Sec. 3.3.1 describes the experimental setup and the procedure used to initiate contamination of different types and severity levels, and Sec. 3.3.2, which describes the sensor instrumentation and data acquisition methodology.

#### 3.3.1 Experimental Procedure

In this research, a customized, Open Architecture LPBF Platform was designed and implemented at Edison Welding Institute (EWI) [65]. This platform, shown in Figure 3-3 (a and b) allowed complete control of the key process factors, such as laser power, scan speed, and scan pattern; commercial LPBF systems typically do not allow users to customize the process settings. The energy source was a ytterbium fiber laser with wavelength of 1070 nm operating in continuous mode (manufacturer IPG). Furthermore, an array of heterogeneous sensors was integrated within the apparatus and was located on an optical table near the laser scanning mechanism.

Further details of this setup are available in previous work by Boulware *et al.* [65]. An Inconel 625 cuboid-shaped test part of size 10 mm × 10 mm × 15.20 mm (vertical build height) was made with the following parameters after extensive offline studies: scan velocity (V) 960 mm/s, laser power (P) 270 W, layer thickness (T) 0.040 mm, and hatch

spacing (H) 0.1 mm, i.e., an applied volumetric energy density  $E_v \approx 70 \text{ J/mm}^3 = P/(H \times V \times T)$ .

All powders used in this work were sourced from Electro Optical Systems GmbH (EOS) and were commercially marketed as NickelAlloy IN625; in the material data sheet supplied by the company this material was stated as corresponding to UNS N06625[54]. It is noted that the layer thickness of 0.040 mm was an input value to the system. It was controlled by accuracy of the motion stages on the build platform and the dispenser platform (typically 0.001 mm resolution). It was not an average of multiple layers or measured directly, but rather an input to the system and validated during preventive maintenance and calibration routines performed semi-annually. To precisely control the degree of material contamination, a material dispensing setup was fabricated. The setup attached to the recoater arm, and powder material (contaminant) was dispensed from a motorized hopper. Figure 3-3 shows the schematic illustration of the sensor test bed and the equipment used for dispersion of the contaminants (tungsten and aluminum particles).

The experimental procedure for dispersing contaminants, namely aluminum (Al) and tungsten (W), is depicted in Figure 3-2. The contaminants were dispersed over the powder bed every 20<sup>th</sup> layer. This procedure for purposely introducing contamination was repeated three times over a total build consisting of 380 layers. The severity of contamination was controlled at three levels for each type of contaminant material, viz., aluminum and tungsten. Further, the contaminant particles were distributed over the powder bed in two ways, called dynamic contamination and static contamination. In the so-called static contamination, which occurred in levels labeled L<sub>1</sub>, L<sub>2</sub>, and L<sub>3</sub> (in ascending order of contaminant volume), the contaminant particles were dispensed entirely in one area of the

layer and then raked across the bed. In the dynamic contamination mode, which occurred in layers labeled L<sub>4</sub>, L<sub>5</sub> and L<sub>6</sub>, the contaminant particles were dispensed continuously as the recoater moved across the bed.

When the rotary dispenser shaft in Figure 3-3(c) was started it opened the hopper and the contaminant material was dispensed through a small notch from the hopper side to an open column. The contaminant particles were then deposited on the powder bed via a nozzle. There was a 0.5-mm gap between the nozzle that deposited the contaminants and the powder bed surface. The degree of contamination for every layer was controlled by varying the number of rotations of the dispenser shaft mechanism below the hopper. A relationship between the number of shaft rotations and the volume of material deposited was described in a patent application granted to EWI [64].

In the static contamination mode, the recoater was stopped while it was raking the Inconel 625 powder and the shaft was rotated. This dropped the contaminant onto one spot on the powder bed. The recoater then began to move and spread the contaminants on the powder bed. In the dynamic contamination mode, the contaminant powder was dispensed synchronous with the recoater movement. That is, the hopper motor in the fixture shown in Figure 3-1(c) was continually operational as the recoater raked the Inconel 625 powder across the bed.

This sort of deposition of the contaminant resulted in an elongated line or streak across the powder bed, and was labeled L<sub>4</sub>, L<sub>5</sub> and L<sub>6</sub> in ascending order of severity (Figure 3-4). The consequence of the different types of contamination modes (i.e., static and dynamic mode) was captured using an in-process optical camera in Figure 3-4 (a1) and (a2); the

severity of the contamination levels and their sequence within each replicate of experiment are further detailed in Figure 3-4 (b1) and (b2), and Table 3-1.

The quantifier used for assessing severity of contamination (Figure 3-4) was the volume contamination per unit area of the base material (Inconel 625), i.e.,  $\text{mm}^3/\text{mm}^2$ . This measure accounted for the distribution profile of contaminant powder in each contamination level. As a result, length, width, and compactness of contaminant powder were considered in the design of the six levels of contamination ( $L_1, L_2$  and  $L_3$  for static contamination; and  $L_4, L_5$  and  $L_6$  for dynamic contamination).

There was the possibility of the contaminant powder accidentally leaking from the hopper if there were gaps in the mechanism assembly. If leakage were to occur it would lead to erroneous traceability – i.e., the in-process photodetector sensor signatures would (correctly) show a spike, while the layer would be (incorrectly) recorded by the operator as not being contaminated. To ensure that powder leakage did not occur during the experimental tests, the whole test bed including dispenser, build plate, and collector was sealed, and the hopper system was tested for 100 times. During these test runs, no leakage of powder was detected from the powder container on the build platform and collector.

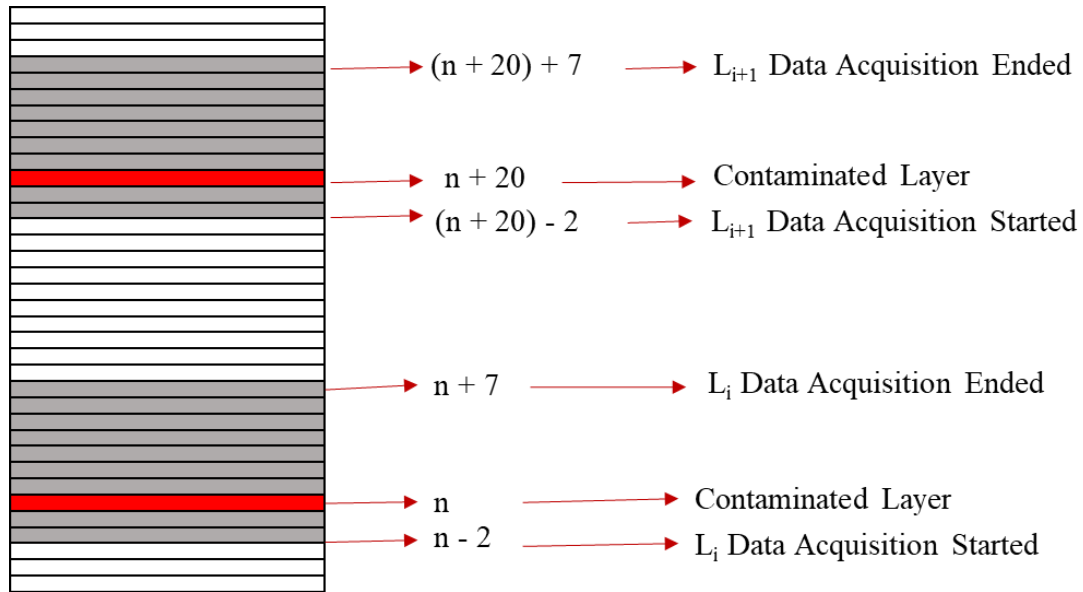


Figure 3-2: The schema used for introducing contamination during the build. The gray layers show the ones where data is captured. The red layers indicate where the contamination is introduced.

Table 3-1. The build layout and contamination pattern. The contamination set of  $L_1$  through  $L_6$  was deposited three times, and at the end of 3 iterations was followed by 20 cover layers.

Contamination Set #	Base Line (BL) / Contamination Layer ( $L_n$ , $n=1$ to 6)	Start Layer	End Layer	End Height (mm)
Iteration 1	Base line (non-contaminated layer)	1	19	0.76
	(Static contamination) $L_1$ -1	20	20	0.80
	Base line (non-contaminated layer)	21	39	1.56
	(Static contamination) $L_2$ -1	40	40	1.60
	Base line (non-contaminated layer)	41	59	2.36
	(Static contamination) $L_3$ -1	60	60	2.40
	Base line (non-contaminated layer)	61	79	3.16
	(Dynamic contamination) $L_4$ -1	80	80	3.20
	Base line (non-contaminated layer)	81	99	3.96
	(Dynamic contamination) $L_5$ -1	100	100	4.00
	Base line (non-contaminated layer)	101	119	4.76
	(Dynamic contamination) $L_6$ -1	120	120	4.80
× 2 iterations of the build pattern	BL- $L_1$ -2 through $L_6$ -2 BL- $L_1$ -3 through $L_6$ -3	121	360	14.44
Cover Layers	Base line (non-contaminated layer)	361	380	15.20

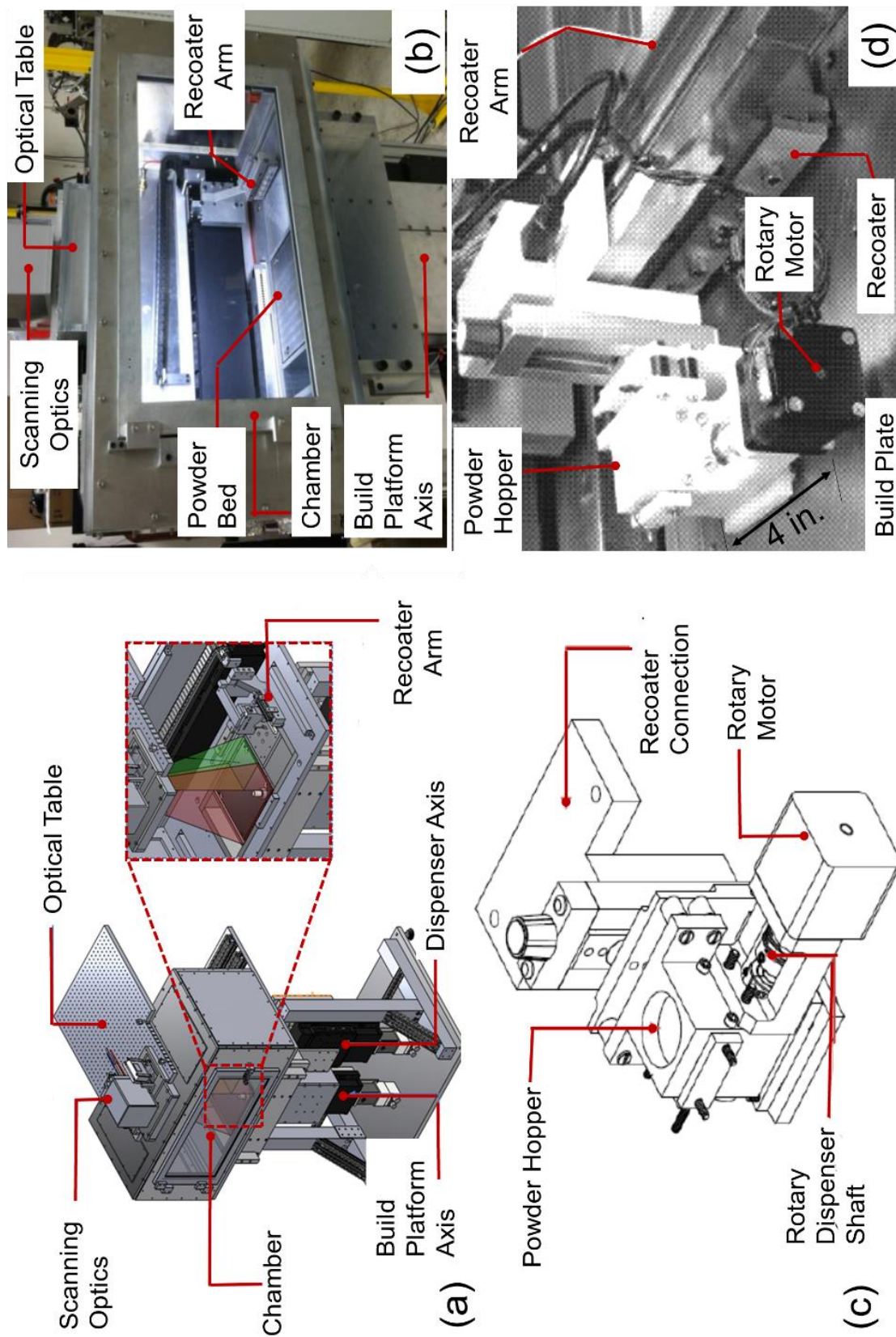


Figure 3-3: A schematic of the open architecture LPBF platform at EWI. For scale purposes, the powder bed on the machine accommodates parts as large as 10 inch  $\times$  10 inch (250 mm  $\times$  250 mm). (b) Photograph of the LPBF platform (c) Schematic of the fixture made to deliver

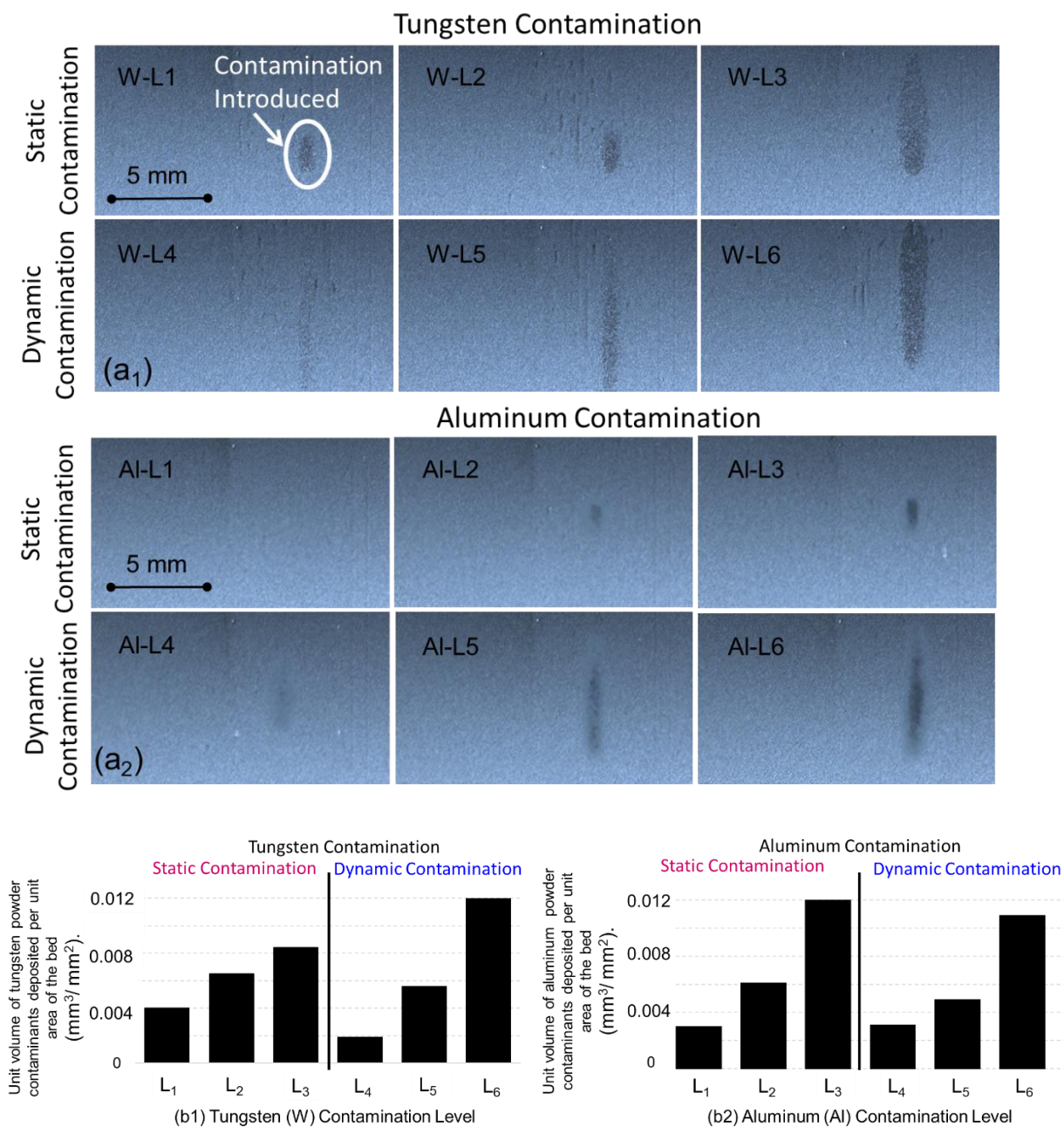


Figure 3-4: Post recoating optical images after tungsten contamination under different conditions. (a1) Tungsten contamination and (a2) Aluminum contamination. The unit volumes of deposited powders for each of six contamination levels in (b1) tungsten and (b2) aluminum.

### 3.3.2 Sensor Integration and In-Process Data Acquisition

Photodetector signal data were acquired for a total of 10 layers as follows: (1) two layers prior to contamination, (2) the contaminated layer, and (3) seven layers subsequent to the contamination. The photodetector sensor was used in this study to detect occurrence of contamination. Especially, a Thorlabs model PDA36A photodetector was used and was located coaxial and synchronized with the switching of the laser (i.e., data was acquired only when the laser was active).

The analog photodetector signal was acquired via the National Instruments NI 9215 analog input module. The detection range of the photodetector was the 350 nm to 1100 nm range with the gain of 40 dB, and the sampling rate was set at 10 kHz. The photodetector module was a Silicon junction photodiode (also called a photoelectric pyrometer or photodiode) coupled with an amplifier, which proportionally translates radiated light intensity into an electrical signal. The transducing mechanism at play with this type of photodiode was the generation of a photocurrent upon light absorption in the depleted region of the semi-conduction detecting element (silicon). The optical delivery to the photodetector aperture was integrated coaxially into the optical path of the laser, such that the light being interrogated stemmed from the laser plume during the melting process. In other words, the photodetector measured the radiation intensity of the laser plume (which in turn was proportional to the temperature of the melt pool) in terms of an amplified electrical signal with output in volts.

The sensor operated in a fast, highly linear manner, producing a current output proportional to the light intensity absorbed by the sensor. The data was acquired hatch-by-

hatch; the laser traced the hatch pattern's alternating manner as shown in Figure 3-5 – parallel (to the recoater direction) for odd layers, and perpendicular for even layers. The hatch pattern information is used in Sec. 3.5.2 to relate the sensor signatures to the position at which the contamination occurred in XCT. In all, data was available for 180 of the total 380 layers of the build. Each layer was comprised of 100 hatches, and each hatch took ~ 0.01 sec. (10 milliseconds) to melt noting that the laser scan velocity was 960 mm/sec. Hence there were 100 photodetector data points acquired per hatch given that the sensor sampling rate was 10 kHz. In this build the laser stayed on for ~ 1 sec. per layer, for a total of under 7 minutes counting the time to melt the contour.

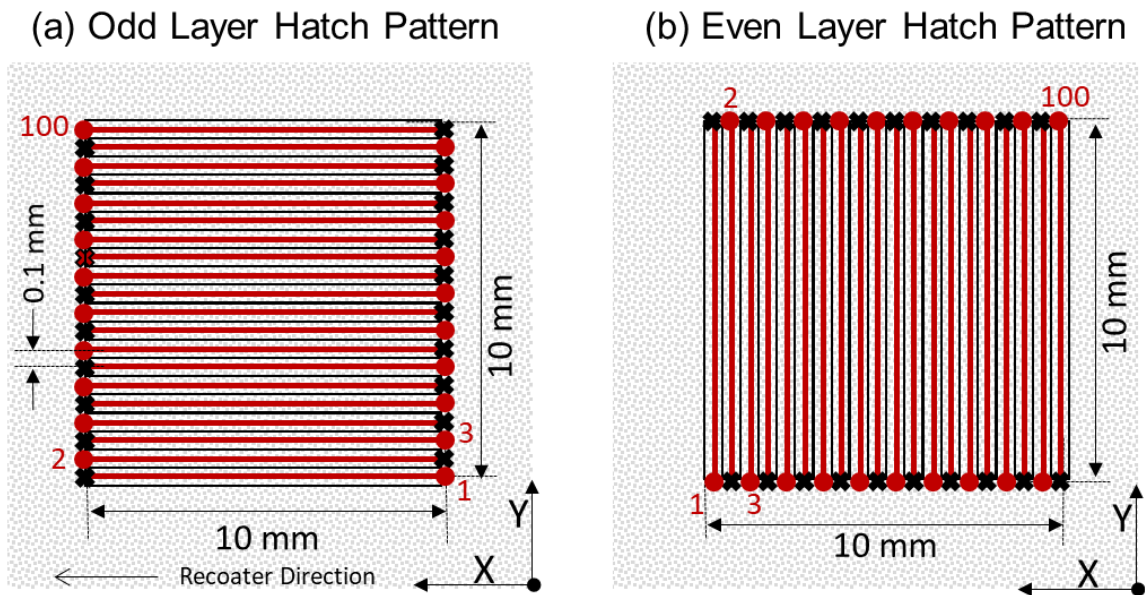


Figure 3-5: The horizontal and vertical hatch patterns implemented during the printing process. The symbols O and X demarcate the starting and ending points for a hatch. There are 100 hatches per layer, each hatch takes close to 10 milliseconds to melt (laser velocity 960 mm/sec), the entire layer takes ~ 1 sec. to fuse.

### 3.4 Proposed Methodology

The aim of this section is to detect the onset of material cross-contamination in the LPBF process using in-process data. To realize this aim, the key idea is to transform the raw data into a domain that makes it tractable to extract signatures in real time. In this work, the signal transformation procedure adopted was from the area of spectral graph theory and has been discussed in depth in our previous research [25, 132].

#### 3.4.1 Overview of the Approach

A similar form to the approach proposed in this work has been used previously by the authors in the context of surface finish characterization in the chemical-mechanical planarization (CMP) semiconductor manufacturing process, monitoring chatter in ultraprecision diamond turning, and recently for assessment of post-process geometric integrity in polymer additive manufacturing. The main difference of this work from those previous forays lies in the application of spectral graph eigenvectors for real-time classification of material cross-contamination in PBF. The previous works were mainly restricted for offline characterization and used spectral graph eigenvalues which were not amenable for real-time adaptive monitoring of a fast-changing processes such as PBF. The underlying mathematics described herewith bears close resemblance to our previous works in spectral graph theory but is nonetheless repeated here for the sake of cohesiveness and continuity [25, 132].

The procedure is summarized in Figure 3-6 and encapsulates four key steps. Steps 1 through 3 can be considered as the training phase, wherein a library of sensor signatures representing non-contaminated states was created. The last step, Step 4, classified a hatch photodetector signal for each hatch into one of the two states, namely, contaminated vs.

non-contaminated in real time within a control chart framework. The underlying concept for each step is summarized herewith. The mathematical convention is to denote matrices and vectors with bold typesets.

The approach has the following four steps, each of these steps is described in detail in Sec. 3.4.2.

Step 1: The photodetector signal  $\mathbf{x}_l^p$  representing each hatch  $p \in \{1 \dots h\}$  at layer  $l \in \{1 \dots L\}$  of the melting process is converted into a weighted and undirected network graph  $G \equiv (V, E, W)$ . Where  $V$ ,  $E$  and  $W$  are the graph vertices, edges, and weight between the edges, respectively.

Step 2: The topological information in the graph  $G \equiv (V, E, W)$  is extracted in terms of the eigenvectors ( $\mathbf{v}_{\mathbf{x}_1^p}$ ) and eigenvalues ( $\lambda_{\mathbf{x}_1^p}$ ) of the Laplacian matrix ( $\mathcal{L}_{\mathbf{x}_1^p}$ ). In other words, a spectral graph transform  $G(\cdot)$  on the signal  $\mathbf{x}_1^p$  is defined, i.e.,  $G(\mathbf{x}_1^p) \rightarrow \mathcal{L}_{\mathbf{x}_1^p}(\lambda_{\mathbf{x}_1^p}, \mathbf{v}_{\mathbf{x}_1^p})$ .

Step 3: A learning procedure is used to obtain a universal eigenvector basis  $\mathbf{V}_{normal}$  corresponding to the normal or non-contaminated process state. Through this universal basis a spectral graph Fourier transform  $\hat{G}(\mathbf{x}_l^p) = [(\mathbf{x}_l^p)^T (\mathbf{V}_{normal})]$  is defined for non-contaminated layers. Such a graph-based Fourier transform facilitates creating a library of spectral graph coefficients  $\mathbf{C}$  archetypical of the non-contaminated process state.

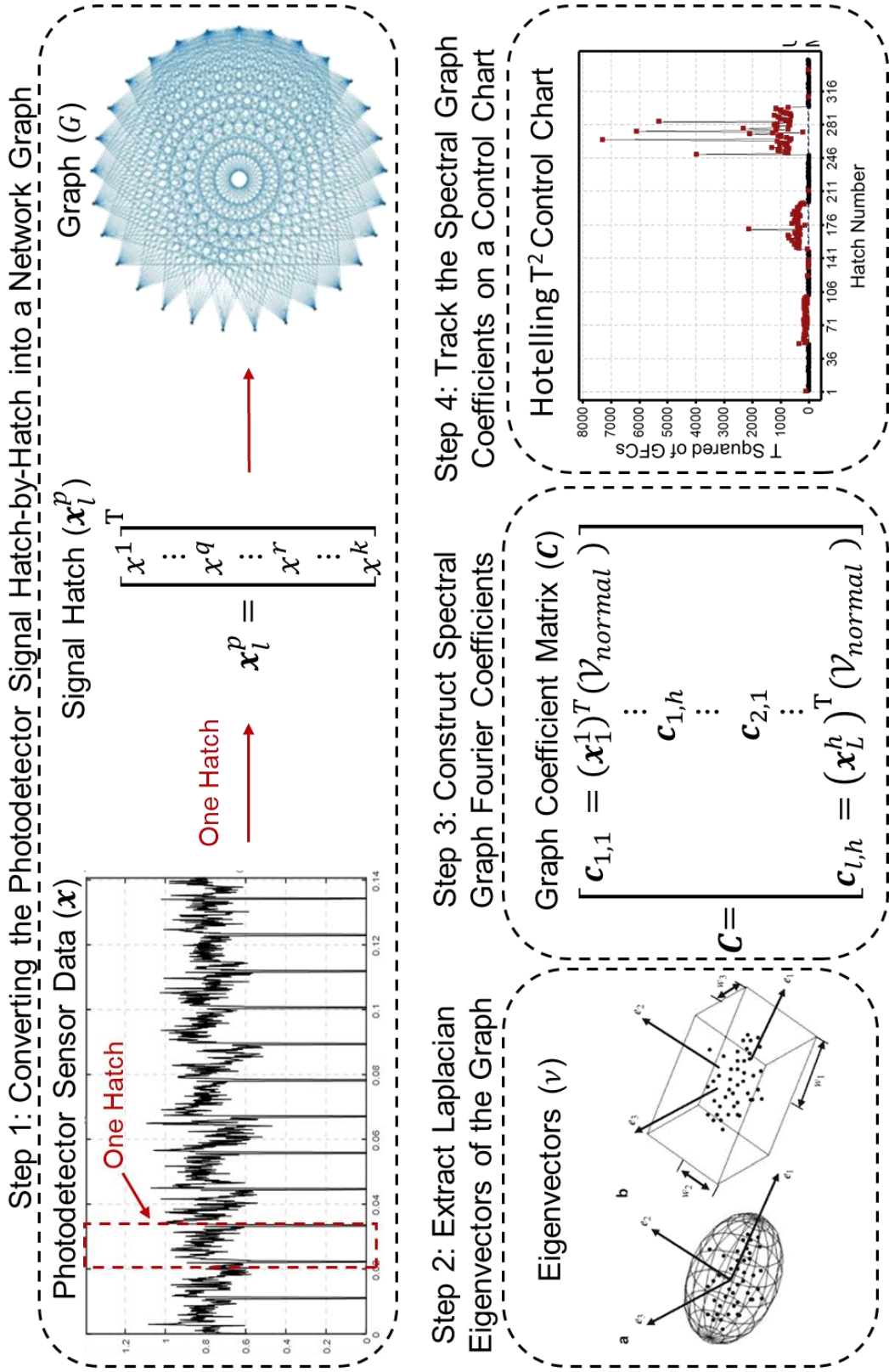


Figure 3-6: Graphical overview of the proposed spectral graph-theoretic approach.

*Step 4:* The coefficients  $\mathbf{C}$ , representative of the normal or non-contaminated process state, are used to build a multivariate statistical control chart, called the Hotelling  $T^2$  control chart. Given a new signal  $\mathbf{y}$ , an inner product with the basis vector  $\mathbf{v}_{normal}$ ,  $\hat{G}(\mathbf{y}) = [(\mathbf{y})^T(\mathbf{v}_{normal})]$  leads to a set of new spectral graph Fourier coefficients  $\hat{G}(\mathbf{y})$  that are easily traced on the control chart. If  $\hat{G}(\mathbf{y})$  falls outside the control limits established based on the data from the non-contaminated layers, then it is deemed as belonging to an out-of-control state, i.e., the data indicates that the layer is contaminated with trace materials.

### 3.4.2 Applying Spectral Graph Theory to the LPBF Photodetector data

*Step 1: Converting the photodetector signal hatch-by-hatch into a network graph.*

In this step, the aim is to represent each hatch related to the photodetector sensor data  $\mathbf{x}$  as a weighted, undirected network  $G(V, E, W)$ . This graph  $G(V, E, W)$  is a lower dimensional representation of the signal  $\mathbf{x}$ . Consider an  $m$ -data point long 1-dimensional signal  $\mathbf{x}$  for a layer  $l \in \{1 \dots L\}$  per the matrix shown in Eq. (2-1).

$$\bullet \quad \mathbf{x}_l = [x^1 \quad \dots \quad x^i \quad \dots \quad x^m]^T, l \in \{1 \dots L = 180\}. \quad (3-1)$$

In this work  $L = 180$  (data from ten layers for each of the six levels of contamination replicated thrice,  $10 \times 6 \times 3$ ). Each layer was comprised of  $h$  hatches; in this work  $h = 100$ ,  $m = 10,000$ . Thus, the signal  $\mathbf{x}_l$  was further divisible into the corresponding  $h$  hatches; each hatch had  $k$  data points, with  $k = 100$ . This information was obtained by tracking the on-off switching time of the laser in each layer (i.e., the time between when the laser went on and off related to one hatch). Let each hatch in a layer be defined as a matrix  $\mathbf{x}_l^p$  so that it can be written in matrix form as,

$$\mathbf{x}_l^p = [x_l^1 \quad \dots \quad x_l^q \quad \dots \quad x_l^r \quad \dots \quad x_l^k]^T, \quad (3-2)$$

$$k \in \{1 \dots k = 100\}, p \in \{1 \dots h = 100\}, l \in \{1 \dots L = 180\}.$$

To transform a signal of each hatch into a network graph, the following procedure was followed. First, the pairwise comparisons  $w_{qr}$  were computed using a kernel function  $\Omega$  [62] per Eq. (2-3), where  $x_l^{q,p}$  and  $x_l^{r,p}$  are two points of the photodetector signal for a specific hatch  $\mathbf{x}_l^p$

$$w_{qr}^{l,p} = \Omega(x_l^{q,p}, x_l^{r,p}) \quad \forall q, r \in (1 \dots k). \quad (3-3)$$

While different types of kernel functions  $\Omega$ , such as the radial basis or Mahalanobis can be defined to obtain the graph  $G$ , for simplicity, the standardized Euclidean kernel shown in Eq. (2-5) is used, where  $V$  is the variance of the one-dimensional signal  $\mathbf{x}_l^p$ .

$$w_{qr}^{l,p} = (x_l^{q,p} - x_l^{r,p})V^{-1}(x_l^{q,p} - x_l^{r,p}). \quad (3-4)$$

The symmetric *similarity matrix*  $\mathbf{S}^{k \times k} = [w_{qr}^{l,p}]$  represents a weighted and undirected network graph  $G$ ; each row and column of  $\mathbf{S}$  is the vertex  $V$  (or node) of the graph, the relationship between the two vertices is captured in terms of its connection status  $E$  and weight  $W$ . The graph is then represented as  $G \equiv (V, E, W)$  [133]. To be more specific, the following notational additions to the similarity matrix  $\mathbf{S}$  and graph  $G$ :  $\mathbf{S}_{x_l^p}$ ;  $G_{x_l^p}$  are made, where  $\mathbf{x}_l^p$  relates to a specific hatch  $p$  for the signal related to the layer  $l$ .

*Notes for practical application:* In practice, it is found that the number of data points  $k$  in each hatch  $h$  may not be exactly 100 but may vary about 10%. As explained earlier,

immediately following Eq. (2-1), a hatch is readily demarcated in the data based on the laser activation time - when the laser goes off, the photodetector signal immediately degrades to zero as illustrated in Figure 3-11, Sec. 3.5.2. This method of demarcating a hatch was readily applicable in this work given the simple cuboid geometry of the test part (10 mm × 10 mm × 15.2 mm) – the hatch length, as shown in Figure 3-5, was constant across a layer. Such a regular and constant hatch length rarely occurs in practice.

Nevertheless, the approach can be readily modified even if a layer does not have a uniform hatch length. In the case of a complex geometry, a way to form the matrix  $\mathbf{x}_l^p$  is by tracking the data over a fixed timeframe instead of a complete hatch. Moreover, the part geometry does not intrinsically affect the approach because a pairwise comparison between data points is taken in Eq. (2-5) to track the change in the process.

*Step 2: Extracting topological information for the graph surface*

This phase aims to extract topological information from the graph  $G$ . Once the data  $\mathbf{x}_l^p$  in a particular hatch was represented as a graph  $G_{x_l^p}$ , the Laplacian eigenvectors  $\mathbf{v}_{x_l^p}$  were computed. This topological information was subsequently used to capture the process drifts from the nominal condition. From  $\mathbf{S}_{x_l^p}$ , the *degree*  $d_q^{l,p}$  of a node  $q$ ,  $q = \{1 \dots k\}$  was computed, which is a count of the number of edges that are incident upon the node. The node degree is the sum of each row in the similarity matrix  $\mathbf{S}$ . Subsequently, the diagonal *degree matrix*  $\mathbf{D}^{k \times k}$  was structured from  $d_q^{l,p}$  as follows,

$$d_q^{l,p} = \sum_{r=1}^k w_{qr}^{l,p} \quad \forall q = \{1 \dots k\}, \quad (3-5)$$

$$\mathcal{D}^{k \times k} \stackrel{\text{def}}{=} \begin{bmatrix} d_1^{l,p} & \cdots 0 \cdots & 0 \\ \vdots & \ddots & \vdots \\ 0 & \cdots 0 \cdots & d_k^{l,p} \end{bmatrix}. \quad (3-6)$$

This led to the normalized Laplacian  $\mathcal{L}$  of the graph  $G$ , for each hatch, which is defined as,

$$\mathcal{L} \stackrel{\text{def}}{=} \mathcal{D}^{-\frac{1}{2}} \times (\mathcal{D} - \mathcal{S}) \times \mathcal{D}^{-\frac{1}{2}},$$

$$\text{where, } \mathcal{D}^{-\frac{1}{2}} = \begin{bmatrix} 1/\sqrt{d_1^{l,p}} & \cdots 0 \cdots & 0 \\ \vdots & \ddots & \vdots \\ 0 & \cdots 0 \cdots & 1/\sqrt{d_k^{l,p}} \end{bmatrix}. \quad (3-7)$$

Thereafter, the eigenspectrum of  $\mathcal{L}$  was computed as,

$$\mathcal{L}\mathbf{v} = \lambda\mathbf{v}. \quad (3-8)$$

At the end of step 2, a spectral graph transform on a signal  $\mathbf{x}_i^p$  is defined,

$$G(\mathbf{x}_i^p) \rightarrow \mathcal{L}_{\mathbf{x}_i^p}(\lambda_{\mathbf{x}_i^p}, \mathbf{v}_{\mathbf{x}_i^p}). \quad (3-9)$$

In other words, the signal  $\mathbf{x}_i^p$  have been transformed for a specific hatch in terms of the eigenvectors ( $\mathbf{v}$ ) and eigenvalues ( $\lambda_{\mathbf{x}_i^p}$ ) of its Laplacian matrix ( $\mathcal{L}_{\mathbf{x}_i^p}$ ).

### *Step 3: Building the signal basis and spectral transformation*

This step aims to obtain the eigenvectors of  $\mathcal{L}_{\mathbf{x}_1^p}$  across all non-contaminated hatches and converge them towards a universal eigenvector basis. In other words, It is required to represent the signal during the non-contaminated state in terms of a single or universal eigenvector represented as  $\mathbf{v}_{normal}$ .

Step 3.1: A single universal basis  $\mathbf{V}_{normal}$  was obtained by applying a simple update schema. As the eigenvectors  $\mathbf{v}_{x_l^p}$ , for each hatch was calculated, the basis is updated as follows,

$$\mathbf{v}_{x_l^{p+1}} = \mathbf{v}_{x_l^p} + \Delta \left( \mathbf{v}_{x_l^{p+1}} - \mathbf{v}_{x_l^p} \right), \quad p \in \{1 \dots h\}, l \in \{1 \dots L\}, \quad (3-10)$$

$$\mathbf{V}_{normal} = \mathbf{V}_{x_L^h}$$

initialized with  $\mathbf{V}_{x_1^1} = \mathbf{v}_{x_1^1}$  with  $\Delta$  set as a small value (in our case 0.001). To make the process computationally simpler only a small set of the first 10 non-zero eigenvectors of the Laplacian  $\mathcal{L}_{x_1^p}$  were updated.

Step 3.2: the spectral graph transform is defined, which is analogous to the discrete Fourier transform. A spectral graph Fourier transform  $\hat{G}(\cdot)$  on a signal hatch  $\mathbf{x}_l^p$  can be defined as follows [105-107, 134, 135],

$$\hat{G}(\mathbf{x}_l^p) = \left[ (\mathbf{x}_l^p)^T (\mathbf{V}_{normal}) \right], \quad l = \{1 \dots L\}, p \in \{1 \dots h\} \quad (3-11)$$

Applying this inner product through all the non-contaminated layers and hatches by taking the product  $(\mathbf{x}_l^p)^T \cdot \mathbf{V}_{normal}$ , led to the graph coefficient matrix  $\mathbf{C}$ .

$$\mathbf{C} = \left[ [(\mathbf{x}_1^1)^T (\mathbf{V}_{normal}) = \mathbf{c}_{1,1}]; \quad \dots \quad ; [(\mathbf{x}_L^p)^T (\mathbf{V}_{normal}) = \mathbf{c}_{L,p}] \right] \quad (3-12)$$

$$l = \{1 \dots L\}, p \in \{1 \dots h\}$$

Essentially, each term  $\mathbf{c}_{l,p}$  is a matrix that is  $1 \times n$  long, where  $n (= 10)$  is the number of eigenvectors in the universal basis  $\mathbf{V}_{normal}$  selected for analysis. Each  $\mathbf{c}_{l,p}$  can be

visualized as a set of output variables which need to be tracked across the process – they are termed as spectral graph Fourier transform coefficients.

*Step 4: Change point detection using spectral graph Hotelling  $T^2$  control chart*

This step aims to detect material cross-contamination by tracking the spectral graph transform coefficients  $\mathbf{c}_{l,p}$ . To realize this aim, a multivariate statistical control chart called the Hotelling  $T^2$  is used [118]. The control limit of the chart was constructed based on the so-called *in-control state* which in the context of this work was defined as the non-contaminated signal. For the Hotelling  $T^2$  control chart only the upper control limit (UCL) needs to be estimated as the lower control limit (LCL) is zero. The application of the control chart proceeded in two phases. In the first phase (Phase 1), called the training phase, the upper control limit of the chart was constructed based on the spectral graph Fourier coefficients from the non-contaminated state; and in the second phase (Phase 2), called the monitoring phase, the coefficients for incoming signals for each new hatch was tracked on the chart, and their status (i.e., whether they belong to contaminated or non-contaminated state) was determined.

*Step 4.1: Phase 1 – Training the control chart*

In this phase the control limits of the chart are ascertained. Data points below the UCL were said to be *in-control*, which in the context of this work refers to a non-contaminated state. The data points falling above the UCL were termed *out-of-control*. In this research, an out-of-control point was interpreted as the onset of cross-contamination.

For setting the control limits, the photodetector signals from the two layers before the contamination was introduced, and only those from the first iteration of the build are used.

Such an exceedingly conservative strategy towards determining the control limits largely precluded the possibility of introducing signals which might be vitiated, noting that metallurgical analysis revealed that contamination tends to cascade over several subsequent layers (Figure 3-9). Accordingly, only 24 of the total 60 layers for which data was available in iteration 1 were used in the training phase, amounting to 2400 hatches. This translated to roughly 15% of the available data for 180 layers used for analysis.

The test statistic, or the point plotted on the control chart was called the  $T^2$  value and was delineated in Eq. (3-13) where  $\bar{\mathbf{C}}$  is the mean vector of the spectral graph-theoretic coefficients,  $\mathbf{\Sigma}^{-1}$  is the inverse of the covariance matrix of  $\mathbf{C}$ , and T is the transpose operator.

$$T_{l,p}^2 = (\mathbf{c}_{l,p} - \bar{\mathbf{C}})^T \mathbf{\Sigma}^{-1} (\mathbf{c}_{l,p} - \bar{\mathbf{C}}) \quad (3-13)$$

The upper control limit (UCL) of the chart was calculated using Eq. (3-14) where  $\beta_{\alpha, n/2, (hL-n-1)/2}$  is the upper  $\alpha$  tail of a Beta distribution with parameters  $n$  (the number of eigenvectors = 10), and  $h = 100$  and  $L = 24$  are the number of hatches and number of layers, respectively. In this work,  $\alpha$  set at 0.0013 for the Beta distribution, as the LCL of a Hotelling  $T^2$  was set at zero with these parameter values. The Type I error rate was found to be within 10% irrespective of the type of contamination.

$$\text{UCL} = \frac{(hL - 1)^2}{hL} \beta_{\alpha, n/2, (hL-n-1)/2} \quad (3-14)$$

Thereafter, the  $T^2$  values from Eq. (3-13) were plotted on the control chart, and the UCL was revised by removing any data points that fell erroneously above it. The re-

estimation of the control limit by removing erroneous out-of-control data was only done once and was called the delete and revise procedure.

Step 4.2: Phase 2 – Using the control chart for monitoring the process

Once the UCL of a chart is determined, the new sensor signatures are plotted upon the chart as follows. Suppose a photodetector signal  $\mathbf{y}$  is obtained for a hatch, its graph Fourier coefficients  $\hat{G}(\mathbf{y})$  is estimated as,

$$\hat{G}(\mathbf{y}) = [(\mathbf{y})^T(\mathbf{V}_{normal})] \quad (3-15)$$

The Hotelling  $T^2$  statistic, labeled  $T_y^2$  for this new sensor signature, is calculated as follows,

$$T_y^2 = (\hat{G}(\mathbf{y}) - \bar{\mathbf{C}})^T \mathbf{S}^{-1} (\hat{G}(\mathbf{y}) - \bar{\mathbf{C}}) \quad (3-16)$$

The  $T_y^2$  value is plotted on the control chart, and if it falls above the UCL, it is concluded that contamination has occurred.

We now briefly describe the statistical error measurements that underscore the effectiveness of detecting contamination in the context of a control chart. Control charts are culpable of two types of statistical errors, namely, Type I ( $\alpha$  or false alarm) and Type II ( $\beta$  or failing to detect). The Type I error rate is the percentage of data points (each data point on the control chart used in this work represented a hatch) that are falsely categorized as falling above the upper control limit when the process is in-control. In other words, a Type I error was a hatch that was falsely deemed to indicate contamination, i.e., there was no actual contamination, but the control chart erroneously indicated that contamination had occurred in that hatch.

The Type II ( $\beta$ ) error rate is the percentage of data points that fall inside the UCL when they should in reality lie outside, i.e., contamination has occurred, but the control chart fails to indicate it because the data point falls inside the control limits. However, because it was not possible to pinpoint exactly which hatch was contaminated, but it was known beforehand which layer was contaminated, accordingly, in this work the Type II error in terms of layers is estimated. The Type I and Type II error rates were estimated as follows:

Type I error rate =  $\alpha$

$$= \frac{\text{Number of hatches falsely indicated as belonging to contaminated layers}}{\text{Number of hatches expected in non – contaminated layers}}$$

$$\text{Type II error rate} = \beta = \frac{\text{Number of layers incorrectly indicated as in control}}{\text{Number of contaminated layers}}$$

There were two experimentally derived instances to verify these statistical detection errors:

- 1) Information from the experimental design, in that, the exact layers at which the contaminants were dispensed over the base powder is known.
- 2) The XCT scans of the part from which the presence of contamination on a layer could be verified, noting that the contamination was liable to spread from the layer in which it was introduced to previous and subsequent layers.

### 3.5 Results and Discussion

#### 3.5.1 Offline X-Ray Computed Tomography Analysis of the Build

The aim of this section is to understand the effect of contamination on the structure of the build. Using XCT scans additionally allows verification of the online analysis. To realize this aim, the specimen was examined using XCT along the various cutting planes demarcated in Figure 3-7. The XCT scanning was made at 225 kV with a resulting voxel resolution of 16  $\mu\text{m}$  and pixel pitch of 200  $\mu\text{m}$  on a Perkin Elmer detector. The vertical and horizontal cross sections of the 3D volume captured for the tungsten contaminated specimen is shown in Figure 3-8, wherefrom the contaminant powder is clearly discerned.

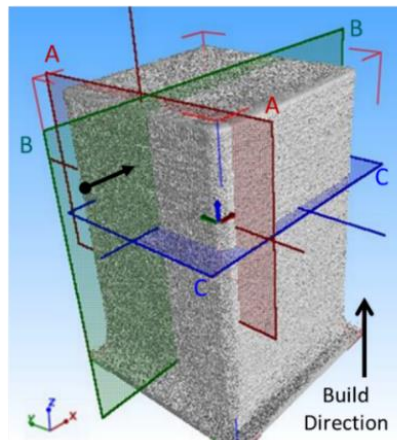


Figure 3-7. Three-dimensional reconstruction of the XCT scan image for the specimen contaminated with tungsten powder particles.

Figure 3-8(a) shows the XCT across the vertical cross-section (Y-Z plane, cutting plane A-A as depicted in Figure 3-7) of the test artifact. Observed in Figure 3-8(a) are the contaminated layers over three replicates. Closer examination of these vertical cross-sections revealed that for high tungsten contamination levels, such as L<sub>3</sub>, the tungsten particles dispersed up to three layers preceding the layer in which they were introduced, and as much as eight subsequent layers. In other words, contamination tended to cascade across layers, and influenced the structure of both the preceding and subsequent deposition.

This assertion was further corroborated through metallurgical analysis in Figure 3-9. Similarly, Figure 3-8(b) shows the effect of contamination as viewed along the X-Z direction (cutting plane B-B); Figure 3-8(c) is the cross-section taken along the X-Y direction (cutting plane C-C). It is noted that in Figure 3-8(a) and (b), due to procedural lapses during XCT scanning, the second level of tungsten contamination for the first iteration (L<sub>2</sub>-1) was not captured. This missing data is demarcated by a star in Figure 3-8(a) and (b). In the context of aluminum contamination, Figure 3-10 shows the vertical cross sections of the specimen; aluminum trace particles were not detected with XCT. To reiterate, aluminum contaminant particles were not discernable in the XCT images, because, (a) aluminum is an alloying element in Inconel 625, and (b) the melting point of aluminum (~ 660 °C) is much lower than the melting point of Inconel 625 (~ 1300 °C). Consequently, aluminum readily dissolves into the surrounding Inconel 625 matrix, and is therefore undetected in the XCT. Additionally, aluminum may have also vaporized due to the high energy density (~ 70 J/mm<sup>3</sup>) applied in the process to melt Inconel 625.

The specimen with embedded tungsten contaminant was sectioned and primary etched with an alcohol-based Kalling's solution. The specimens were secondary etched using a 10% weight chromic acid solution at 2.4 volts. In the optical micrograph of the etched sample shown in Figure 3-9(a) the presence of tungsten contaminants in the Inconel 625 matrix is evident. More remarkably, tungsten particle traces were observed not just in the layer in which they were introduced, but also over multiple layers – both preceding and subsequent layers. The spread of contaminants to layers beyond which they were introduced was hypothesized as the effect of the repeated remelting of the material. However, modeling of the melt pool dynamics is required for confirming this effect. Recent computational

modeling work at Lawrence Livermore National Laboratories by King *et al.* towards simulating the melt pool dynamics showed that material reflow and remelting influence the structure of the previous layers, and may even be used beneficially to control and mitigate defects, such as porosity[136]. Further investigation in this direction to elucidate how and why material contamination cascades across layers is beyond the scope of this work.

The cascading effect of contamination was further verified in the XCT observations in Figure 3-9(b). The XCT cross-section in Figure 3-9(b) was taken in the X-Y plane, the label  $n$  refers to the layer in which contamination was introduced,  $n-1$  is the immediate preceding layer,  $n-2$  is two layers prior, and so on. Similarly, a plus sign is used to indicate layers subsequent to layer  $n$ . The ensuing section, Sec. 3.5.2 applies a spectral graph-theoretic approach to capture these instances of contamination during the build using data from the photodetector.

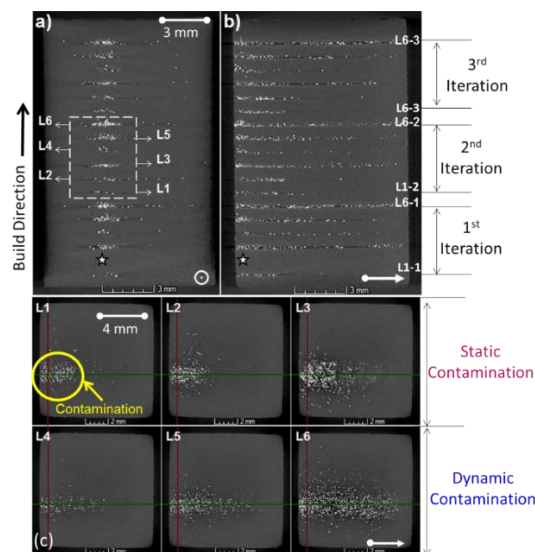


Figure 3-8. The cross sectional XCT views of the Inconel 625 specimen contaminated by the tungsten particles. (a) vertical cross section normal to the recoating direction (A-A, Y-Z direction, b) vertical cross section along the recoating direction (B-B, X-Z direction) c) horizontal cross section (C-C, X-Y direction). Due to procedural lapses in the XCT process the second contamination level in the first iteration (L2-1) was missed.

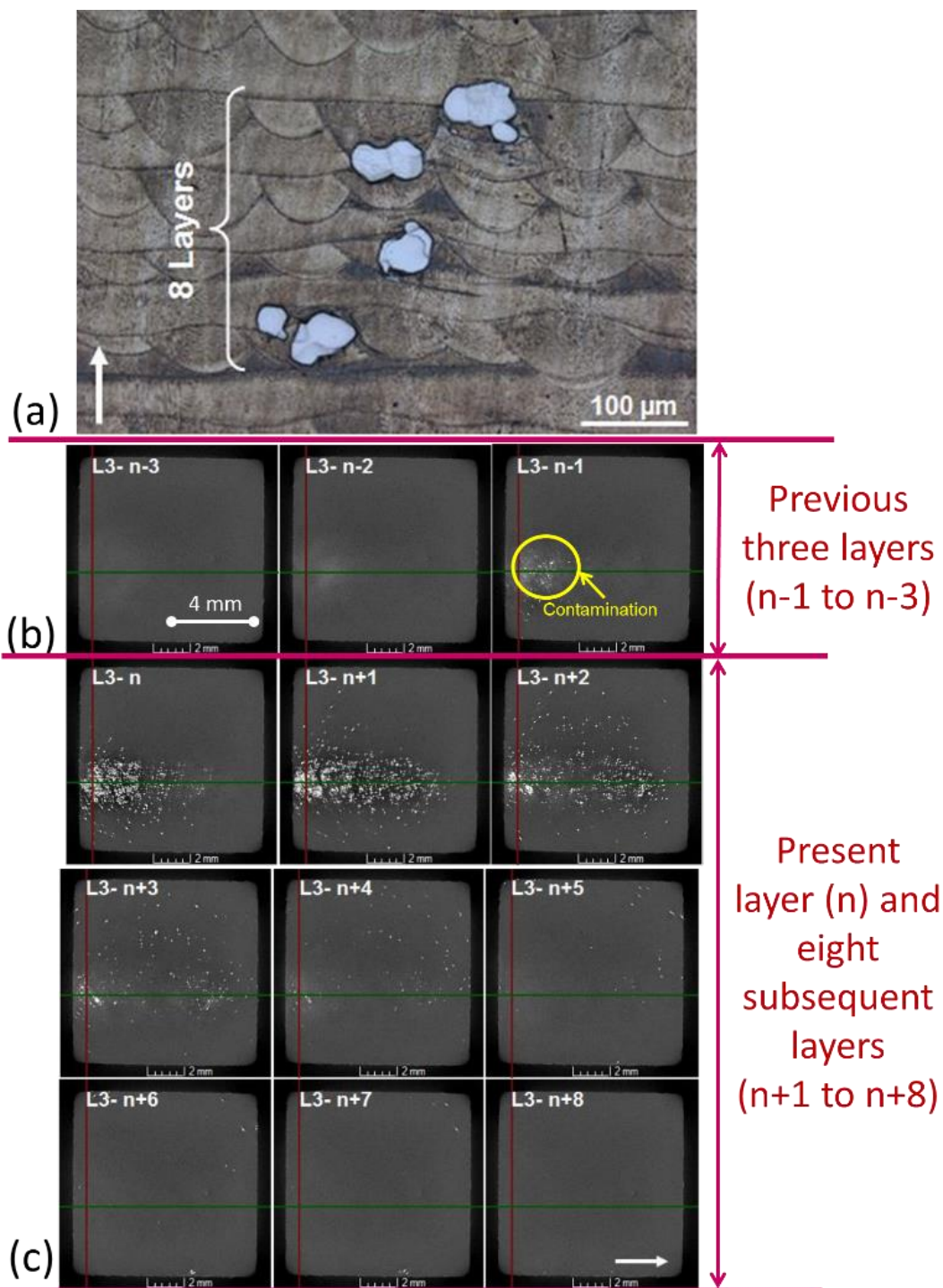


Figure 3-9: The microstructure of the inconel 625 specimen contaminated with tungsten particles. (a) optical micrograph (b) XCT images in the horizontal plane section (cutting plane C-C, X-Y direction) for the L<sub>3</sub> severity level show that trace tungsten particles persist over eight subsequent layers and penetrate through three preceding layers.

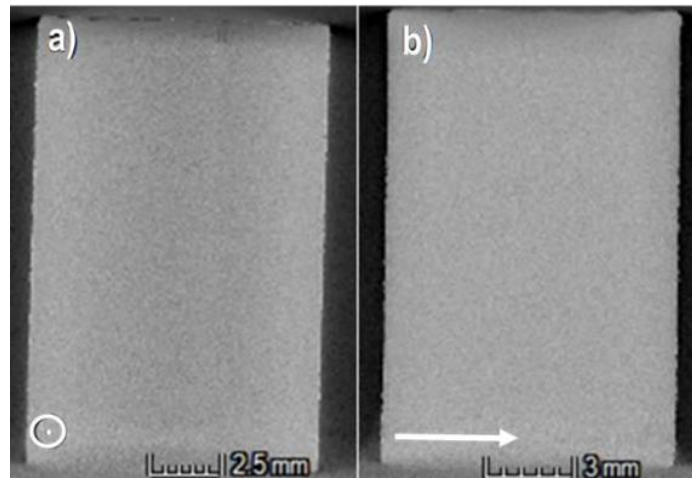


Figure 3-10: The cross-sectional views of the Inconel 625 specimen contaminated by the Aluminum powder particles.

(a) vertical cross section normal to the recoating direction (cutting plane A-A, Y-Z direction), (b) vertical cross section along the recoating direction (cutting plane B-B, X-Z direction). The contaminant particles are not evident within the aluminum matrix.

### 3.5.2 Online Spectral Graph-Theoretic Analysis of the Signal

The photodetector signal related to the six levels of tungsten and aluminum contamination for one iteration are shown in Figure 3-11(a) and (b), respectively. The layers contaminated with tungsten portrayed significant peaks. However, such a clear change was not apparent in the photodetector signal for the aluminum contamination case. Herewith, a physical explanation of the signal characteristics is provided.

Because the photodetector signal essentially captures the optical intensity of the plume during the melting process, it was reasoned that it is intimately related to the laser-material interaction. This effect has been observed by the AM research group at Penn State Applied Research Laboratory in both LPBF and DED processes [126, 127]. In these pioneering works, researchers showed that the photodetector signal is connected to the intrinsic microstructure of the part. In a similar vein, in this work, when the laser passed over the powder bed area having contaminant particles, the optical intensity of the vapor plume

changed, which was captured by the photodetector, and hence it is related to the elemental material aspects. The justification for this reasoning is as follows.

A crucial difference between this work, and the research reported by the Penn State group is that the latter used two photodiodes that captured two different wavelength intensities, one at 520 nm (called line emission spectrum) and 530 nm (called continuum spectrum) [126, 127]. The ratio of the two spectra (line to continuum ratio) has been shown in three successive works by this group to be strongly correlated to pore severity in both LPBF and DED, and hence can be deemed to capture the microstructure-level aspects.

In our present work, an unfiltered signal from a single photodiode was used. On juxtaposing the photodiode signal resulting from contamination from tungsten (Figure 3-11[a]) and aluminum (Figure 3-11[b]), it was evident that, when tungsten contamination occurred, the amplitude of the signal (Volts) increased sharply from 1V to over 3V. Whereas, for the case of aluminum contamination, barely any increase was evident. This observation that the photodiode voltage was dependent on the contaminant material, led to the inference that the photodiode signal in this work is inclined to be element-specific.

In this section, the proposed spectral graph-theoretic algorithm is applied to the LPBF process with the aim of detecting the onset of aluminum and tungsten cross-contamination from the photodetector signals. First, the photodetector signal for the non-contaminated state was apportioned hatch-by-hatch for each layer. This was possible because the laser position was tracked and recorded throughout the build. The photodetector signal for each hatch  $p$  for layer  $l$  is denoted as  $x_l^p$  in Eq. (2-2).

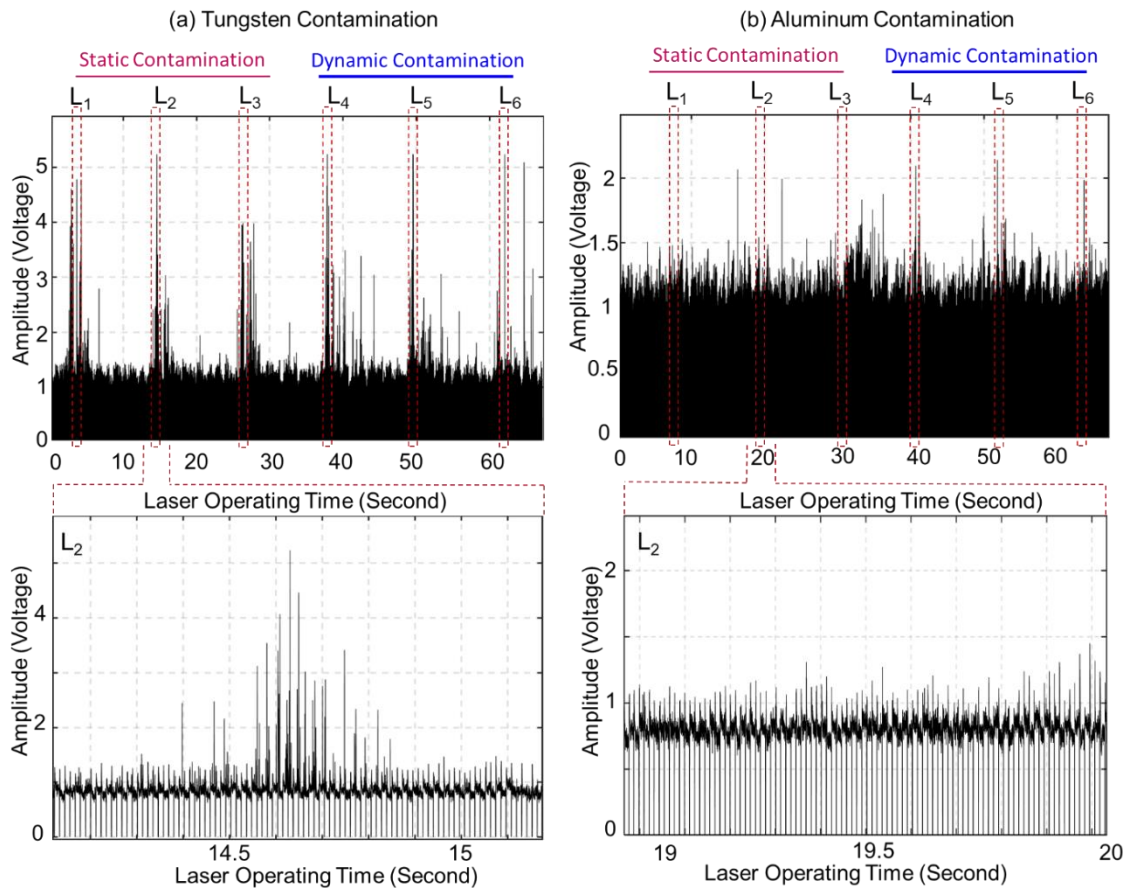


Figure 3-11: The photodetector signal associated with the six levels of contamination. (a-top row) Tungsten contamination and (b-top row) Aluminum contamination in Inconel 625. (bottom row) The second contamination level ( $L_2$ ) is magnified and the signal corresponding to tungsten contamination has clear spikes compared to aluminum.

We noted that there was no clear correlation evident in the amplitude of the signal and the severity of the signal – the statistical features of the signal could not discriminate between different types and levels of severity. Next, using Eq. (2-3) and (2-5), the pairwise comparison between different rows of photodetector hatches was performed to provide the similarity matrix  $\mathcal{S}$  related to graph  $G \equiv (V, E, W)$ . Going through the second step, the Laplacian matrix of graph  $\mathcal{L}$  was constructed using Eq. (2-9). Then the first 10 ( $= n$ ) non-zero Laplacian eigenvectors  $\mathbf{v}_i, i = \{2 \dots 11\}$  were used to build a spectral universal basis  $\mathbf{V}_{normal}$  necessary for spectral transformation (Eq. (2-14)). Subsequently, the spectral

graph Fourier coefficients ( $\mathbf{C}$ ) were obtained by taking the inner product  $(\mathbf{x}_l^p)^T (\mathbf{v}_{normal})$  per Eq. (3-12).

Finally, the coefficients  $\mathbf{C}$  were traced on a Hotelling  $T^2$  control chart. Per the procedure for building the Phase 1 control chart described in Step 4.1, the UCL was first estimated by only considering the so-called in-control signal, viz., those layers not contaminated with tungsten or aluminum particles. As mentioned previously, this was restricted to 24 of the 60 layers for the first iteration of the build with approximately 100 hatches per layer. The  $T^2$  statistics and UCL were calculated based on Eq. (3-13) and (3-14).

The Phase 1 spectral graph-theoretic Hotelling  $T^2$  control chart along with the data for the six levels of tungsten and aluminum contamination for the first iteration are shown in Figure 3-12. There were a total of 6000 hatches (60 layers) for which the data was available in the first iteration. Each point of the control chart was representative of the spectral graph coefficients for one hatch. It was observed that the chart captured the occurrence of contamination almost instantaneously.

The Type I error was  $\approx 1\%$  for both tungsten and aluminum contamination in building the Phase 1 control chart. This Type 1 error was obtained after revising the control limit by removing the outliers (the so-called delete and revise procedure applied only once). This manner of constructing the control limit was an extremely conservative strategy that prioritized the Type I error rate over the Type II error rate. In other words, the Type I error for the control chart was maintained close to 1%, while the Type II error was estimated based on the results. Furthermore, the control limits for a type of contaminant material (tungsten or aluminum) remained fixed.

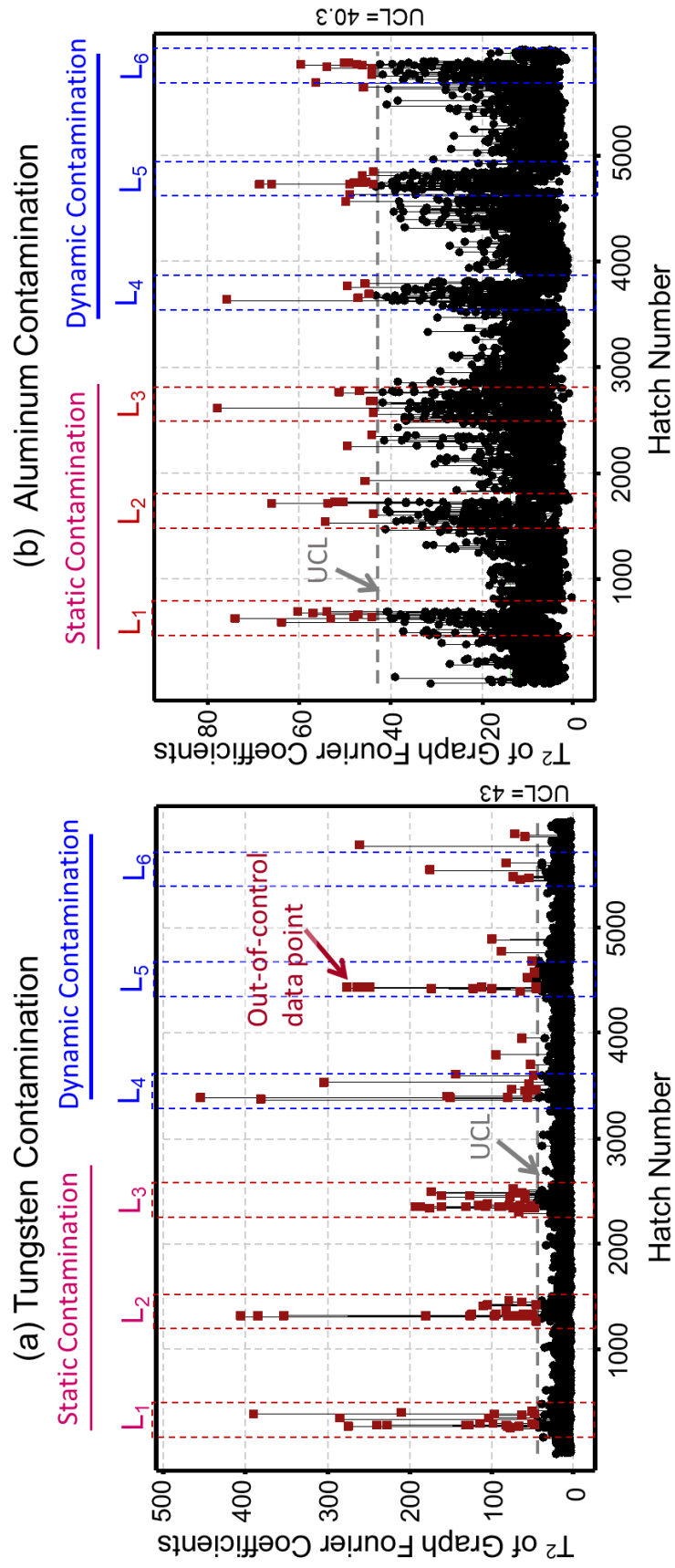


Figure 3-12: The Phase 1 spectral Hotelling  $T^2$  control chart related to six levels of contamination.

(a) Tungsten and (b) Aluminum contamination, wherein the control limits are fixed.

Next, following the procedure in Step 4.2, the Hotelling  $T^2$  chart was used to detect contamination in the rest of the two experimental iterations of the build. The data was representative of 120 layers, with each layer having 100 hatches for a total of 12,000 hatches. To plot the spectral control chart for the other replicates, the UCL stayed identical to Phase 1 in Figure 3-12. As new data  $\mathbf{y}$  arrived, it was multiplied with the universal basis  $\mathbf{V}_{normal}$  to extract the first ten spectral graph Fourier coefficients  $\hat{G}(\mathbf{y})$  as shown in Eq. (3-15). Subsequently,  $T_y^2$  was obtained in Eq. (3-16), and plotted on the control chart. This simple inner product made this approach suitable for online monitoring.

Figure 3-13 shows the application of the Phase 2 control chart to each type of contamination (tungsten and aluminum) over iteration 2 and 3 (i.e., L<sub>1-2</sub> through L<sub>6-2</sub> and L<sub>1-3</sub> through L<sub>6-3</sub>). Every level of tungsten contamination, both static and dynamic, was detected promptly by the control chart in Figure 3-13(a). Whereas, as evident in Figure 3-13(a), in the case of aluminum contamination, the contamination level L<sub>5-3</sub> (dynamic contamination type) was missed (an example of a Type II error). This underscores some of the challenges with contamination detection.

Table 3-2 summarizes the Type I and Type II errors estimated from three replicates of the experiment in detecting powder contamination. It is noted that because it is intractable to pinpoint *a priori* the exact hatch where contamination has occurred, the Type II errors are reported in terms of all the hatches for the entire layer where contaminants were added. In contrast, it was known for certain whether a hatch belonged to a non-contaminated layer, hence the Type I error could be localized with respect to every hatch.

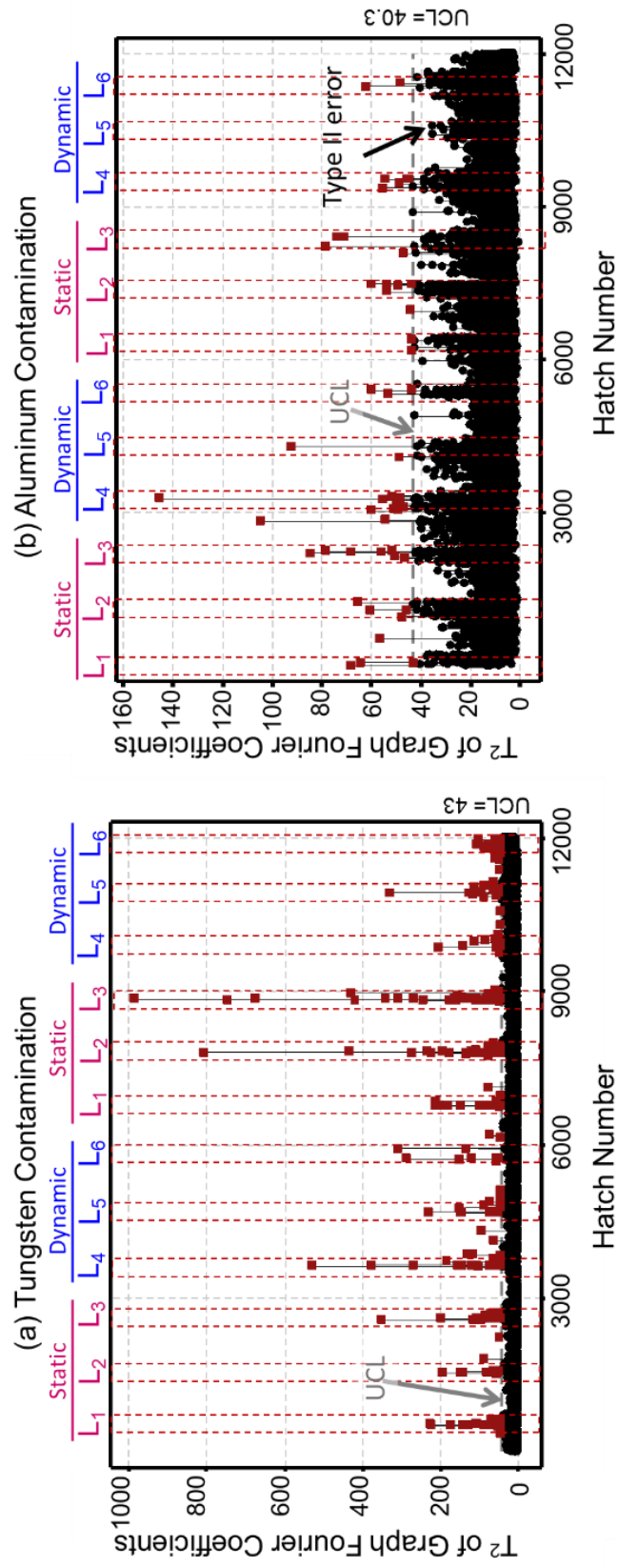


Figure 3-13: The Phase 2 spectral Hotellinging  $T^2$  control chart applied to two replications of the data for the remaining two iterations, for each of the six levels of contamination.

(a) tungsten and (b) aluminum contamination. Note that the dynamic contamination, case  $L_5$  for aluminum is not detected, indicating a Type II statistical error.

Table 3-2: The algorithm accuracy in comparison with traditional approaches. for detecting the Tungsten and Aluminum contamination. The numbers in the parenthesis are from three-fold experimental replications.

Model	Model Structure	Aluminum Contamination		Tungsten Contamination		Computation time per hatch (sec)
		Type I error (%)	Type II error (%)	Type I error (%)	Type II error (%)	
ARMA	(2,2)	0.6 (0.1)	83.3 (0.0)	1.0 (0.1)	0.0 (0.0)	0.0912
	(2,4)	0.6 (0.1)	83.3 (0.0)	1.0 (0.1)	0.0 (0.0)	0.0971
	(2,6)	0.6 (0.1)	83.3 (0.0)	1.0 (0.0)	0.0 (0.0)	0.1021
	(4,2)	0.7 (0.1)	83.3 (0.0)	1.2 (0.1)	0.0 (0.0)	0.0968
	(4,4)	0.7 (0.1)	83.3 (0.0)	1.3 (0.2)	0.0 (0.0)	0.0976
	(4,6)	0.8 (0.2)	66.7 (16.7)	1.2 (0.0)	0.0 (0.0)	0.1302
	(6,2)	1.2 (0.1)	33.3 (17)	1.0 (0.1)	0.0 (0.0)	0.1588
	(6,4)	1.7 (0.1)	16.7 (9.2)	1.0 (0.1)	0.0 (0.0)	0.2829
ARIMA	(2,2)	0.6 (0.2)	83.3 (0.0)	0.8 (0.1)	0.0 (0.0)	0.1128
	(2,4)	0.5 (0.1)	83.3 (0.0)	0.9(0.1)	0.0 (0.0)	0.1216
	(2,6)	0.7 (0.2)	83.3 (0.0)	0.9 (0.0)	0.0 (0.0)	0.1225
	(4,2)	1.1 (0.1)	66.7 (16.7)	1.3 (0.0)	0.0 (0.0)	0.2164
	(4,4)	1.2 (0.0)	66.7 (16.7)	1.3 (0.10)	0.0 (0.0)	0.2576
	(4,6)	1.1 (0.0)	66.7 (16.7)	1.2 (0.1)	0.0 (0.0)	0.1560
	(6,2)	1.5 (0.1)	11.1 (9.6)	1.6 (0.2)	0.0 (0.0)	0.2011
	(6,4)	1.6 (0.1)	11.1 (9.6)	1.6 (0.1)	0.0 (0.0)	2.4152
AR	(2)	1.0 (0.0)	22.2 (19.2)	1.0 (0.20)	0.0 (0.0)	0.0210
	(4)	1.1 (0.1)	16.7 (9.2)	0.9 (0.3)	0.0 (0.0)	0.0089
	(6)	0.8 (0.2)	16.7 (9.6)	0.9 (0.1)	0.0 (0.0)	0.0080
	(8)	0.7 (0.10)	16.7 (9.6)	0.9 (0.1)	0.0 (0.0)	0.0085
	(10)	0.5 (0.1)	33.3 (17)	0.8 (0.2)	0.0 (0.0)	0.8641
Statistical Control Chart		1.5 (0.0)	11.1 (9.6)	1.3 (0.7)	0.0 (0.0)	0.0427
Spectral Graph-Theoretic		0.5 (0.0)	5.0 (9.2)	1.1 (0.1)	0.0 (0.0)	0.0008

### 3.5.3 Verification with Statistical Time Series Analysis

The results from the proposed approach were compared with traditional delay-embedded Box-Jenkins stochastic time series models, such as autoregressive (AR), autoregressive moving average (ARMA), and autoregressive integrative moving average (ARIMA) models [137]. Starting with the simplest model with two autoregressive terms, the model search was stopped when the number of terms in the model reached 10. The stopping criteria was chosen so that the number of terms in the most complicated model did not exceed the number of eigenvectors ( $n = 10$ ) used in the spectral graph-theoretic approach.

For instance, Eq. (3-17), (3-18), and (3-19) show the AR(10), ARMA(6,4), and ARIMA(6, 4), respectively [137]. Where  $\mathbb{L}$  is the lag operator, such that  $\mathbb{L}^i(x_t) = x_{t-i}$ ,  $x_t$  is a photodetector data point (i.e., the amplitude of the photodetector signal at time  $t$ ). The parameter  $\alpha_i$  is connected to the AR part of the time series model,  $\theta_i$  are the parameters of the moving average (MA) part, and  $\varepsilon_t$  are model error terms. The terms  $\alpha$  and  $\theta$  are optimized using the time series modeling toolbox in Matlab, such that the sum of squared errors, i.e.,  $\sum_{\forall t} \varepsilon_t^2$ , is minimized.

$$\text{AR}(10) \text{ model: } (1 - \sum_{i=1}^{10} \alpha_i \mathbb{L}^i)x_t = \varepsilon_t \quad (3-17)$$

$$\text{ARMA}(6,4) \text{ model: } (1 - \sum_{i=1}^6 \alpha_i \mathbb{L}^i)x_t = (1 + \sum_{i=1}^4 \theta_i \mathbb{L}^i)\varepsilon_t \quad (3-18)$$

$$\text{ARIMA}(6,4) \text{ model: } (1 - \sum_{i=1}^6 \alpha_i \mathbb{L}^i)(1 - \mathbb{L})x_t = (1 + \sum_{i=1}^4 \theta_i \mathbb{L}^i)\varepsilon_t \quad (3-19)$$

In Phase 1, the model coefficients  $\alpha$  and  $\theta$  were trained to fit the data hatch-by-hatch (using Matlab), and then these model coefficients were tracked on a Hotelling  $T^2$  control chart. The procedure followed is identical to the one described previously for the spectral

graph-theoretic approach in Sec. 3.5.2. The only difference is that  $\alpha$  and  $\theta$  were used to populate the library of coefficients  $\mathbf{C}$  per Eq. (3-12) instead of the spectral graph Fourier coefficients  $\hat{G}(\mathbf{x}_l^p)$ .

For each model, the Hotelling  $T^2$  control chart was constructed and the Type I and Type II errors were estimated using the same procedure used for the proposed spectral graph-theoretic approach. The Phase 2 results for the traditional stochastic time series methods are presented in Table 3-2, from which it is evident that the onset of material cross-contamination was promptly detected in the case of tungsten contamination; the Type II ( $\beta$ ) error rate was negligible for tungsten contamination and the Type I ( $\alpha$ ) error was less than 1% for a majority of cases. However, detection of aluminum contamination was rather intractable with these existing traditional Box-Jenkins time series approaches; the Type II error exceeded 10%.

These results were further juxtaposed with a Hotelling  $T^2$  control chart built with statistical features extracted from each hatch, such as mean, standard deviation, skewness, etc. The results depicted in Table 3-2 also provide the average computation time for extracting the  $T^2$  values for one hatch in the Phase 2 part of the control chart. It is noted that the computation time for the proposed graph-theoretic approach was less than a millisecond ( $\sim 0.8$  millisecond), which is a magnitude smaller in comparison to traditional approaches, and thus attests to the viability of the approach for real-time process monitoring in AM.

### 3.5.4 Consistency Between Spectral Graph Theory and XCT

Continuing with the analysis, since the position data for each hatch of the photodetector signal was available, the spectral graph  $T^2$  coefficients could be correlated with the layer-by-layer contamination pattern obtained from the XCT scan. Such an attempt is made in Figure 3-14 for the tungsten contamination case. In Figure 3-14(a), the Hotelling  $T^2$  values for the spectral graph coefficients are color-coded, with red indicating out-of-control or contaminated hatches. These color-coded  $T^2$  values are superimposed on the XCT of the specimen taken along the X-Z cross-section in Figure 3-14(b); the XCT is along the cutting plane B-B in Figure 3-7. From the overlaid plot in Figure 3-14(b) it is evident that there was a near one-to-one correlation between the sensor signatures and the layer at which contamination occurred.

However, such an overlaid plot for the aluminum contamination case could not be produced, because the XCT of Inconel 625 specimens contaminated with the aluminum particles did not show visually prominent inclusions (Figure 3-10). To reiterate, the XCT of parts with aluminum was not informative, because, (a) aluminum particles may dissolve within the Inconel 625 matrix given their low melting temperature relative to Inconel 625 ( $\sim 660\text{ }^\circ\text{C}$  vs.  $\sim 1300\text{ }^\circ\text{C}$ ), and (b) aluminum vaporizes due to the high energy density ( $70\text{ J/mm}^3$ ) applied to process Inconel 625. This result corroborated that the spectral graph sensor signatures were indeed indicative of material cross-contamination and could be traced back to physical locations where contamination was present. This traceability of sensor signatures to XCT demonstrates the viability of the *qualify-as-you-build* paradigm in AM, in which in-process sensor data instead of cumbersome offline measurement and testing can be used to rapidly qualify the part quality.

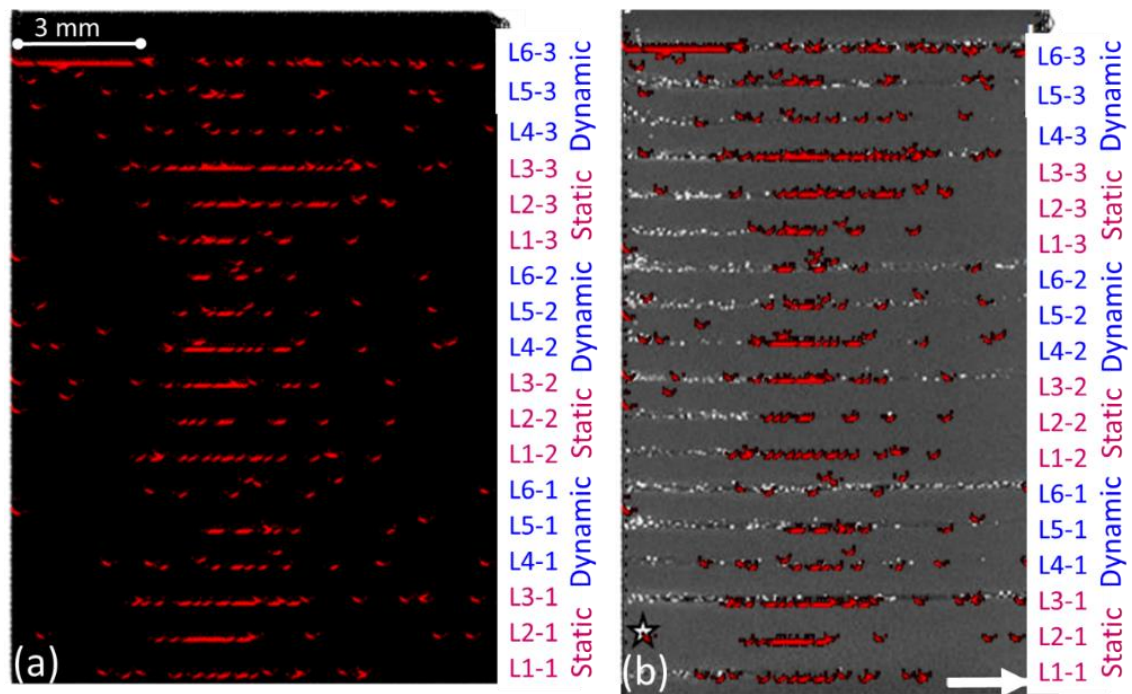


Figure 3-14: (a) The color coded  $T^2$  values of the spectral graph Fourier coefficients.

Red indicates out-of-control (contaminated) hatches, and black indicates in-control hatches. These  $T^2$  values are plotted along the X-Z plane of the part, since the position of each hatch is known. (b) The spectral graph  $T^2$  values are overlaid upon the XCT scan to demarcate the near one-to-one correspondence between the two.

Furthermore, through this research, once the presence of contaminants was discovered at a layer, measures to forestall their spread further over future layers could be taken. Such a preventive strategy could be, for instance, rescanning an entire layer with higher energy density to ensure thorough fusion of contaminant particles like tungsten, or removing a layer using a hybrid additive-subtractive strategy. This in-process correction strategy is possible with hybrid LPBF systems, e.g., Matsuura Lumex Avance and Sodick OPM250L, which have an in-built subtractive machining attachment that can be used to remove a contamination-afflicted layer. In the worst-case scenario, the build could be stopped to prevent poor part quality and waste of expensive powder.

### 3.6 Conclusions

This work describes a spectral graph-theoretic approach to detect occurrence of material cross-contamination in the laser powder bed fusion (LPBF) additive manufacturing (AM) process based on in-process sensor data. The key idea is to convert a signal into its network graph equivalent, and subsequently, extract so-called spectral graph Fourier coefficients as surrogate signatures to track the process hatch-by-hatch. A photodetector signal was specifically used to demonstrate the efficacy of the approach of an LPBF of an Inconel 625 alloy part. During the build, two types of foreign material contaminants were introduced, namely, tungsten and aluminum, varying in the severity and the controlled manner in which they were introduced – static deposition, and dynamic/continuous deposition over a layer.

The key advantages of this approach over existing time-delay stochastic time series modeling techniques, such as ARMA is that: (a) it does not require fitting a model to the data; essentially it is model-free, and (b) it eschews decomposition or extraction of features from each incoming signal; a simple inner product with an eigenvector basis is required, thus saving on computational time. As a result, the approach detects instances of material contamination with high accuracy; the worst-case Type I error was found to be  $< \sim 1\%$ , and the Type II error  $< 5\%$ , which presents a magnitude improvement over traditional time series modeling. The ability to detect contamination was corroborated with offline metallurgical and XCT scanning.

Specific conclusions from this work are enumerated below.

1. Metallurgical and XCT analysis of specimens revealed that contaminants are not confined to the layer in which they were introduced. Indeed, it was observed that contaminant particles not only entered previously deposited layers, but also tended to cascade to subsequent layers. The repeated re-melting of the material is hypothesized as the root cause of the behavior that leads to cascading of contamination to previous and subsequent layers. Physical modeling to explain the transportation of contaminant particles across layers is beyond the scope of this work.
2. Tungsten contamination is readily discernable in both offline metallurgical and XCT images, and online photodetector signals. This is probably because tungsten has a higher melting point and is also not elemental to Inconel 625. In contrast, aluminum has a lower melting point than Inconel 625 and may be present as an alloy in minor quantities (< 0.4%) in the same. There is also the possibility that aluminum may be vaporized during the build (which causes pinhole porosity). Therefore, contamination of Inconel 625 with aluminum was harder to discern in either the XCT or photodetector signals than the tungsten contamination case.
3. The graph Fourier coefficients were extracted for each hatch of the material and traced in a Hotelling  $T^2$  control chart. The occurrence of both tungsten and aluminum contamination were detected with high fidelity using the spectral graph Fourier coefficients; the Type I and Type II errors were  $< \sim 1\%$  and  $< 5\%$ , respectively.
4. The Hotelling  $T^2$  values obtained from the spectral graph-theoretic Fourier coefficients were overlaid on the XCT scans of the specimen. A near one-to-one correlation was demonstrated between the status of the Hotelling  $T^2$  values—whether they are in-control or out-of-control – and the layer at which contamination was observed in the XCT.

## 4 Detecting Lack-of-Fusion Porosity in LPBF

### 4.1 Goal, Objectives, and Hypothesis

The objective of this work is to first detect lack-of-fusion porosity that results from the incomplete melting of the powder material, and subsequently, to predict the level or severity of porosity using in-process optical emission spectroscopy signatures. To realize this objective, the line-to-continuum ratio of Chromium emission around 520 nm was monitored during LPBF of Inconel 718 (UNS N07718) powder feedstock [126, 127, 138]. Next, a graph-theoretic approach is developed and applied to analyze the acquired line-to-continuum optical emission signatures. The graph-theoretic approach transforms the line-to-continuum measurements into features called Laplacian eigenspectra. These graph-theoretic features were subsequently used as derived process signatures to predict the level of porosity layer-by-layer through three types of machine learning models. The correlation between the predicted and actual level of porosity was verified via offline XCT of the parts. Accordingly, the underlying hypothesis is that the Laplacian eigenspectra extracted from the in-process spectral signatures are statistically distinctive discriminants of the level of porosity in LPBF parts.

The rest of this study is organized as follows. A review of the literature, focused on optical spectroscopy monitoring in metal AM, is provided in Sec. 4.2. In Sec. 4.3 the research methodology encompassing the experimental procedure, sensing, and data acquisition is described. This is followed by discussion of the results and conclusions in Sec. 4.5, and Sec. 4.6, respectively.

#### 4.2 Prior Work and Challenges at Optical Spectroscopy in LPBF

Several comprehensive review articles have been recently published describing sensing techniques for process monitoring in metal AM processes [31, 83]. Here, the primary focus is on optical emission-based techniques utilizing single-point photodetectors, e.g. photodiodes and spectrometers. While sensors, such as infrared thermal cameras and optical imaging are capable of providing high-resolution, image-based data that can detect defects [66], the advantage of using photodetectors and spectrometers in AM is their fast response rates (sampling rates exceeding 100 kHz are possible) and relatively low cost [139]. In metal AM, photodetectors and optical spectrometers (which essentially consist of an array of photodetectors) are primarily used to measure the intensity and wavelength, respectively, of the light emitted in the laser-material interaction region.

Mazumder *et al.* have pioneered the use of photodetectors for closed-loop control in metal AM, albeit, in the specific context of the directed energy deposition (DED) metal AM process[140]. One of their early works describes the use of three photodetectors for closed-loop control of the surface finish, geometry, and microstructure of the part by modulating the energy density via changing the build height[140]. As a result of this closed-loop control strategy, the surface roughness improved by as much as 20%, and parts with unusual bulk properties, such as the negative coefficient of thermal expansion, were produced.

Recent patents by Mazumder *et al.* also describe the use of optical spectrometry-based closed-loop control in DED [141, 142]. Through various examples, including DED of titanium and nickel-based superalloys, Mazumder *et al.* showed that the intensity of the line emissions correlate with the level of phase transformation in the material. This relationship was further extended for prediction of the microstructure of the resulting material. Furthermore, the use of an optical spectroscopy approach was also demonstrated for the monitoring of defects, and detection of undesirable DED process conditions such as lack of deposition and overbuilding. By tying the optical emissions to specific process variables, e.g., laser power and laser spot size (beam diameter), a closed-loop control schema for tailoring the microstructure can be envisioned. Mazumder *et al.* have termed such a sensor-based closed-loop control of AM a *smart additive manufacturing system* [141].

Song and Mazumder further demonstrated the use of a two-color pyrometer to measure the melt pool temperature [143]. The temperature measurements from the pyrometers were coupled with a generalized predictive controller for attaining a desired microstructure in tool steel. In this case, the controller adjusted the voltage delivered to the laser to modulate the volumetric energy density. A similar work with a combination of CCD cameras and a two-color pyrometer for controlling the build height has also been reported by the Mazumder group [139].

In a similar vein, Nassar *et al.* have demonstrated a correlation between the line-to-continuum ratios around certain titanium emission lines during DED of Ti-6Al-4V and lack-of-fusion [127, 138]. They isolated lack-of-fusion in Ti-6Al-4V using optical

emissions spectroscopy around 430 nm and 520 nm, as well as using a camera filtered around 430 nm.

The main drawback in these pioneering works is in the application of rudimentary signal processing techniques to extract signatures from in-process sensors for isolating one type of defect or phenomena at a time through an experiment designed to initiate the desired effect. In practical implementation, however, multiple defects with varying severity can occur simultaneously. Furthermore, defects in AM can occur even if the process is maintained at an optimal parameter set point. Here, graph theory is applied to reduce sensor data and apply machine learning to discriminate porosity levels in LPBF parts.

### 4.3 Experimental Setup and Data Acquisition

#### 4.3.1 Part Build Conditions

In this work, cylindrical test parts (discs) were built on a 3D Systems ProX DMP 200 LPBF machine. Each disc was 12 mm in diameter and 6.6 mm in height. The build direction was parallel to the axis of each cylinder. Laser power ( $P$ , W), laser scan velocity ( $V$ , mm/s), and hatch spacing ( $H$ , mm) were varied for each disk. Five discs, labeled A through E, were selected for analysis — processing parameters for each of these discs are listed in Table 4-1, and their relative location on the build plate is shown in Figure 4-1. The parts were characterized post-process using X-Ray Computed Tomography (XCT); Figure 4-2 exemplifies a representative XCT slice from five discs processed at varying global volumetric energy densities. Additionally, based on Figure 4-2, an obvious relationship between global volumetric energy density ( $E_V = \frac{P}{V \times H \times T}$  J/mm<sup>3</sup>) and porosity was not visually evident. While porosity discernably decreased for Disc C through Disc E,

corresponding to an increasing  $E_v$ , the relationship did not hold for Discs A and B. This indicates that factors beyond power, speed, and layer thickness influence the likelihood of flaw formation.

It is noted that, because Discs D and E were both found to be largely devoid of pores, Disc E is not used for further analysis. This was done so that there were roughly an equal number of layers corresponding to the different levels of porosity. Having an equal number of representative data further prevented biasing the machine learning models used in this work.

Table 4-1: The build conditions for the five disks used in this study.

Disc	Laser Power [W]	Laser Scan Velocity [mm/s]	Hatch Spacing [ $\mu\text{m}$ ]	Energy Density [ $\text{J}/\text{mm}^3$ ]
A (H-50%)	300	2500	25	160
B (P0, V0, H0)	300	2500	50	80
C (V-25%, H+50%)	300	1875	75	53
D (V-25%)	300	1875	50	107
E (V-25%, H-50%)	300	1875	25	213

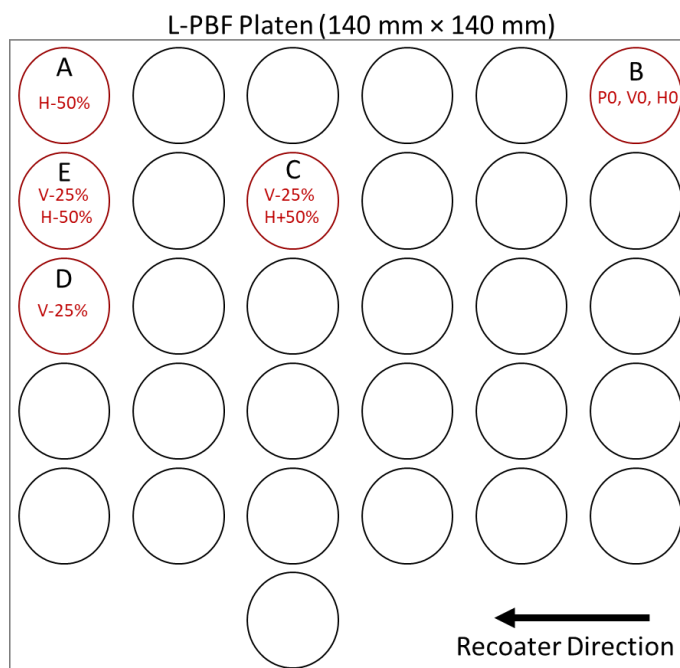


Figure 4-1: The relative location of the discs A through E on the build platen.

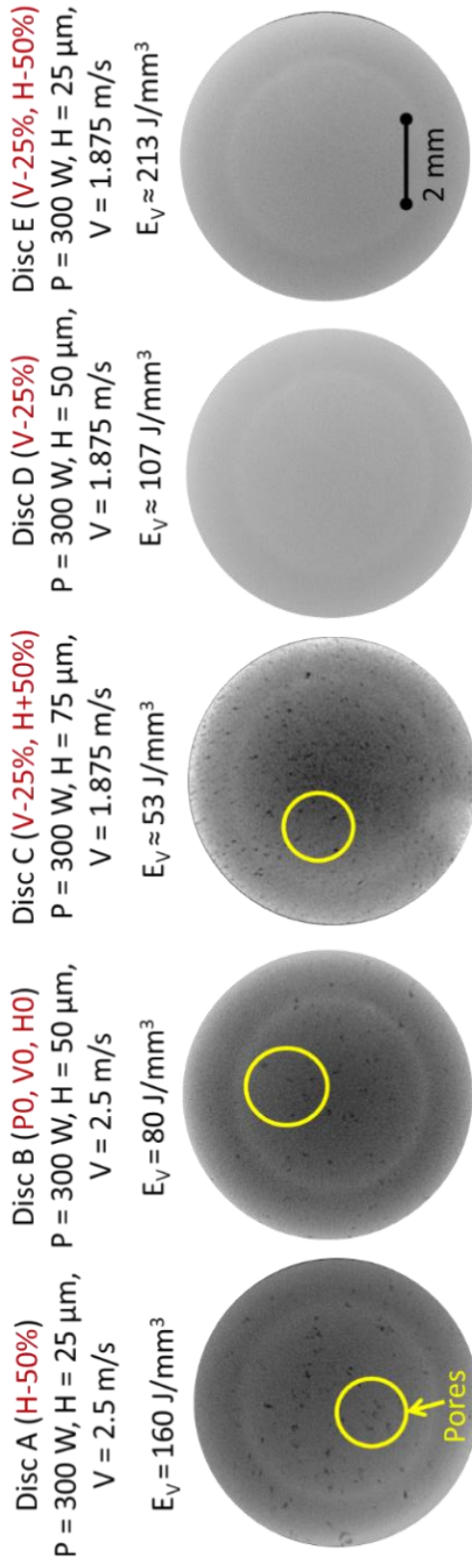


Figure 4-2: The five discs used for analysis in this work.  
 The discs are made by varying the power (P), velocity (V), and hatch spacing (H) settings.

### 4.3.2 Sensor Instrumentation

The ProX 200 machine is equipped with a photodetector-based sensor detailed in previous researches [126, 127]. The sensor measures the line-to-continuum ratio of chromium emission lines around 520 nm. As shown in the schematic diagram in Figure 4-3, the sensor array consisted of two off-axis photodetectors (photodiodes) that captured light from the laser-material interaction zone.

A custom optical system was used to image the build plate of the LPBF machine (140 mm  $\times$  140 mm) onto the sensor of each photodiode. Bandpass optical filters were used to capture emissions around 520 nm and 530 nm (10 nm FWHM)—this approach is detailed in the authors previous works [126, 127, 138]. The output current of each photodetector was amplified and converted to a voltage, which was sampled at 100 kHz. Photodetector outputs were synchronized with the laser scanner position, laser trigger, and laser power output. Hence, the part geometry and scan pattern were matched one-to-one.

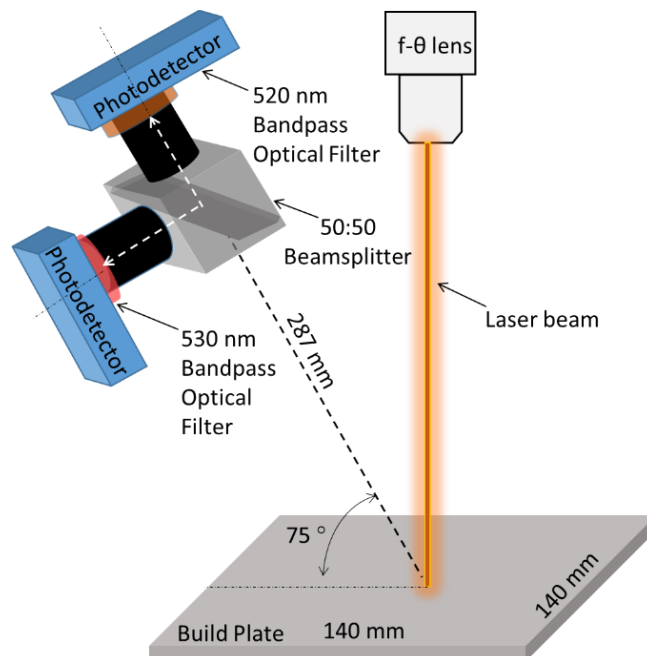


Figure 4-3: Schematic of the multispectral sensor installed within the AM machine.

### 4.3.3 X-Ray Computed Tomography (XCT) of Test Parts

X-ray computed tomography (XCT) of the five discs was carried out on a GE Phoenix v|tome|x m system. Components were scanned using a beam voltage of 170 kV and a voxel resolution of 0.015 mm. Image processing techniques were used to extract three quantities for each layer: (i) the average proportions of pores, (ii) the number of pores, and (iii) the average distance between pores (in terms of their pixel proximity). These three metrics were then aggregated into a metric termed as normalized porosity level ( $\mu$ ), described subsequently in this section.

Porosity information was extracted using three image processing steps to detect the boundary of each pore and then label its interior:

1. Detecting and cropping around the boundary of each disc to eliminate XCT artifacts.
2. Adjusting the brightness and contrast of the XCT slice to make the pores differentiable from the background. This was done heuristically for a few layers of a particular disc, and then the parameters were maintained constant for the rest of the layers for that disc.
3. Detecting all the edges related to a pore using the Canny edge detection algorithm [144] with manually-adjusted threshold parameters. However, the pore edges obtained from the Canny approach were not continuous (because there were subtle differences between the contrast of the layers). Hence, to ensure that the edges of the pore formed a contiguous boundary, an iterative image dilation technique was used. Lastly, the interior of each pore was labeled with a (binary) pixel value of one.

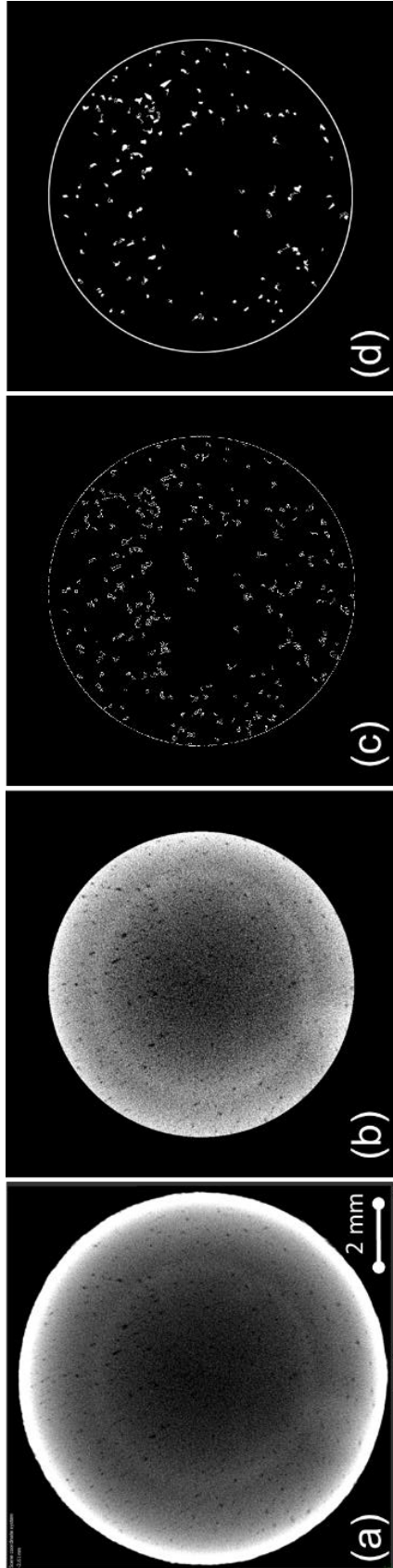


Figure 4-4: Image processing steps to extract the porosity from XCT slices. The XCT is shown for layer 18 Disc C with (a) the original unprocessed XCT slice, (b) the cropped image after image enhancement, (c) the detected edges located around the pores and disc cross section in a binary format, and (d) the dilated edges that are filled with pixel values equal to 1 to construct the whole pores in a layer of the disc.

Figure 4-4 illustrates the implementation of image processing steps. On comparing Figure 4-4(c) and (d), it is noted that some of the smaller pores whose boundaries could not be closed in Step 4, were missed. However, this loss of information was found to be consistent across all discs. From the binary image from Figure 4-4(d), the following metrics is extracted to characterize porosity:

- i. The proportion of an area in a layer affected by the porosity ( $\rho_1$ ),
- ii. Frequency of occurrence, i.e., the number of discrete pores in a layer ( $\rho_2$ ),
- iii. The average distance between a pair of pores ( $\rho_3$ ).
- iv. The combination of above three metrics into a single metric, called the normalized porosity level ( $\mu$ ).

These porosity metrics, and the approach to obtain them are detailed hereunder.

*Proportion of area covered by pores in a layer* ( $\rho_1$ , unitless) defines the area occupied by the pores as a ratio of the pixels related to the pores in proportion to all the pixels in the image. This was calculated by summing the pixels with value 1 in a binary image.

If the binary image is represented as a matrix  $I$  with  $M$  rows and  $N$  columns, with each element (pixel)  $p_{i,j}$  then,

$$\rho_1 = \frac{\text{Pixels related to the pores}}{\text{All pixels in the image}} = \frac{\sum_{i=1}^{i=M} \sum_{j=1}^{j=N} p_{i,j}}{M \times N} \quad (4-1)$$

*Number of the pores in a layer* ( $\rho_2$ , unitless) is defined as the distinctive number of pores in a layer. This was found by first estimating the coordinates of the centroid of each pore in the layer, and then counting the number of distinct centroids. If the centroids are marked as  $c_1 \dots c_k$ , then  $\rho_2$  is given as,

$$\rho_2 = |c_i|_0 \quad \forall i; \quad i = \{1 \dots k\} \quad (4-2)$$

*Average distance between pores in a layer* ( $\rho_3$ , pixels) is the mean pairwise distances between the centroid of the pores. The numerator in Eq. (3) is the sum of the Euclidean distance between pores, and the denominator is the number of pairs of pores.

$$\rho_3 = \frac{\sum_{\forall i,j} \|c_i - c_j\|_2}{\binom{\rho_2}{2}} [\text{pixels}] \quad \forall i, j; \quad i, j = \{1 \dots k\} \quad (4-3)$$

*Normalized porosity level* ( $\mu$ , unitless) combines  $\rho_1$ ,  $\rho_2$ , and  $\rho_3$  into a dimensionless number ( $\mu$ ) between 0 and 1. It is assumed that  $\rho_1$ ,  $\rho_2$ , and  $\rho_3$  were all non-zero. Accordingly,  $\mu$  was obtained in two steps. First, in Eq. (4-4) the porosity measure  $\rho_4$  was obtained for each layer. Subsequently, the  $\rho_4$  value was normalized in Eq. (4-5) to obtain a value between 0 and 1.

$$\rho_4 = \frac{\rho_1 \times M \times N [\text{pixels}^2]}{\rho_2 \times \rho_3 [\text{pixels}]} = \frac{\sum_{i=1}^{i=M} \sum_{j=1}^{j=N} p_{i,j}}{\rho_2 \times \rho_3} [\text{pixels}] \quad (4-4)$$

$$\mu = \frac{\rho_4 - \min(\rho_4)}{\max(\rho_4)} \quad (4-5)$$

The physical meaning of  $\mu$  can be explained as follows. The area occupied by pores in a layer is represented in  $\rho_1$ , hence a small  $\rho_1$  is desirable for a fully dense component.

However,  $\rho_1$  does not capture how many pores account for this area. For example, one big pore of a certain area  $A$  may have a more deleterious effect on the physical properties of the part than multiple pores which add up to the same area  $A$  (i.e., the smaller the ratio  $\rho_1/\rho_2$  the better[145]). Next, having pores farther away from each other is more desirable than having two pores closer together. Hence, the average distance between the pores ( $\rho_3$ ) should also be considered with the physical contention that the severity of porosity is inversely proportional to  $\rho_3$ .

Accordingly, in the combined measure  $\rho_4$  of Eq. (4-4),  $\rho_1$  went to the numerator, whereas,  $\rho_2$  and  $\rho_3$  were in the denominator. Subsequently,  $\rho_4$  was normalized to  $\mu$  to obtain a value between 0 and 1 for each test part (disc), with a value nearer to 0 representing an ideal outcome. It is noted that if  $\rho_1$  was zero for a layer, such as in Disc D the number  $\mu$  was forced to zero.

In Sec. 4.5.3,  $\mu$  is used as the response (output) to be predicted for each layer as a function of graph-theoretic Laplacian eigenvectors and eigenvalues extracted from the multispectral sensor data. The procedure to derive these graph-theoretic process signatures is described in the forthcoming section, Sec. 4.4.

#### 4.4 Proposed Methodology

There are four steps in the approach used to extract the Laplacian eigenspectra of line-to-continuum signatures. Each step is explained in detail herewith. The mathematical underpinnings of the proposed methodology have been addressed in the authors' previous work; some of it have been restated here for the sake of continuity [25]. Detailed mathematical justifications for the approach are available in Rao's previous work [25, 112].

The novelty of this work can be described as the reconstruction of sensor data into an undirected weighted graph to extract the Laplacian eigenspectra for each layer and relate these process signatures to the level of porosity. In previous works the sensor signatures were mainly correlated with defects due to overhang and contamination in LPBF [13, 25]

*Step 1: Transforming the one-dimensional multi-spectral signal into a graph.*

In this step, the aim was to convert the one-dimensional line-to-continuum ratio signatures into a weighted, undirected graph  $G(V, E, W)$ , where  $V$ ,  $E$  and  $W$  are the vertices, edges, and weight between the edges of a network graph, respectively. To begin with the graph conversion process, it was necessary to reshape the signal as a matrix that would be used as an input for the approach. To realize this aim, the multi-spectral signal related to each layer of the disc, which was comprised of approximately 56,000 to 157,000 data points, was represented as a signal matrix ( $X_l$ ). Where  $l$  is the layer number in this work, line-to-continuum data was available for 110 layers for each disc (i.e.,  $l = 1, 2, \dots, 110$ ) indexed in terms of the laser scan coordinates.

The total number of data points per layer for each disc is detailed in Table 4-2: Approximate number of data points available per layer.

for a particular disc, and the corresponding number of rows ( $N$ ) for each layer ( $d = 50$ ). The number of data points obtained per layer was contingent on the scan velocity and hatch spacing – a higher scan speed and hatch spacing implied less time spent melting a layer. Hence the fewest data points were sampled per layer of Disc C, for example, which had the highest hatch spacing. The key aspect of this step is to populate the signal matrix ( $\mathbf{X}_l$ ).

Accordingly, the line-to-continuum emission signal for each layer was first separated into equal lengths corresponding to 50 data points which translated to approximately 1 mm and 1.25 mm of scan length for the lowest (1.875 m/sec) and highest scan velocity (2.5 m/sec), respectively. The approach is illustrated in Figure 4-5. Based on extensive offline studies not reported in this work, the length of 50 data points was found to be the smallest possible window wherein the approach was found to be viable. This allowed the signal to be converted into a matrix with a fixed column width, i.e., each row of the data was a 50 data point long signal segment of a layer ( $l$ ).

Table 4-2: Approximate number of data points available per layer.  
for a particular disc, and the corresponding number of rows ( $N$ ) for each layer ( $d = 50$ ).

Discs	Average number of data points per layer	Number of rows ( $N$ ) in the signal matrix $\mathbf{X}_l$
Disc A	157000	3140
Disc B	76000	1620
Disc C	56000	1120
Disc D	113000	2260

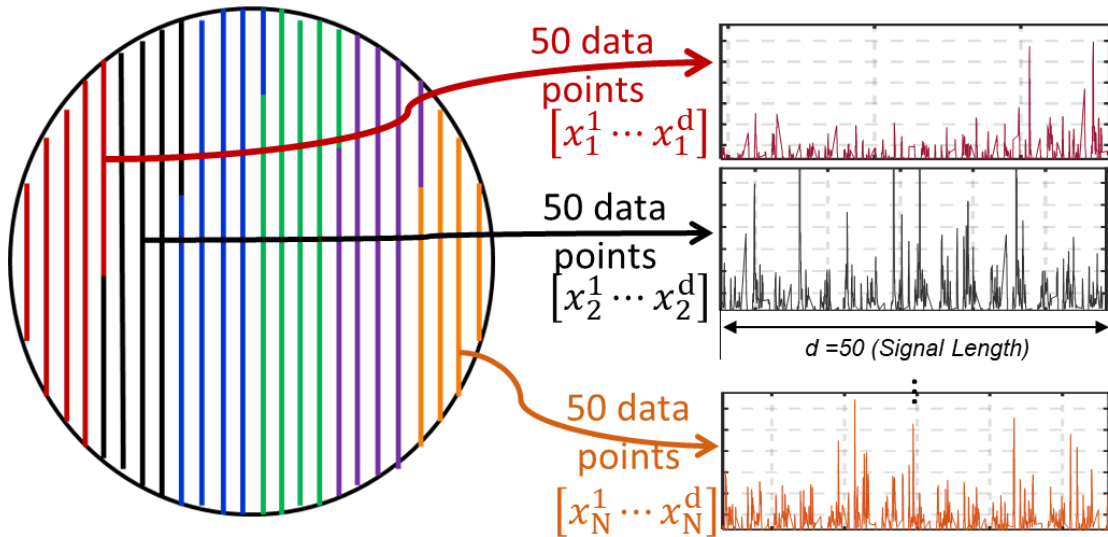


Figure 4-5: Illustration of the approach taken to window the signal.

Shown here is an example of windowing the photodetector signal in each layer into 50 data point long segments. The diagram is not to scale.

In other words, each 50-point long segment populated a separate row of  $\mathbf{X}_l$ . Hence the matrix  $\mathbf{X}_l$  had  $N$  rows and  $d$  ( $=50$ ) columns. The value of  $N$ , which was the number of 50-point segments in the layers, varied roughly between 3100 to 1100 and, as mentioned previously, was inversely proportional to the laser velocity and hatch spacing (Table 4-2: Approximate number of data points available per layer.

for a particular disc, and the corresponding number of rows ( $N$ ) for each layer ( $d = 50$ ).). Consequently, the signal matrix ( $\mathbf{X}_l$ ) was setup for each layer as follows,

$$\mathbf{X}_l = \begin{bmatrix} x_1^1 & \cdots & x_1^d \\ \vdots & \ddots & \vdots \\ x_N^1 & \cdots & x_N^d \end{bmatrix} \forall l = \{l = 1, 2, \dots, L = 110\}, \text{ and } d = 50. \quad (4-6)$$

Next, a pairwise comparison was made between each of the rows of the matrix  $\mathbf{X}_l$ . Such a pairwise comparison implies that the change in the signal across a layer is tracked. In graph-theoretic parlance, each of the  $N$  rows in  $\mathbf{X}_l$  became a node or vertex in the graph. The weight of an edge connecting one node ( $q$ ) to another ( $r$ ) in the graph was the pairwise

distance between them. The distance  $w_{qr}$  was computed using a normed kernel function  $\Omega$  per Eq. (2-3). The kernel function could relate to a similarity measure, such as a Euclidean distance, between the set of data points in row  $r$  and  $q$  of the matrix  $\mathbf{X}_l$ . Following this reasoning if  $\mathbf{x}^q$  and  $\mathbf{x}^r$  are the  $q^{\text{th}}$  and  $r^{\text{th}}$  row vectors in  $\mathbf{X}_l$ , the similarity distance between them ( $w_{qr}$ ) can be mathematically represented as,

$$w_{qr} = \Omega(\mathbf{x}^q, \mathbf{x}^r) \forall q, r \in (1 \cdots k). \quad (4-7)$$

Among different types of kernel functions  $\Omega$ , such as the radial basis or Euclidean, in this work the Mahalanobis kernel shown in Eq. (2-5) is used, where  $\mathbf{\Sigma}$  is the covariance matrix of  $\mathbf{X}_l$ . The Mahalanobis kernel was chosen because it tends to normalize the data with respect to its covariance.

$$w_{qr} = (\mathbf{x}^q - \mathbf{x}^r)\mathbf{\Sigma}^{-1}(\mathbf{x}^q - \mathbf{x}^r) \quad (4-8)$$

Because, there are  $N$  rows in the matrix  $\mathbf{X}_l$ , a weighted undirected graph with  $N$  nodes and  $\frac{N(N-1)}{2}$  edges is obtained. Once the pairwise distances  $w_{qr}$  are computed, they can be compacted into a *similarity matrix*. The similarity matrix  $\mathbf{S}_l^{N \times N} = [w_{qr}]$  which is a symmetric matrix, represents a weighted and undirected graph  $G$ . Hence,  $\mathbf{S}_l$  is the matrix representation of the signal  $\mathbf{X}_l$  in terms of the graph.

Each row (or column) of  $\mathbf{S}_l$  is a node in the graph. Each element is the weight of the edge connecting two nodes indexed by its row and column. For instance, the element  $\mathbf{S}_l(i, j) = \mathbf{S}_l(j, i)$  represents the weight of the edge connecting between node  $i$  and node  $j$ . In other words, the graph  $G(V, E, W)$  is a lower dimensional, specifically a planar 2D,

graph representation of the relationship between each segment of the signal  $\mathbf{X}_l$  in terms of the similarity matrix  $\mathbf{S}_l$ .

*Step 2: Calculating eigenspectrum (topological information) of the graph*

This step aimed to extract topological information from the graph  $G$  embedded in the eigenvectors and eigenvalues of its Laplacian matrix. After converting the signal into a matrix  $\mathbf{X}_l$  as described in Step 1 and representing it as a planar graph  $G_l$  in terms of the similarity matrix  $\mathbf{S}_l$ , next the Laplacian eigenspectrum including eigenvalues ( $\mathbf{\Lambda}_l$ ) and eigenvectors ( $\mathbf{V}_l$ ) is calculated. These so-called *spectral features* were subsequently used to predict the degree of porosity in a layer.

The procedure to obtain  $\mathbf{\Lambda}_l$  and  $\mathbf{V}_l$  is encapsulated in Eq. (2-7) – Eq. (2-11). The normalized Laplacian matrix was first calculated in Eq. (2-7) – Eq. (2-9) based on the similarity matrix ( $\mathbf{S}_l$ ) and degree matrix ( $\mathbf{D}_l$ ), where the degree matrix Eq. (4-10) is the sum of each row in the similarity matrix. To be more specific, the degree of each node in the graph is described as the sum of the weight of the edges that are incident upon a node. In Eq. (2-7),  $q$  represents a node on the graph.

$$d_q = \sum_{r=1}^N w_{qr} \quad \forall q = \{1 \dots N\} \quad (4-9)$$

$$\mathbf{D}_l \stackrel{\text{def}}{=} \text{diag}(d_1, \dots, d_N). \quad (4-10)$$

Having the degree matrix, the normalized Laplacian  $\mathcal{L}$  of the graph  $G$  can be defined as,

$$\mathcal{L}_l \stackrel{\text{def}}{=} \mathbf{D}_l^{-\frac{1}{2}} \times (\mathbf{D}_l - \mathbf{S}_l) \times \mathbf{D}_l^{-\frac{1}{2}}, \quad (4-11)$$

where,  $\mathbf{D}_l^{-\frac{1}{2}} = \text{diag}\left(\frac{1}{\sqrt{d_1}}, \dots, \frac{1}{\sqrt{d_N}}\right)$ .

Accordingly, the eigenspectrum of  $\mathcal{L}$  is computed as,

$$\mathcal{L}_l \mathbf{V}_l = \mathbf{\Lambda}_l \mathbf{V}_l. \quad (4-12)$$

And the graph Laplacian eigenvalues ( $\mathbf{\Lambda}_l$ ) and eigenvectors ( $\mathbf{V}_l$ ) can be described as follows,

$$\begin{aligned} \mathbf{\Lambda}_l &= [\lambda_{l,1}; \lambda_{l,2}; \dots; \lambda_{l,N}] \\ \mathbf{V}_l &= [[\mathbf{v}_{l,1}]; [\mathbf{v}_{l,2}]; \dots; [\mathbf{v}_{l,N}]] \end{aligned} \quad (4-13)$$

where,  $\mathbf{V}_l$  is composed of  $N$  individual eigenvectors  $\mathbf{v}_{l,(.)}$ , and  $\mathbf{\Lambda}_l$  contains the corresponding number of eigenvalues  $\lambda_{l,(.)}$ .

A property of the Laplacian eigenvalues and eigenvectors that is central to this work is that all the eigenvalues are real and non-negative, and the eigenvectors are orthogonal to each other (because the matrix  $\mathcal{L}_l$  is symmetric and positive semi-definite). These properties are encapsulated in Eq. (4-14), with the additional caveat that the first eigenvector is a zero vector ( $\mathbf{v}_{l,1} = \vec{0}$ ) and the first eigenvalue of  $\mathcal{L}_l$  is zero ( $\lambda_{l,1} = 0$ ).

$$\begin{aligned} \mathbf{v}_{l,2} \perp \mathbf{v}_{l,3} \perp \mathbf{v}_{l,i} \cdots \perp \mathbf{v}_{l,N}, &\Rightarrow \langle \mathbf{v}_{l,i}, \mathbf{v}_{l,j} \rangle = 0 \quad \forall i \neq j, \\ \text{and } \langle \mathbf{v}_{l,i}, \mathbf{v}_{l,j} \rangle &= 1 \quad \forall i = j, \text{ noting } \mathbf{v}_{l,1} = \vec{0} \\ \lambda_{l,(.)} &\geq 0, \text{ and } \lambda_{l,1} = 0 \end{aligned} \quad (4-14)$$

*Step 3: Constructing the signal basis to obtain graph Fourier coefficients*

In this step, the eigenvectors  $\mathbf{V}_l$  were used to transform a raw line-to-continuum signal into so-called graph Fourier coefficients. To realize this aim, a universal eigenvector basis space must be constructed. The rationale for forming such a universal eigenvector basis space is as follows. The signal ( $\mathbf{X}_l$ ) from a nominally defect-free disc (Disc D) are presumably statistically distinctive compared to the signals obtained from other test parts

(Discs A, B, and C). However, due to the presence of noise for even a nominally defect-free disc the signal patterns will vary across layers, and hence the eigenvectors  $\mathbf{V}_l$  will also differ from one layer to the next.

To overcome this challenge, a universal basis is framed, ( $\mathbf{V}_{basis}$ ) as a time-weighted average of the eigenvectors across layers for Disc D, which represents a prototype/ideal eigenvector. The procedure for obtaining the  $\mathbf{V}_{basis}$  is a layer-wise simple update schema. It was started with the eigenvector of the first layer ( $\mathbf{V}_{l=1}$ ) of Disc D. This would be continually updated by a small portion ( $\Delta < 0.01$ ) of the difference between the eigenvectors for the next consecutive layers for Disc D, and so on.

$$\begin{aligned} \mathbf{v}_{l+1} &= \mathbf{v}_l + \Delta(\mathbf{v}_{l+1,i} - \mathbf{v}_{l,i}), \forall l \in \{1 \dots L = 110\}, i \in \{1 \dots N\} \\ \mathbf{V}_{basis} &= \mathbf{V}_L \end{aligned} \quad (4-15)$$

We defined the spectral graph transform  $\mathbf{C}$  using Eq. (2-15) which is analogous to the discrete Fourier transform as follows, where  $\mathbf{X}_l$  is a sensor signal for a layer  $l$ , which is an  $N$  data point long column vector [107].

$$\mathbf{C} = [(\mathbf{X}_l)^T (\mathbf{V}_{basis})] \quad (4-16)$$

As the  $\mathbf{V}_{basis}$  is fixed, using the above inner product through all the layers ( $\mathbf{X}_l$ ) resulted in the graph coefficient matrix  $\mathbf{C}$ . The graph Fourier transform ( $\mathbf{C}$ ) in this study is a  $1 \times N$  vector that results from the dot product of the  $1 \times N$  line-to-continuum signals for each layer ( $\mathbf{X}_l^T$ ) with the  $N \times N$  dimensional eigenvector basis ( $\mathbf{V}_{basis}$ ) [105-107, 134, 135]. However, to reduce the computational burden, only the first 5 to 10 non-zero values of the  $\mathbf{C}$  are used. This was verified through principal component analysis; it is found that

more than 85% of the variation in the dataset were captured within the first ten eigenvectors in  $\mathcal{V}_{basis}$ .

*Step 4: Predicting the porosity properties using spectral graph features*

The aim of this step was to predict the level of porosity, which was expressed in terms of the normalized porosity level ( $\mu$ ), as a function of the graph Fourier coefficients ( $\mathbf{C}$ ) and eigenvalues ( $\mathbf{\Lambda}_l$ ) derived from the in-process, line-to-continuum ratio measurements. This mapping of sensor signatures ( $\mathbf{C}$ ) to normalized porosity ( $\mu$ ) was done using machine learning approaches, which are described in detail in the forthcoming section, Sec. 4.

We have used the following two-fold strategy for predicting the porosity in a disc based on the line-to-continuum emission ratio obtained from the multispectral sensor data.

- 1) Classifying or binning the normalized porosity level ( $\mu$ ) into discrete categories.
- 2) Estimating the value of the normalized porosity level ( $\mu$ ).

There are two types of graph-theoretic sensor signatures that can be extracted from the line-to-continuum signals and used for either classification or estimation. The first method relates to the Laplacian eigenvalues ( $\mathbf{\Lambda}_l$ ), which will be used as inputs to a machine learning model to ascertain the normalized porosity level ( $\mu$ ) for a particular layer. This approach requires extracting the Laplacian eigenvalues from the line-to-continuum ratio signals for each layer of each disc, and subsequently, training a supervised machine learning model to predict a particular class (or label) of normalized porosity level ( $\mu$ ) which is obtained *a priori* from the offline analysis of the XCT images as described in Sec. 4.3.3.

Consequently, when a new sensor signal dataset for a layer ( $\mathbf{X}_l$ ) was acquired, the Laplacian eigenvalues ( $\mathbf{\Lambda}_l$ ) were extracted from it, and subsequently used as an input to the

already trained machine learning model to predict the porosity level ( $\mu$ ). The advantage of this approach is that the steps to obtain  $\Lambda_l$  from the signal for each layer are relatively straightforward in terms of the mathematics – following Eq. (4-6) – Eq. (4-13). The drawback is that the signal from every layer must be subjected to the analysis for extracting the Laplacian eigenvalues. This takes a relatively long computational time, because, obtaining the Laplacian eigenvalues requires first converting the signal into a planar graph, and then solving the cumbersome eigen decomposition problem for a large matrix (Eq. (2-11)).

The second method was more complex to train initially but was more tractable to implement for real-time monitoring and relied on the graph Fourier transform ( $\mathbf{C}$ ) (Eq. (2-15)). Herein the eigenvectors basis ( $\mathbf{V}_{basis}$ ) were extracted from the nominally defect-free part, which in our case was Disc D. The eigenvectors ( $\mathbf{V}_{basis}$ ) served as a basis or projection space for the sensor data. The rationale is that when a set of data belonging to the nominal defect-free condition, such as Disc D, is projected onto this space, in terms of the graph Fourier transform coefficients  $\mathbf{C}$ , it will cluster closely in space with the coefficients from previous nominally defect-free layers.

Conversely, if the signal belongs to a pore-afflicted layer, its coefficients will cluster away from the coefficients belonging to a nominally porosity-free layer. The advantage of this approach is that, instead of solving the eigen decomposition problem for each layer of the signal, as in the previous approach with the Laplacian eigenvalues ( $\Lambda_l$ ), the sensor data is transformed into a spectral graph space on obtaining a simple inner product multiplication (dot product) of the Laplacian eigenvector with the signal of equal length as described in Eq. (2-15).

*Approach for classifying the normalized porosity level into discrete categories*

The aim herein is to classify the porosity level in terms of the normalized porosity metric ( $\mu$ ) given the multispectral line-to-continuum signatures. The procedure to obtain  $\mu$  was described previously in Sec. 4.3.3;  $\mu$  was obtained for each layer of the 110 layers from the offline XCT scans. Next, the normalized porosity level in a layer was divided into different classes. In the first instance, the porosity level was split into two classes (high and low), and in the second, the porosity level was grouped into three classes. These class groupings or labels were made per a threshold limit value of the porosity level  $\mu$  specified, based on all the XCT data available from the experiment.

In making the choice for the threshold value the distribution of the porosity level ( $\mu$ ) values is considered so that a situation in which a particular class was populated with only a few representative porosity levels  $\mu$  could be avoided. This strategy entailed that each of the classes had at least 100 values of  $\mu$  associated with it, and thus minimized the possibility of overfitting the data with machine learning models.

Three rudimentary machine learning classification algorithms, namely, Support Vector Machine (SVM), K-Nearest Neighbor (KNN), and Decision Tree (Tree) were used to classify the level of porosity. The fidelity of these algorithms was assessed based on the F-score measure, which is a combination of both Type I (false error) and Type II (failing to detect) statistical errors. The results based on extensive offline studies are reported to optimize the parameters for these algorithms.

The input features to the algorithms selected are one of the following three types, which correspond to 440 deposited layers (4 printed discs with 110 layers for each disc).

- Input Type 1: First ten non-zero Laplacian eigenvalues ( $\Lambda_l$ ), which were obtained as described previously in Sec. 4.1, Eq. (4-13).
- Input Type 2: The graph Fourier coefficients ( $\mathbf{C}$ ) obtained from the first ten non-zero Laplacian eigenvectors ( $\mathbf{V}_{basis}$ ) shown in Sec. 4.1, Eq. (2-15).
- Input Type 3: The five statistical features extracted from the line-to-continuum ratio, namely, the mean, standard deviation, range, skewness, kurtosis, and interquartile range.

Each feature set was finally subjected to principal component analysis (PCA), which is a statistical procedure to further compress the dimension of the data. This PCA-based dimension reduction transformed the features into orthogonal components. Further, to ensure equitable comparison between the input features, the number of principal components chosen corresponded to those capturing at least 85% of the variation in the data.

#### *Estimating the value of the normalized porosity level*

Given that the ability to distinguish between different porosity levels was found to be 80% at best for a three-level scenario, a simple (shallow) feed-forward neural network is implemented with two hidden layers and five neurons in each hidden layer designed to predict the exact porosity value ( $\mu$ ). In this neural network, sigmoid activation functions were used in the hidden layers, and a linear activation function was used in the output layer. The backpropagation algorithm, via Levenberg-Marquardt optimization, was implemented

to minimize the sum of squared errors between the predicted ( $\hat{\mu}_l$ ) and observed ( $\mu_l$ ) normalized porosity level over one layer [146].

To evaluate the accuracy of the prediction, two measurements are used, namely, symmetric mean absolute percent error (SMAPE) and normalized root mean square deviation (NRMSD), defined in Eq. (4-17). Both these measures are based on the difference between the porosity values ( $\mu_l$ ) extracted for a layer  $l \forall l \in \{1 \dots L = 110\}$  from the offline XCT scans and the predicted porosity values ( $\hat{\mu}_l$ ) for that layer obtained using the neural network.

$$SMAPE = \frac{1}{L} \sum_{l=1}^{l=L} \frac{|\mu_l - \hat{\mu}_l|}{(|\mu_l| + |\hat{\mu}_l|)/2}; \quad NRMSD = \frac{\sqrt{\sum_{l=1}^{l=L} (\mu_l - \hat{\mu}_l)^2}}{\sqrt{\sum_{l=1}^{l=L} \hat{\mu}_l}} \quad (4-17)$$

## 4.5 Results and Discussion

### 4.5.1 Quantifying Porosity from X-Ray Computed Tomography (XCT)

The size and distribution of pores varied across the measured discs as evident in Figure 4-6, which shows the results from applying the procedure for extracting the pores for each of the discs for layer 14. Measurements of the mean percentage of area covered by pores ( $\rho_1$ ), the mean number of pores ( $\rho_2$ ), the mean distance between pores ( $\rho_3$ ), and the normalized porosity ( $\mu$ ) are provided in Table 4-3. Distributions of each porosity metric across each disc is also visualized in Figure 4-7. Disc D did not contain any porosity and is not shown.

From Figure 4-7 it is further apparent that the statistical distribution of each porosity metrics differed from disc to disc. Disc A appears to have the severest level of porosity

with the highest mean porosity proportion of pores per layer ( $\rho_1$ ), highest mean number of pores per layer ( $\rho_2$ ), smallest average distance between pores ( $\rho_3$ ), and consequently, the largest mean normalized porosity level ( $\mu$ ). In ranking terms, apart from Disc D, the samples in terms of *descending* level of pore severity are: Disc A, followed by Disc B and Disc C.

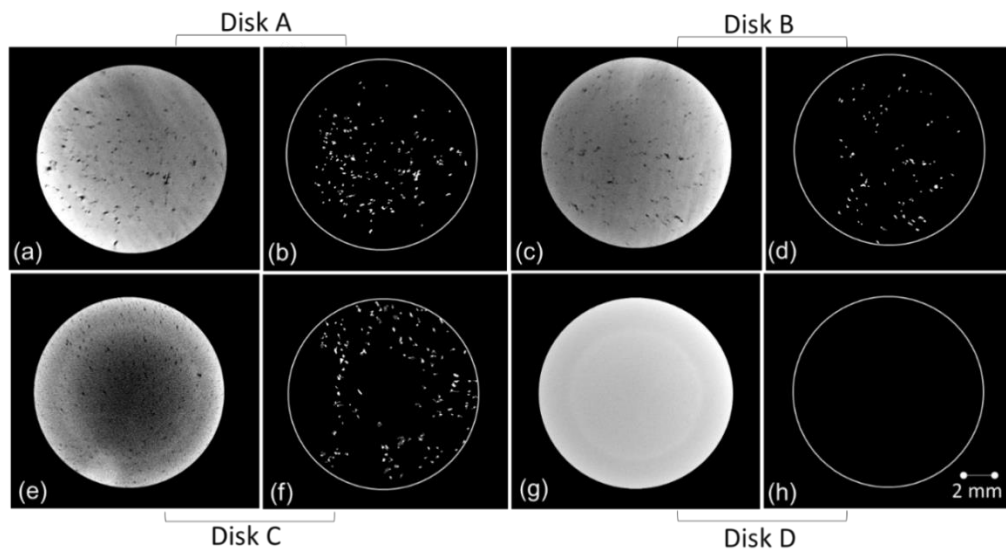


Figure 4-6: The pore extraction procedure as applied to the XCT. Shown here is the result of the pore extraction procedure for layer 18 for Disc A through Disc D. The proportion of pores, their number, and spatial distribution are observed to vary across the discs.

Table 4-3: The mean value of the three metrics  $\rho_1$ ,  $\rho_2$ , and  $\rho_3$ . The data shown is from applying the pore extraction procedure applied to over 110 layers of the three discs extracted from their XCT scans. The number in the parenthesis is the standard deviation.

Disc	$\rho_1$ Mean percentage of area covered by pores in each layer.	$\rho_2$ Mean number of pores in each layer (rounded)	$\rho_3$ Mean distance in pixels between pores in each layer	$\mu$ Mean normalized porosity measure in each layer.
Disc A	1.8% (0.828%)	102 (48)	223 (15.7)	0.64 (0.076)
Disc B	1.3% (0.997%)	78 (52)	233 (23.3)	0.57 (0.080)
Disc C	0.7% (0.810%)	40 (40)	263 (34.6)	0.57 (0.097)

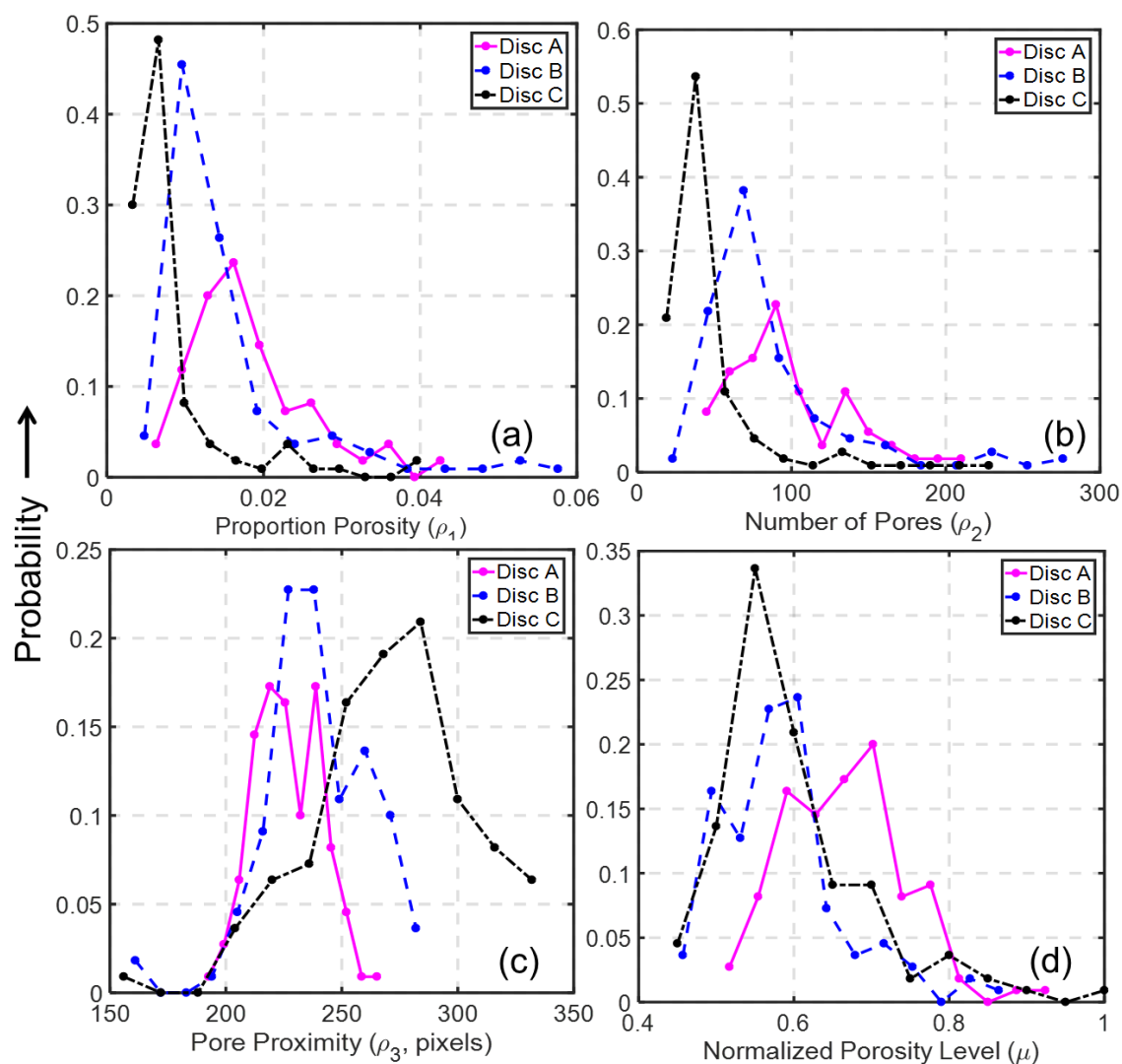


Figure 4-7: The probability mass functions for three different porosity metrics.

#### 4.5.2 Visualization of Sensor Data

The probability distribution of the line-to-continuum ratio for 50,000 randomly selected data points from the same layer (60) for the four discs A through D are overlaid in Figure 4-8, from which it is evident that there were apparent differences in the distribution of the line-to-continuum ratios for the four discs.

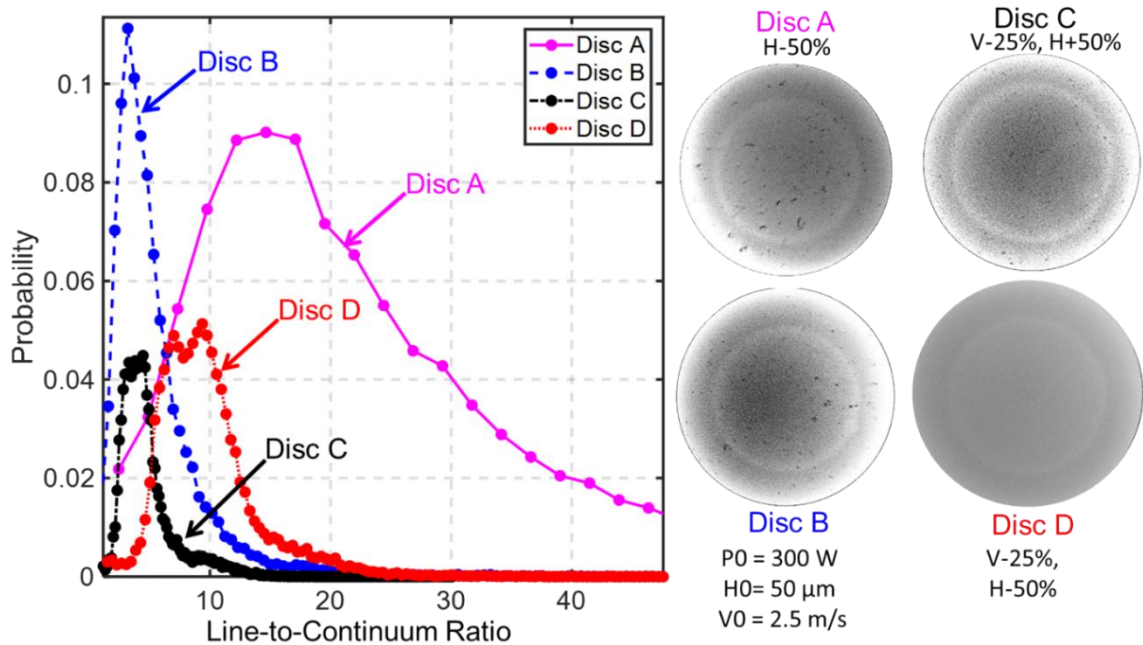


Figure 4-8: The distribution of 50,000 randomly selected measurements of the line-to-continuum ratio for one layer (layer 60) of Disc A through D.

#### 4.5.3 Classifying the Severity of Pores into Discrete Levels

We implemented three algorithms each with three types of input features for evaluating the proposed approach for a total of 9 treatment conditions, in the parlance of design of experiments. Finally, the statistical performance of the algorithm in terms of the F-score was evaluated through a 5-fold cross validation technique. The training and testing procedure used is as follows,

- *Training.* The dataset was split randomly into 5 tranches with equal number of data points per tranche ( $440 \text{ layers}/5 = 88 \text{ data points per tranche}$ ) in each part. Each of the four algorithms was first trained for each type of input using data from one tranche (88 data points).
- *Testing.* The algorithms were tested on the data from the rest of the tranches ( $4 \times 88 = 352 \text{ data points}$ ). This process was repeated 5 times, and then the average prediction fidelity in terms of the F-score over these 5 repetitions was reported.

For the two-class classification case, since  $\mu$  ranged between  $[0,1]$ , the threshold is set at 0.5. In other words, if the normalized porosity level ( $\mu$ ) was less than or equal to 0.5 for a layer it was considered as an acceptable porosity level, and conversely, any layer having  $\mu$  over 0.5 was labeled as falling within a class representing an unacceptably high level of porosity.

In a similar vein, for the three-class problem, the labeling procedure is as follows: if  $\mu = 0$  then the porosity-class was labeled as low-level, if  $0 < \mu < 0.6$  as medium-level, and  $0.6 \leq \mu$  as high-level. It is reiterated that there were several means to partition the porosity level into classes; the volume of data available determines how finely the class divisions can be made. It is ensured that no class had less than 100 values of  $\mu$  to avoid overfitting. Table 4-4 represents the accuracy of the predictions for a two-level porosity (in terms of F-score) among three different methodologies. The confusion matrix related to the most accurate F-score is shown in Table 4-5. The following inferences can be drawn based on the results depicted in Table 4-4 and Table 4-5.

For the two-level classification case, the three input types provided appreciably good results. Using the Laplacian eigenvectors for the input type, however, led to the highest classification accuracy. Furthermore, examining the confusion matrix revealed that the Type II error rate, i.e., incorrectly concluding that a layer has a low porosity level when it truly belongs to a high-porosity class, was only 1 in 287 layers. However, the Type I statistical error, i.e., falsely concluding that the layers have high porosity, was approximately 1 in 30 layers. The reason for such a high-level of Type I error can be explained based on the physics of the process. While a pore may be created in a layer, and promptly detected from the multispectral line-to-continuum emissions; subsequent layers

are liable to re-melt the unfused particles in previous layers and thereby eliminate porosity. This re-melting phenomena in LPBF has been mathematically simulated by researchers at Lawrence Livermore National Laboratories, namely, by Khairallah and King, *et al.*[136].

In the more challenging three-level classification case, there was a more marked difference in the three input types. Using the Laplacian eigenvectors resulted in a classification accuracy approaching 80%, whereas, the other two input features led to an F-score in the 60% to 65% region. Examining the F-score from the Laplacian eigenvectors, in terms of the confusion matrix shown in Table 4-5, indicates that, if indeed a layer had a level of porosity, it was not detected in only 2 out of 330 cases – 1 in 196 layers belonging to the medium-level porosity class were grouped in the low porosity class, while 1 in 134 layers for the high-level porosity class were wrongly classified as belonging to the low-porosity level. However, the concern with the confusion matrix is in the last row of Table 4-5 where 59 out of a total 134 layers that belong to the high-level porosity case are wrongly categorized as belonging to the medium-level porosity. This high level of classification error is most likely due to the hard threshold that was used to separate the data into three classes. Such a large error needs to be overcome, for the proposed approach to be successful in practice. An approach to overcome the limited success of the three-level classification is to use a continuous boundary condition, instead of a hard threshold. This would also allow estimation of the exact porosity level. However, this entails sacrificing the tractability of classification to a more sophisticated data modeling technique, such as a neural network.

Table 4-4: Performance of two proposed algorithms in comparison with one that uses statistical features for predicting the normalized porosity level ( $\mu$ ).

In this table layers with normalized porosity level  $\mu \leq 0.5$  were labeled as acceptable porosity whereas  $\mu > 0.5$  were considered as unacceptable porosity.

F-score results from classifying the porosity levels into two classes. $\mu \leq 0.5$ as acceptable-level, $\mu > 0.5$ as unacceptable-level.			
Machine Learning Algorithm ↓	F-Score (%)		
	Input Type 1 (Laplacian eigenvalues)	Input Type 2 (Laplacian eigenvectors)	Input Type 3 (Statistical features)
KNN	88 (1.3)	93 (1.1)	83 (1.0)
SVM	88 (1.7)	93 (0.4)	83 (0.8)
Tree	87 (1.1)	92 (1.4)	80 (0.3)
Classifying the porosity levels into three classes $\mu = 0$ as low-level, $0 < \mu < 0.6$ as medium-level, and $0.6 \leq \mu$ as high-level.			
Machine Learning Algorithm ↓	F-Score (%)		
	Input Type 1 (Laplacian eigenvalues)	Input Type 2 (Laplacian eigenvectors)	Input Type 3 (Statistical features)
KNN	65 (0.4)	79 (1.1)	62 (0.3)
SVM	65 (1.6)	79 (0.1)	63 (0.2)
Tree	66 (0.4)	79 (0.6)	65 (0.5)
Computation Time	61.3 sec	0.4 sec	5.9 seconds

Table 4-5: A representative confusion matrix for normalized porosity level ( $\mu$ ) based on the Laplacian eigenvectors (graph Fourier coefficients).

The graph Fourier coefficients were used as inputs and KNN as the classification algorithm.

Confusion matrix for classifying pore severity into two discrete levels using graph Fourier transform coefficients (Input Type 2), and KNN.			
True Class ↓	Predicted Class		
	Acceptable Porosity $\mu < 0.5$	Unacceptable Porosity $\mu \geq 0.5$	
Acceptable Porosity $\mu < 0.5$ (153 data points)	110 (out of 153)	43 (Type I error, False Alarm)	
Unacceptable Porosity $\mu \geq 0.5$ (287 data points)	1 (Type II error, Failing to detect)	286 (out of 287)	

Confusion matrix for classifying pore severity into three discrete levels using graph Fourier transform coefficients (Input Type 2), and KNN.			
True Class ↓	Predicted Class		
	Low-Level Porosity $\mu = 0$	Medium-Level Porosity $0 < \mu \leq 0.6$	High-Level Porosity $0.6 < \mu$
Low-Level Porosity $\mu = 0$ (110 data points)	109 (out of 110)	0	1
Medium-Level Porosity $0 < \mu < 0.6$ (196 data points)	1	165 (out of 196)	30
High-Level Porosity $0.6 \leq \mu$ (134 data points)	1	59	74 (out of 134)

#### 4.5.4 Estimating the Value of the Normalized Porosity Level

Figure 4-9 illustrates the observed porosity level ( $\mu$ ) overlaid with the estimated values ( $\hat{\mu}$ ) obtained using the graph Fourier coefficients as input features to the neural network. Figure 4-9 demonstrates that the porosity-level was predicted with a high-level of accuracy for all the different discs except Disc D, which had a porosity level of zero ( $\mu = 0$ ). In Disc D, roughly one third of estimated porosity levels were negative. This is because the linear activation function used in the output layer of the neural network had a non-zero bias that prevented the prediction of a constant value. This could be readily alleviated by using a positive linear activation function. The prediction accuracy is quantified in Table 4-6, Disc D is excluded due to the aforementioned reasons. Aggregating the predictions related to all discs, the NRMSD was less than 15%, and the SMAPE was roughly 10%.

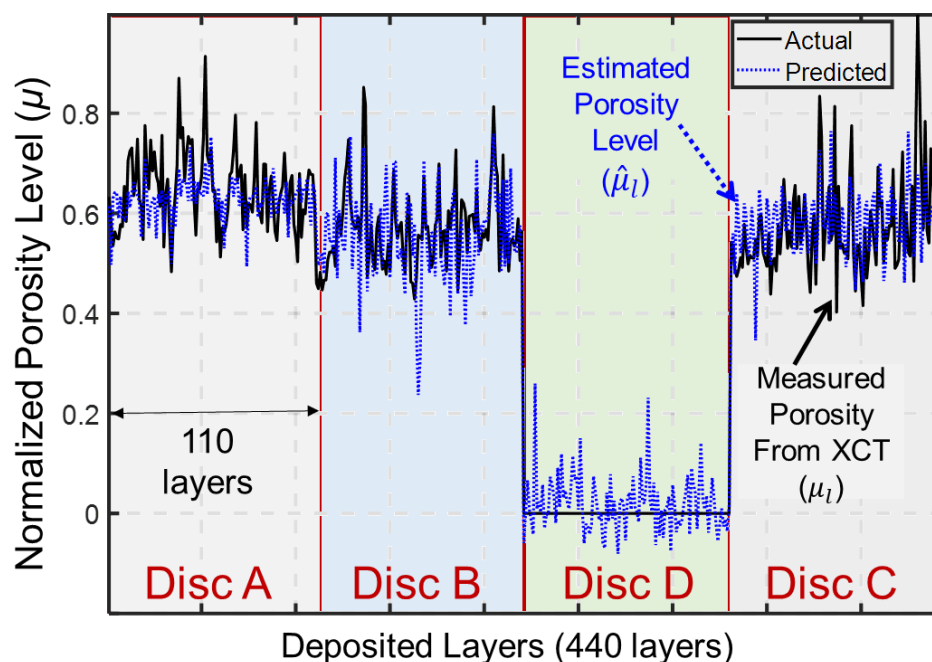


Figure 4-9: The actual vs. predicted normalized porosity levels ( $\mu$ ) along the whole dataset using the graph Fourier coefficients (method 2).

Table 4-6: The goodness of fit in exact porosity prediction using a shallow neural network with graph features as inputs.

Porosity Features	Method 1 Laplacian eigenvalues		Method 2 Laplacian eigenvectors	
	SMAPE	NRMSD	SMAPE	NRMSD
Disc A	0.08 (0.01)	0.10 (0.01)	0.09 (0.01)	0.11 (0.03)
Disc B	0.10 (0.00)	0.14 (0.00)	0.13 (0.02)	0.17 (0.02)
Disc C	0.11 (0.02)	0.14 (0.03)	0.12 (0.00)	0.16 (0.01)
Overall error	0.10 (0.01)	0.13 (0.01)	0.11 (0.00)	0.14 (0.01)

#### 4.6 Conclusions

In this work, a graph-theoretic signal processing technique is developed for detection and identification of a specific type of defect called lack-of-fusion porosity in laser powder bed fusion (LPBF) additive manufacturing of Inconel 718. The approach used output from a pair of photodetectors filtered around 520 and 530 nm, to estimate the line-to-continuum ratio of Cr I emissions. These measurements were synchronized with the position of the laser. The graph-theoretic approach proposed in this work processes the line-to-continuum ratio measurements layer-by-layer, and results in features called Laplacian eigenvalues and eigenvectors – collectively called Laplacian eigenspectra. The hypothesis is tested that the Laplacian eigenspectra derived from the line-to-continuum ratio measurements captured the patterns that are symptomatic of the occurrence and severity of pores in Inconel 718 parts.

The ability to relate graph-based features to part porosity was demonstrated in the context of machine learning techniques that use the Laplacian eigenspectra as input features to (a) classify the severity of the porosity into discrete levels, and (b) estimate the porosity level for each layer. There are two specific outcomes from this work:

- 1) The severity of pore formation is classified into two, as well as three levels via three machine learning algorithms with the Laplacian eigenspectra as input features. For the two-level classification case, the highest statistical fidelity (F-score > 90%) is obtained using graph Fourier coefficients derived from the Laplacian eigenvectors. The computational time required for the approach is less than 0.5 second. For the three-level classification study, the statistical fidelity degraded to 80%.
- 2) The Laplacian eigenspectra is also used for prediction of the porosity level, the prediction errors (normalized root-mean-square deviation, NMRSD) is approximately 10%.

### Acknowledgements

This work was partially supported by the Office of Naval Research, under Contract No. N00014-11-1-0668. This work was also partially supported by the Air Force Research Laboratory through America Makes under agreement number FA8650-12-2-7230. Any opinions, findings and conclusions or recommendations expressed in this publication are those of the authors and do not necessarily reflect the views of the Office of Naval Research, Air Force Research Laboratory, or America Makes.

## 5 Detecting Lack-of-Fusion Porosity in DED

### 5.1 Goal, Objective, and Hypothesis

The goal of this research is to detect the onset of defects such as porosity in additively manufactured metal parts using data acquired from in-process sensors. As a step towards this goal, this study focused on the analysis of in-process sensor data to detect lack-of-fusion porosity in titanium alloy (Ti-6Al-4V) parts made using a directed energy deposition (DED) metal additive manufacturing process. This avenue of research is consequential to ensure the production-scale viability of additive manufacturing (AM) processes, which despite their significant and revolutionary advantages over conventional subtractive and formative manufacturing processes, are currently impeded by their lack of part consistency and quality.

The objective is to detect the occurrence of lack-of-fusion defects in DED of titanium alloy (Ti-6Al-4V) parts such as those shown in Figure 5-1. To realize this objective, a graph-theoretic approach based on the concept of Kronecker product of graphs is developed and applied. This approach combines data from multiple in-process sensors (sensor fusion), and consequently, the signatures (features) derived from the graph-theoretic analysis are used for online detection of lack-of-fusion porosity.

The central hypothesis of this work is that the process signatures derived from the graph-theoretic analysis of sensor data are statistically significant discriminants of the lack-of-fusion porosity that manifest in Ti-6Al-4V parts produced under varying DED process conditions of laser power, powder flow rate, and hatch pattern. As a consequence of testing this hypothesis, it is shown that significantly more accurate demarcation of the porosity-level in a layer is obtained when graph-based signal features are used as independent

variables, as opposed to statistical moments-based signal features, such as signal mean and standard deviation. To test this hypothesis, the following tasks are framed:

1. Understand the effect of DED process conditions: laser power (P, Watt), powder flow rate (F, g/min), and hatch pattern (H, cross vs. parallel) on porosity. The process conditions and porosity (average pore length in a layer) are linked through offline layer-by-layer XCT measurements made on separate Ti-6Al-4V test coupons produced under ten varying P, F, and H settings.
2. Correlate the in-process sensor data obtained during the deposition of the parts in the previous task to average pore length in a layer using the concept of Kronecker product of graphs. To elaborate further, the graph Kronecker product is used to combine the signatures from two in-process sensors, namely a spectrometer and a melt pool plume imaging camera. Then, the signal patterns affiliated with different discrete levels of average pore length is learnt in the form of a dictionary. Finally, given the sensor data for a new layer, the dictionary is used to predict the average pore length level in the layers.

The rest of this study is structured in the following manner. Sec.5.2, summarizes the previous research in-process mapping and sensor-based monitoring of the DED process. Next, Sec. 5.3 describes the experimental conditions for making titanium alloy test parts and the design of the in-process system. Sec.5.4 explains the graph-theoretic approach for the analysis of in-process sensor data. In Sec. 5.5, the graph-theoretic approach is used to detect the level of porosity in the test coupons from the in-process sensor signals acquired during experiments. The conclusion and future work are summarized in Sec. 5.6.

## 5.2 Prior Work and Challenges in In-process Sensing in DED

This literature review is divided into two parts. The first part summarizes the DED process from the process mapping perspective by focusing on a review of the literature concerning the effect of process parameters on mechanical and physical properties. The second part summarizes the research in the area of in-process sensing and analytics in DED.

There are numerous factors in DED; some of these consequential factors are enumerated in accordance with the schema described by Craeghs *et al.* for a different process (PBF) in Table 5-1[81]. Typical process defects in DED include cracking and part geometry distortion due to high cooling rates; improper fusion or bonding of layers called lack-of-fusion porosity due to either insufficient energy for melting the material (i.e., the powder flow rate is excessive in relation to the energy supplied) or due to deficient powder flow rate relative to the volume; porosity from powder contamination and gas entrapment; microstructure heterogeneity defects as a consequence of thermal phenomena; and inter-road (hatch line) defects resulting from poor process planning [81]. Within the context of process mapping, Vetter *et al.* listed the various material-process-machine interactions governing the DED process [147]. A review of different control strategies for these defects is provided by Boddu *et al.* [96].

We direct the reader to recent studies by Shamsaei *et al.* and Wang *et al.* which discuss the effect of process parameters on the microstructure and physical properties of AM parts. For instance, a recent study by Foster *et al.* examined the effect of dwell time (the time between deposition of successive layers) on the microstructural evolution for Ti-6Al-4V and Inconel 625, and demonstrated that a longer dwell time in general results in finer

microstructure in both materials, and consequently impacts the resulting mechanical properties, namely, microhardness and yield strength. Furthermore, the authors found that the microstructure varies with the distance from the substrate. For instance, in Inconel 625 the dendritic spacing is finest near to the substrate, and progressively increases with height, and decreases after reaching a peak value.

Table 5-1: Boundary conditions and input parameters in DED processes.

Boundary Condition Factors		Controllable Input Parameters		
Part Design Factors	Material Factors	Environmental Factors	Process-Machine Factors	Laser Optics and Scanning Factors
Part orientation.	Material type and purity.	Oxygen concentration.	Powder flow rate.	Laser power, spot size and geometry.
Part overhang.	Powder particle size and distribution.	Chamber temperature and chamber gas factors.	Layer height.	Beam coherence, shape, and focus integrity.
Platen (Substrate) type and thickness.	Powder capture and reuse.	Substrate temperature.	Carrier and shielding flow rate.	Rastering (hatch) pattern and spacing.
Location, Contact area and design of supports.	Foreign residue as a result of processing.	Cleanliness of the lens and exhaust efficiency.	Wavelength and operating mode.	Laser scan speed (velocity), hatch distance.
	Powder flowability.	Number of degrees of freedom of table and laser.	Nozzle stand-off.	Dwell time.
	Powder mixing in the hopper.	Integrity/accuracy of the machine elements.	Injection angle.	
			Nozzle geometry.	

In a similar vein, Keist and Palmer investigated the effect of geometry and build direction on the microstructure and tensile strength of samples. Test samples were made from thin-wall and thick-wall structures (wall with multiple hatches) deposited in two different geometric patterns. The tensile strength of the test samples extracted (machined) interacted with the shape, number of hatches (wall thickness), and the direction (parallel or perpendicular to the build direction).

This brief summary of the literature thus exemplifies the complex interactions between DED process parameters, thermal phenomena, part geometry, microstructural evolution, and part properties. In the context of monitoring and control of DED processes, research efforts can be stratified into three aspects; a review of these techniques is available in Reutzel *et al.*[148].

- (i) Melt pool monitoring chiefly devolves into measuring the thermal aspects of the deposition process. The shape, intensity, and temporal aspects of the melt pool are measured, typically using infrared pyrometers and CMOS or a CCD camera fitted with a NIR filter. Infrared (IR) sensors are also often used to get a reading of the temperature of the melt pool.
- (ii) Powder delivery rate monitoring uses laser photodiodes and imaging techniques to assess the adequacy of the powder flow rates. The sensing system is typically coupled to the delivery tube (Hu and Kovacevic [149]) or the nozzle side (Boddu *et al.*[150]).
- (iii) Layer morphology monitoring involves assessing the shape and physical aspects of the deposited layer. Traditionally, a line laser is projected on a deposited layer. The reflection is captured using a camera and subsequently analyzed using image

processing techniques (to account for distortion). The output is the layer height (or clad height). Recently, laser spectroscopy has been investigated as a means to go beyond simple height measurement towards measurement of the characteristics of a deposited road (hatch spacing) [138].

Vetter *et al.* [147] discussed the various factors and interactions in DED, they delineated the following two interaction zones concerning the powder flow that have a consequential impact on the quality of the build.

- (i) The first interaction zone occurs in the region where the powder leaves the nozzle, and involves the laser, gas, and powder.
- (ii) The second interaction zone occurs at the region where the powder contacts the substrate and involves the substrate in addition to the first interaction zone.

To understand the effect of these interactions on the build quality, Vetter *et al.* [147] integrated multiple sensors into the machine. The material flow properties were characterized using an optical sensor coupled to a spectrometer. The shape of the stream was captured using a CCD camera, while the powder flow characteristics were recorded with four silicon photodiodes, and finally, a pyrometer measured the melt pool temperature. These sensors enabled the authors to map important aspects, such as powder flow rate and temperature gradients at various locations between the nozzle and substrate.

Nassar *et al.* [138] captured the optical emission using a spectrometer in the second interaction zone; the setup was identical to the one used herein. The central premise was that the optical emission spectrum of an incompletely fused hatch would be markedly different from that of a well-fused hatch. The emission spectrum measurement was in the

200 nm to 1100 nm range, which spans the UV to near infrared (NIR) spectrum. The sampling rate of the spectrometer was maintained close to 8 Hz. Nassar *et al.* [138] deposited Ti-6Al-4V layers with varying hatch spacing; the hatch spacing was progressively increased during the deposition of each layer [138].

At the outset, the optical emission spectra was devoid of any sharp peaks for a well-fused portion of the layer, i.e., where the hatch spacing was smaller. The absence of sharp peaks in the optical emission spectrum meant that distinctive elemental forms were not detected. Conversely, if clear spikes corresponding to the powder elements were detected, then, it implied that the material was not well-fused. The experimental results reported by Nassar *et al.* showed spikes corresponding to Vanadium and Titanium in those portions of the part where the hatch spacing was excessive. Taking this rationale forward, the authors quantified the optical emission spectrum.

This quantification was done by using the line-to-continuum ratio found by computing the ratio of the area under a particular wavelength band to the lower envelope of the area of the entire 200 nm to 1100 nm spectrum, as opposed to the two specific spectra at the 430 nm and 520 nm regions. The line-to-continuum ratio was used as a monitoring statistic in a control chart-like schema. Bartkowiak [151] also investigated spectroscopy as a means for online monitoring in DED. A spectrometer was used by Bartkowiak to observe the optical emission in the 247  $\mu\text{m}$  – 472  $\mu\text{m}$  (i.e., UV to the violet-blue region of the visible spectrum). Visibly evident differences in the emission spectra are reported for different process conditions. However, quantification of the differences in spectra with respect to the processing conditions is not reported.

Song and Mazumder [139] also used laser spectroscopy for monitoring the elemental composition of the deposit. They plotted calibration curves mapping the spectrum behavior versus material composition. Experiments were conducted with chromium-based tool steel powders with varying chromium compositions. In a related work, Mazumder *et al.* [139] used optical spectrometry to identify elemental phase transformation in various powder compositions, including, iron-nickel, iron-titanium, and iron-chromium binary powders. In an alternative development, Mazumder *et al.* [139] used a system with three CCD cameras for measuring the height of the melt pool, along with a dual color pyrometer for measuring the temperature of the melt pool. The instantaneous layer height was tracked by a triangulation method from the images gathered by the CCD cameras. The dual color pyrometer operated in the NIR – SWIR range (1.3  $\mu\text{m}$  and 1.4  $\mu\text{m}$ ).

If the layer height deviates above the set point due to deposition of excessive powder flow rate, the laser power is reduced so that material fusion reduces. In contrast, if the layer height is less than the set point, the temperature sensor reads a proportionally lower temperature. This in turn activates a controller that increases the laser power, and also increases the amount of material deposited to compensate for the drop in layer height.

Mazumder *et al.*, [139] used this feedback control approach to build turbine blade sections with mitigated distortion in shape due to inordinate heating of narrow, thin wall sections. In an earlier work, Song and Mazumder [152] described a state-space predictive controller based on readings from the dual color pyrometer alone. In a recent work by Wang *et al.*, a physics-based feedback control approach, as opposed to purely data-driven method, was used. The road width and height was measured in-process with a 3D spatial

optical profilometer, and the laser speed and deposition speed were used as input variables to control the melt pool cross-section area [153].

Bi *et al.* [154, 155] developed an approach using a single-color infrared pyrometer for closed-loop control of the laser power in DED. The signals from the IR pyrometer sensor were experimentally correlated with the laser power and quality of the deposited surface. The control strategy was to maintain the laser power (which was also separately measured) at a set point by correlation with the IR pyrometer. Essentially, the pyrometer signal was coupled to the laser power. As the pyrometer signal increased (decreased) from an *a priori* set threshold, then the laser power was increased (decreased). Bi *et al.* [155] also studied the effect of laser power on deposited layer quality in terms of presence of surface defects and oxidation. The above-mentioned control strategy was tested on two powder material combinations, namely, stainless steel and Ni-based super alloys.

Researchers have recently begun to integrate the data being acquired using in-process sensors with contemporary machine learning approaches capable of extracting signal patterns, and further correlating these patterns with phenomena evocative of specific defects from the large amount of data. For instance, Khanzadeh *et al.* [156] investigated the effect of a heat affected zone on the emergence of the pores in the direct laser deposition process. They demonstrated that by monitoring the features of melt pool images acquired from a dual-wavelength pyrometer, the onset of defect formation in terms of lack-of-fusion or gas pores could be predicted through machine learning. In this study, they used the statistics obtained from functional principal component analysis (FPCA) as predictors to estimate the probability of pore formation [156].

### 5.3 Experimental Setup and Data Acquisition

This section is divided into two parts: Sec. 5.3.1, describes the experimental conditions used to produce the test coupons; and Sec. 5.3.2, describes the in-process sensing setup.

#### 5.3.1 Experimental Test Conditions

The Optomec LENS MR-7 DED system was used in this work. The following process parameters were varied: laser power ( $P$ , Watt), powder flow rate ( $F$ , g/min), and hatch pattern ( $H$ , cross hatch pattern, and parallel hatch pattern). Other key parameters that were maintained constant are as follows: print speed (10.6 mm/sec), layer height (0.254 mm), and hatch spacing (1 mm). Concerning the hatch pattern, for the parallel pattern, the laser paths in consecutive layers were in the same direction, whereas, in the cross hatch pattern, there was a  $90^\circ$  rotation in the hatch direction in alternate layers.

The material used for printing the test parts was the titanium alloy Ti-6Al-4V in powder form consisting of spherical particles with median powder diameter ( $D_{50}$ ) of 37.72  $\mu\text{m}$ . A 500 W fiber laser with a second moment diameter of 1.24 mm provided the energy for melting the powder. The test part was a cuboid-shaped coupon with the dimensions of 15 mm  $\times$  15 mm  $\times$  10 mm ( $L \times W \times H$  – the build direction is parallel to the edge), which was printed under the ten combinations of printing parameter settings reported in Figure 5-1. Each test coupon was comprised of 40 layers with 12 hatches per layer built on a 6.35 mm-thick Ti-6Al-4V substrate. A photograph of a representative coupon and the offline X-ray Computed Tomography (XCT) slices taken at the second layer for each of the ten different printing conditions is shown in Figure 5-1.

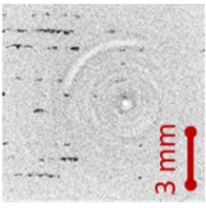
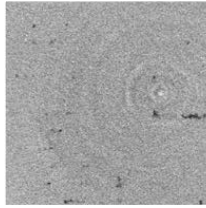
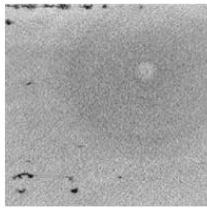
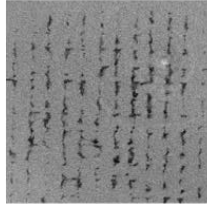
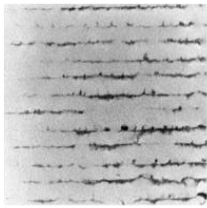
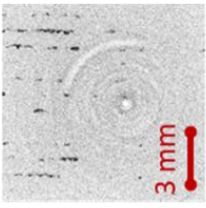
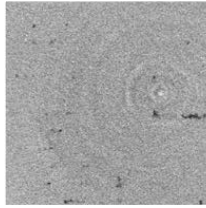
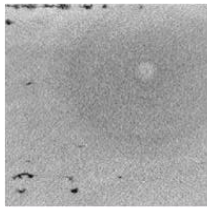
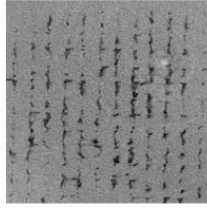
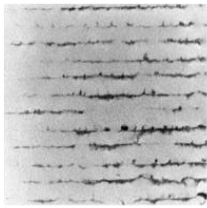
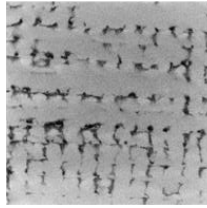
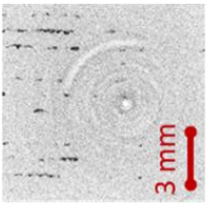
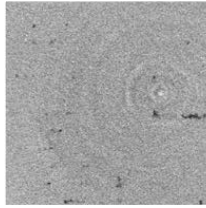
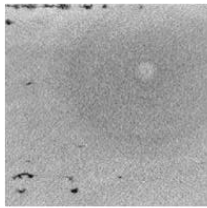
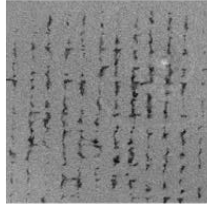
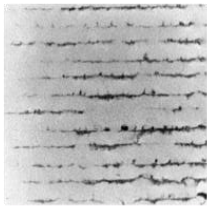
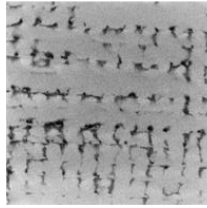
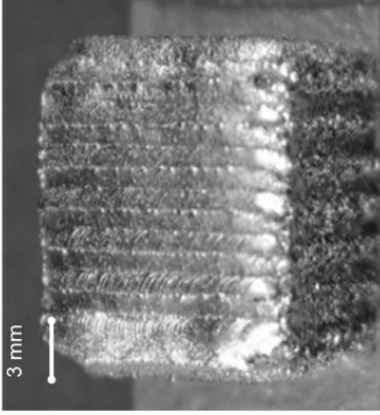
Laser Power (P, Watt)							
		300		425		475	
Hatch Pattern (H)	Powder Flow Rate (F, g/min)	Parallel	Cross	Parallel	Cross	Parallel	Cross
		2					
3							
4							
		 Representative Test Coupon 3 mm					

Figure 5-1: The XCT scans at the same layer for ten selected printing conditions.

### 5.3.2 In-Process Heterogeneous Sensor Setup and Data Acquisition

In this study, two different types of sensor signatures were acquired along with the time and location of the laser beam during the build. The first type of sensor installed on the machine was a spectrometer that measured the line-to-continuum ratio of two spectral emissions during the deposition process. The second type of sensor was a CCD camera that imaged the melt pool plume region. The specifications associated with these sensors are reported in Table 5-2. A photograph of the apparatus is shown in Figure 5-2.

Table 5-2: The information related to the spectrometer and plume camera used in the DED machine.

	Plume Camera	Spectrometer
Specifications	Basler Pilot piA640-210gm CCD camera	Ocean optics HR2000+ UV-VIS-IR spectrometer
Locations	152 mm from laser interaction zone inclined at 30° angle relative to the substrate in the vertical plane.	109 mm from laser interaction zone inclined at 20° angle relative to the substrate in the vertical plane.
Detail	Integration time: 20 ms Wavelength: [200 nm -1100 nm] Slit width: 10 $\mu$ s Resolution: 1 nm (FWHM) optical fiber: 600 $\mu$ m core diameter	Exposure time: 10 ms Between images lag: 20 ms

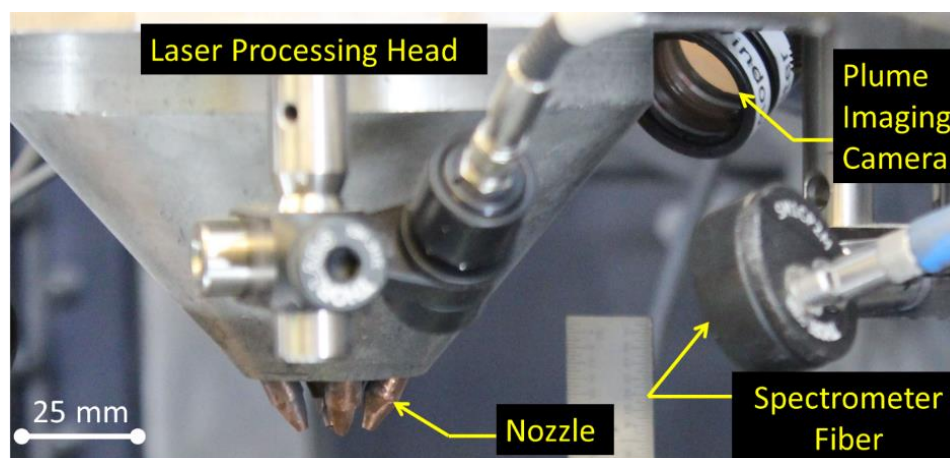


Figure 5-2: The image of the spectrometer and plume camera integrated into the DED machine.

The features extracted from the spectrometer signal and plume camera images were the line-to-continuum ratio and total plume area, respectively. Two line-to-continuum ratios were estimated at wavelengths of 430 nm and 520 nm that corresponded to the emission of Ti (I)[157]. The concept of the line-to-continuum ratio and optical emission spectroscopy for AM applications was explained in recent publications by Nassar *et al.*[127, 138]. The total plume area was calculated after binarization of the plume images.

The difficulty in using the raw (unprocessed) signal features to differentiate between different levels of porosity is illustrated in Figure 5-3. Using the same number of data points in three layers (500 total measurements), the histogram of the line-to-continuum ratio at 520 nm was plotted for an identical number of bins ( $n = 15$ ) to provide a consistent metric for comparison. A subtle distinction in the shape of the empirical probability distribution is evident in Figure 5-3(a). Similarly, Figure 5-3(b) represents the sample data for the plume imaging area. From these frequency plots, it is evident that while a subtle difference in the histogram shape can be discerned, quantification of the same is exceedingly challenging. In the forthcoming section, the graph-theoretic approach is described to combine the data from two sensors.

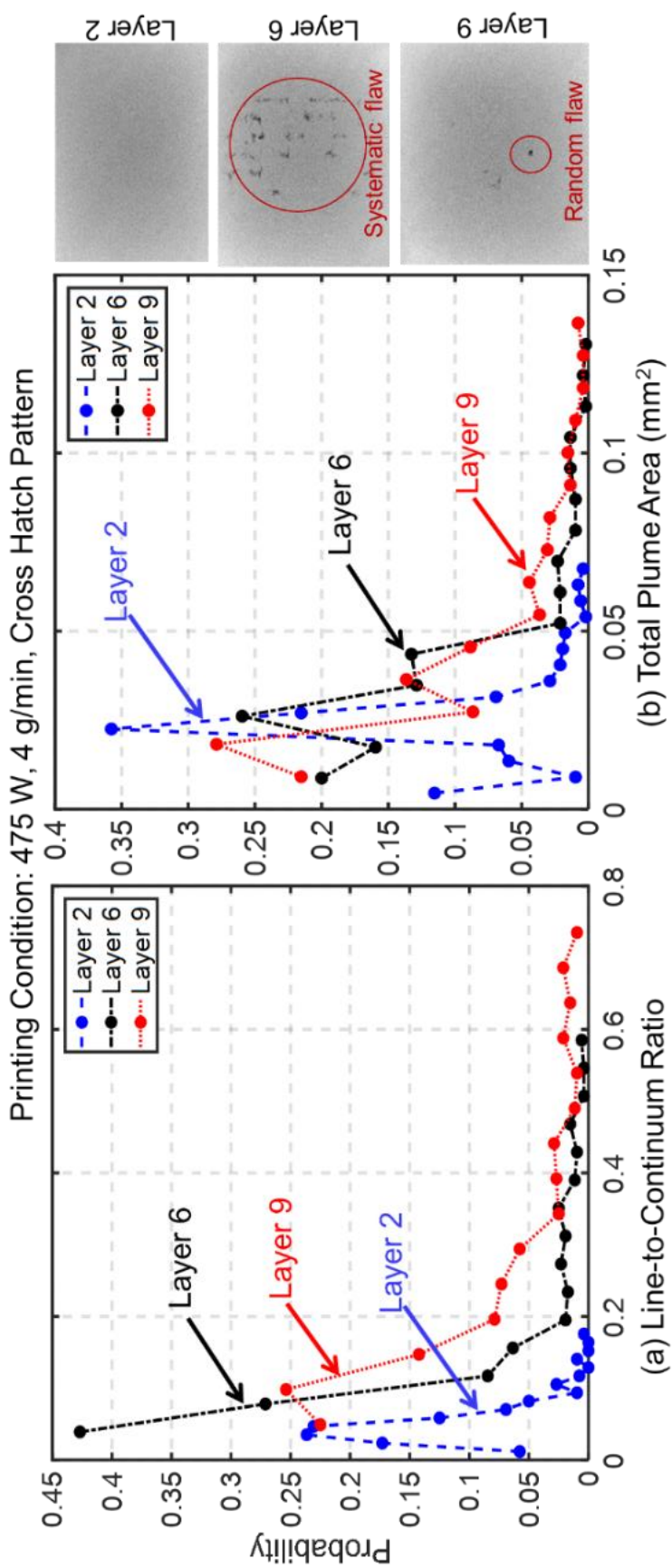


Figure 5-3: the probability distributions of the sensor signatures. (a) line-to-continuum ratio and (b) total plume area. All are related to three different layers when the printing conditions set at laser power = 475 W, flow rate = 4 g/min, and hatch pattern is cross.

#### 5.4 Proposed Methodology

The proposed approach to synthesize sensor information, and subsequently, detect the porosity levels in a layer has the following steps:

*Step 1.* Combining the data from various sensors in one layer in the form of the network graph.

*Step 2.* Analyzing the data across layers using the concept of Kronecker product of graphs, and thus forming a dictionary of signal patterns.

*Step 3.* Training a machine learning algorithm to predict the average porosity value in a layer as a function of the dictionary (input).

We herewith detail each of these steps.

*Step 1:* Combining the data from multiple sensors into a network graph

As explained previously, at first, the representative features from each of the sensor data in-process are extracted. In the case of the spectrometer, the line-to-continuum ratio around the 430 nm and 520 nm wavelength range were extracted. Thus two channels of data were obtained from the spectrometer. In the case of the plume camera data, the total projected area of the image was estimated using an image processing technique. Accordingly, There is a total of three channels of data.

Given the different sampling frequencies for the spectrometer and plume camera, the line-to-continuum ratios and the plume total area measurements were not identical in the number of samples gathered in a layer. To overcome this impediment, the sensor data streams associated with the middle section of the 10 mm × 10 mm test part were used.

Focusing our analysis on sensor data acquired from the middle area of the test part allowed eliminating the effects, such as the ill-developed and abrupt changes in the plume image around the edges. Lastly, the data from the spectrometer and the plume camera were downsampled to 30 data points per layer (15~18 individual data points were averaged).

Labeling the two line-to-continuum measurements at a given instant  $t$  in layer  $L$  as  $x_t^L$  and  $y_t^L$ , and the corresponding plume area as  $z_t^L$ , the sensor data for a particular layer ( $L$ ) could be represented in matrix form  $X_L$  as follows:

$$X_L = \begin{bmatrix} x_1^L & y_1^L & z_1^L \\ x_2^L & y_2^L & z_2^L \\ \vdots & \vdots & \vdots \\ x_t^L & y_t^L & z_t^L \\ x_N^L & y_N^L & z_N^L \end{bmatrix} \quad (5-1)$$

In the matrix  $X_L$ , each row is a data point obtained at the time instant  $t$ , indexed by a sensor along each column. This data was converted into a weighted network graph as discussed in our previous works, and thus a brief summary is only mentioned herewith [13, 25]; The Mahalanobis distance between each row of the data  $X_L$  is calculated as follows,

$$w_{ab} = (\vec{r}_a^L - \vec{r}_b^L)C^{-1}(\vec{r}_a^L - \vec{r}_b^L)^T \quad (5-2)$$

where  $\vec{r}_a^L$  and  $\vec{r}_b^L$  are the  $a^{th}$  and  $b^{th}$  row of the matrix  $X_L$ , and  $C^{-1}$  is the inverse of the covariance matrix of  $X_L$ . The calculated distances using Eq. (5-2) will be represented as a matrix  $S_L$ , called the similarity matrix.

$$S_L = [w_{ab}] \quad (5-3)$$

The matrix  $S_L$  is the weighted, undirected graph representation of the data in layer  $L$ . For ease of notation, the graph of layer  $L$  is denoted as  $G_L$ . In summary, the individual sensor data in each layer is transformed into a weighted undirected graph  $G_L$ .

*Step 2: Building a dictionary of graph-theoretic features related to the porosity level*

Given a graph  $G_L$  for each layer  $L$ , every test part can be described as a set of  $N$  graphs ( $N = 40$  in this study, i.e., 40 layers), through the following *Kronecker* product random walk kernel,

$$D_c = \begin{bmatrix} k(G_1 \otimes G_1) & \cdots & k(G_1 \otimes G_N) \\ \vdots & \ddots & \vdots \\ k(G_N \otimes G_1) & \cdots & k(G_N \otimes G_N) \end{bmatrix} \quad (5-4)$$

In the above matrix  $D_c$ , called the *dictionary*, the subscript  $c$  refers to the part condition;  $c = \{1, 2, \dots, 10\}$  in this work, since there are 10 process setting combinations as evident in Figure 5-1. Further,  $G_i \otimes G_j$  is the Kronecker product of graphs  $G_i$  and  $G_j$  which are representative of the sensors data for layers  $i$  and  $j$ , respectively. As an example, the Kronecker product for matrices  $X$  and  $Y$  is described as:

Given,  $X = \begin{bmatrix} 1 & 0 & 1 \\ 0 & 0 & 1 \\ 0 & 1 & 0 \end{bmatrix}$ ;  $Y = \begin{bmatrix} 1 & 1 \\ 1 & 0 \end{bmatrix}$ , the Kronecker product of  $X$  and  $Y$  ( $X \otimes Y$ ) is

described in Eq. (5-5).

$$\begin{aligned}
X \otimes Y &= \begin{bmatrix} X(1,1).Y & X(1,2).Y & X(1,3).Y \\ X(2,1).Y & X(2,2).Y & X(2,3).Y \\ X(3,1).Y & X(3,2).Y & X(3,3).Y \end{bmatrix} \\
&= \begin{bmatrix} 1. \begin{bmatrix} 1 & 1 \\ 1 & 0 \end{bmatrix} & 0. \begin{bmatrix} 1 & 1 \\ 1 & 0 \end{bmatrix} & 1. \begin{bmatrix} 1 & 1 \\ 1 & 0 \end{bmatrix} \\ 0. \begin{bmatrix} 1 & 1 \\ 1 & 0 \end{bmatrix} & 0. \begin{bmatrix} 1 & 1 \\ 1 & 0 \end{bmatrix} & 1. \begin{bmatrix} 1 & 1 \\ 1 & 0 \end{bmatrix} \\ 0. \begin{bmatrix} 1 & 1 \\ 1 & 0 \end{bmatrix} & 1. \begin{bmatrix} 1 & 1 \\ 1 & 0 \end{bmatrix} & 0. \begin{bmatrix} 1 & 1 \\ 1 & 0 \end{bmatrix} \end{bmatrix} \\
&= \begin{bmatrix} 1 & 1 & 0 & 0 & 1 & 1 \\ 1 & 0 & 0 & 0 & 1 & 0 \\ 0 & 0 & 0 & 0 & 1 & 1 \\ 0 & 0 & 0 & 0 & 1 & 0 \\ 0 & 0 & 1 & 1 & 0 & 0 \\ 0 & 0 & 1 & 0 & 0 & 0 \end{bmatrix}
\end{aligned} \tag{5-5}$$

As Eq. (5-5) demonstrates,  $X \otimes Y$  is the multiplication of each entry in matrix  $X$  by the whole matrix  $Y$ . Therefore, if matrices  $X$  and  $Y$  have the dimensions of  $(p \times q)$  and  $(r \times s)$  respectively, the  $X \otimes Y$  would be a  $(p \times r) \times (q \times s)$  matrix. Next, the so-called *random walk kernel* kernel  $k(G_i \otimes G_j)$ , representative of the similarity between graphs  $G_i$  and  $G_j$  is obtained from the Kronecker product  $(X \otimes Y)$  as follows [158], letting,  $G_i \otimes G_j = S_{i,j}$ ,

$$k(G_i \otimes G_j) = k(S_{ij}) = \sum_{\substack{\forall \text{rows,} \\ \text{columns}}} \left( I - \gamma_{ij}(S_{ij}) \right)^{-1} \tag{5-6}$$

In graph-theoretic terminology, a random walk encapsulates the number of sequential nodes and edges that need to be traversed to reach a random node B from a starting node A. Equation (5-6) describes the calculation of the random walk kernel where  $I$  is the identity matrix and  $\gamma_{i,j}$  is the decay constant. The decay constant  $\gamma_{i,j}$  is the inverse of the maximal sum taken over the rows (or columns) of  $S_{i,j} = (G_i \otimes G_j)$ .

*Step 3:* Predicting the average porosity value in a layer using the dictionary.

This step had two sub-parts: the first was training a machine learning model to learn the relationship between the dictionary  $D_c$  and the corresponding porosity level, and the second to predict the corresponding porosity level in a layer given new sensor data.

The porosity level was quantified as the average pore length. At first it is observed that the data from layer  $i$  of a part resides in the corresponding row  $i$  of the matrix  $D_c$ . Accordingly, the  $i^{\text{th}}$  row of the matrix  $D_c$  is paired with the corresponding pore length observed for the  $i^{\text{th}}$  layer from the XCT data. The procedure to extract the porosity in the form of desired porosity features is explained in Sec. 5.5.1. Essentially, if there were  $N$  rows and  $N$  columns in  $D_c$ , each row was an input vector corresponding to a layer and each column was an independent variable. The output variable was the corresponding average pore length for the layer obtained from the XCT data.

To simplify the problem, instead of combining all the  $N$  variables (columns) in the  $i^{\text{th}}$  row of the dictionary  $D_c$ , a dimension reduction technique is used. This was done by subjecting the dictionary  $D_c$  to the well-known principal component analysis (PCA), and using only the first two principal components, instead of all the columns of the matrix  $D_c$ , as the input to predict the porosity of each layer. On the output side (porosity), instead of using the average pore length, it is classified into either two or three pre-selected discrete classes. For predicting the porosity-level given the input sensor signals, the popular and easily implemented support vector machine (SVM) technique with a linear discriminant kernel was used.

The second part of this step was to make a prediction once new sensor data was obtained. The approach is as follows. Consider a data stream  $X_{New}$  for a new layer identical to the matrix  $X_L$  in Eq. (5-1). Following the procedure described in Eq. (5-2) and (5-3), the data  $X_{new}$  is first converted into the corresponding graph form  $G_{new}$ . Next, the matrix  $\theta_{new}$  is obtained as follows, where  $G_1$  to  $G_N$  are the older data.

$$\theta_{new} = [k(G_{new} \otimes G_1) \quad \dots \quad k(G_{new} \otimes G_N)] \quad (5-7)$$

The input vector in Eq. (5-7) was presented to an *a priori* trained machine learning model after the PCA procedure, to obtain the corresponding porosity level given the data  $\theta_{new}$ .

## 5.5 Results and Discussion

This section is divided into two parts. In Sec. 5.5.1 the statistical significance of three process parameters is analyzed, namely: laser power (P, Watt), powder flow rate (F, g/min), and hatch pattern (H, cross vs. parallel) on the average pore length in each layer. Furthermore, in Sec. 5.5.2, the graph-based analysis of the in-process sensor data is used as described in the preceding Sec. 5.4, to predict the quality of a layer in terms of the average pore length.

### 5.5.1 Offline Statistical Analysis of Porosity from XCT Slices

As explained in Sec. 5.3, this work involves the DED of 10 test parts. Subsequent to deposition, these parts were analyzed with X-ray Computed Tomography (XCT). In this section, the process parameters with the severity of lack-of-fusion porosity level in terms of the average pore length per layer are linked. Then, each slice of the XCT (the step height

for an XCT slice is 15  $\mu\text{m}$ ) is analyzed using an image processing technique which consisted of two steps which are illustrated in Figure 5-4.

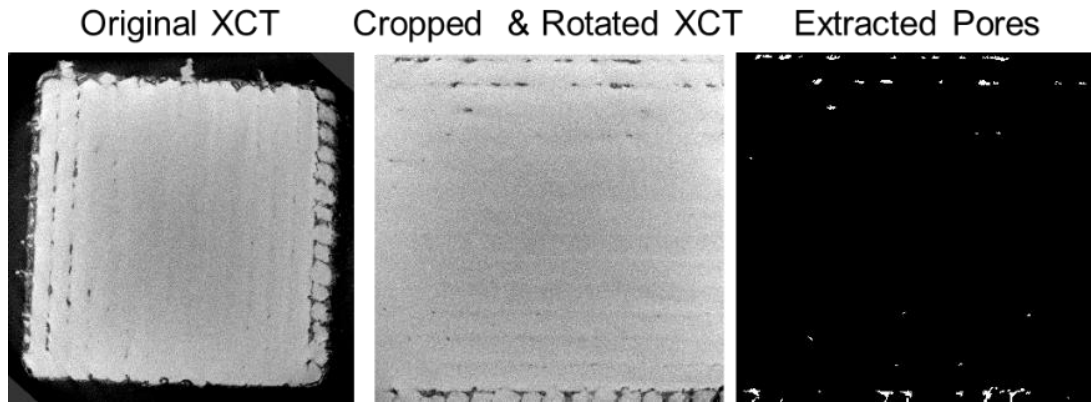


Figure 5-4: The image processing steps for the extraction of pores from XCT slices.

1. Cropping and rotation of the XCT slices to remove edge effects.

Given the non-homogeneous and jagged shape of the part near the edges, the original XCT images were cropped and rotated. Cropping left the middle 10 mm  $\times$  10 mm in the X-Y plane of the test part for analysis. Next, the images were rotated to synchronize the XCT with the coordinate system of the DED machine.

2. Extracting the average pore length layer from the binarized XCT images.

The XCT images were first binarized using image processing techniques, with a heuristically set threshold value for each test part. Further, the step height of the XCT slices was less than the layer height; roughly 17 XCT slices were related to one deposited layer. Hence, the pores for 17 consecutive slices were projected on a single plane. Figure 5-5 represents the distribution of the estimated porosities from 6 printed parts with identical laser power ( $P = 300 \text{ W}$ ) but different flow rate and hatch pattern settings.

A visual comparison between each column of Figure 5-5 reveals that by increasing the volume of powder flow rate under the same laser power, porosity tended to increase in

severity. This phenomenon is explained as follows; by adding more material to the laser interaction zone, the energy density available for fusion of a unit mass of powder considerably reduced, which in turn manifested in lack-of-fusion porosity.

We used the average pore length in a layer as a measure of layer quality. The pore length was determined as the length of the major axis of an ellipse that encompassed a pore. The average pore lengths for the 10 test parts aggregated across 40 layers are tabulated in Table 5-3. The effect of the three process parameters, power (P), powder flow rate (F), and hatch pattern (H) on the average pore length per layer is visualized in Figure 5-6. Further, to statistically quantify the printing conditions, a generalized linear regression analysis is conducted with the process parameters as inputs and the average pore length as output, which revealed that all the three main parameters were statistically significant determinants of average pore length (at statistical significance level of  $\alpha = 5\%$ ).

Moreover, the following interaction effects were also statistically significant:  $P \times H$ , and  $P \times F$ . The regression coefficient ( $R^2$ -adj.) was 47% with all terms (main effects and interactions) included, and 42% with only main effects, i.e., P, F, and H. This statistical analysis indicated that the process parameters were capable of explaining less than 50% of the variation in the data. In other words, if the process parameters were to be used as the sole predictors of lack-of-fusion porosity in a layer, the fidelity of the prediction would be less than 50%. Accordingly, there is a need to augment the process parameters with in-process sensor signatures to predict pore formation in DED.

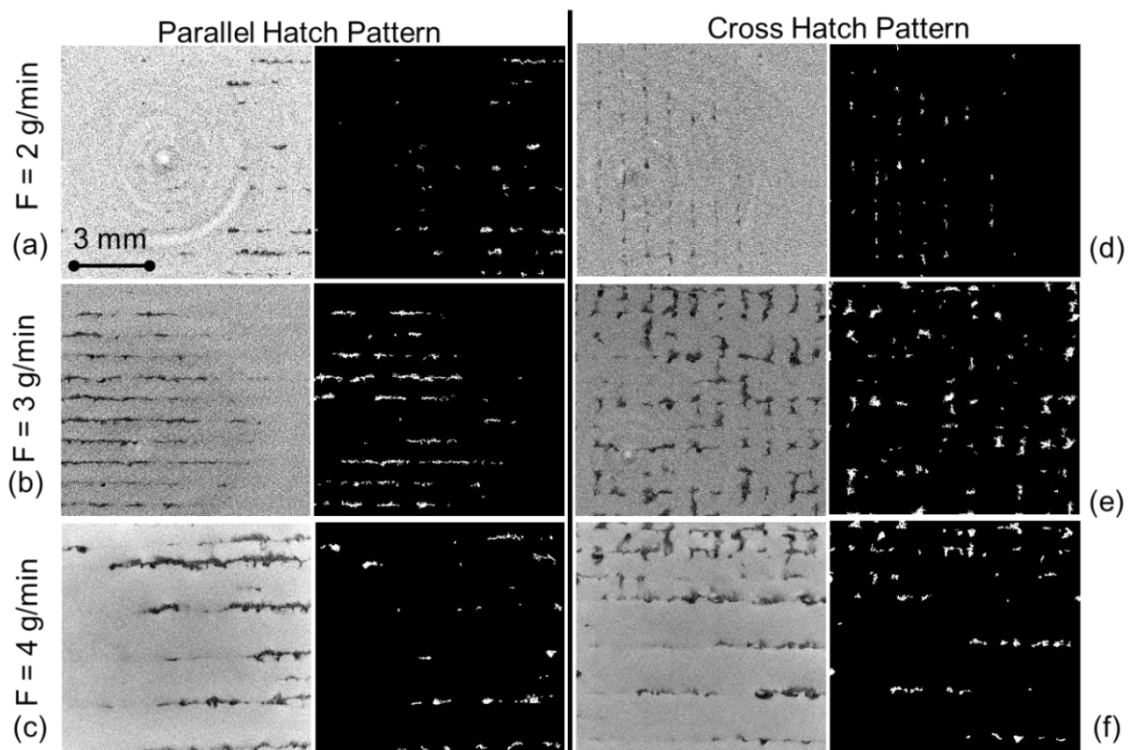


Figure 5-5: The flaws extracted from the XCT.

The XCT images are from the same layer for samples that were processed under 300 W laser power but differing flow rate and hatch pattern. Samples a, b, and c have the parallel hatch pattern vs. d, e, and f that have a cross hatch pattern. The powder flow rate increases from top to the bottom.

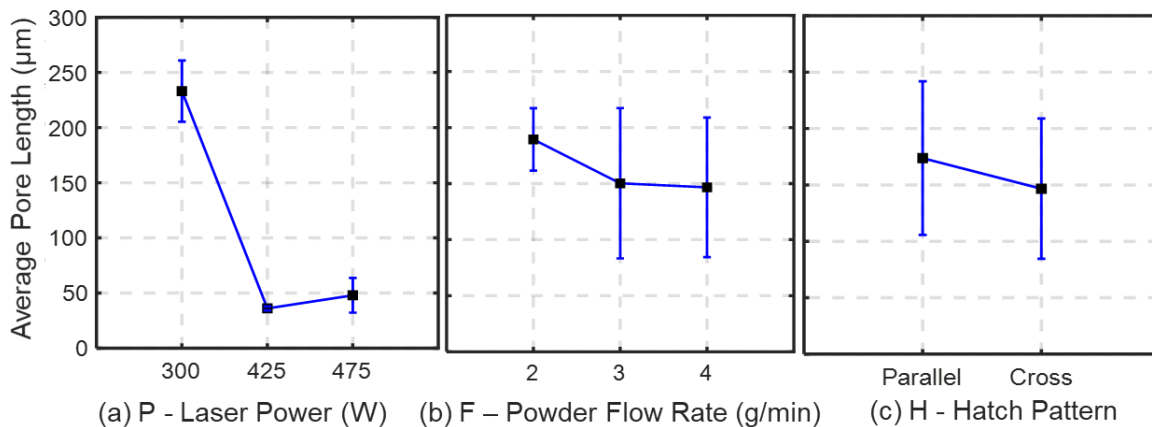


Figure 5-6: Main effects plots each DED process parameter.

(a) laser power, (b) powder flow rate, (c) and hatch pattern. The error bars represent a variation of one standard deviation.

Table 5-3: Printing conditions of 10 parts and their estimated average and maximum pore length.

Laser Power [W]	Powder Feed Rate [g/min]	Hatch Pattern	Energy per unit mass of powder flow [kJ/g]	Mean of Maximum Pores Length over 40 layers [ $\mu\text{m}$ ]	Mean of Average Pores Length over 40 layers [ $\mu\text{m}$ ]	Remarks	Assigned class
300	4	Parallel	4.5	1277	302	Low energy	Average Pore Length per layer > 200 $\mu\text{m}$
300	3	Parallel	6	1356	294	Low energy	
300	3	Cross	6	794	235	Low energy	
300	2	Parallel	9	629	213	Insufficient mass flow rate	
300	4	Cross	4.5	575	189	Low energy	50 $\mu\text{m}$ < Average Pore length per layer < 200 $\mu\text{m}$
300	2	Cross	9	400	165	Insufficient mass flow rate	
475	4	Cross	7.125	136	70		Average Pore length per layer < 50 $\mu\text{m}$
425	3	Cross	~ 8.5	85	39		
425	3	Parallel	~ 8.5	102	34		
475	4	Parallel	7.125	62	26		

The following inferences can be drawn based on these statistical analysis results:

1. The average pore length is, typically, inversely proportional to the energy per unit volume of powder flow. The reasoning is that more energy was required to fuse a proportionally larger amount of material. Hence, the laser power (P) had a great effect on the part quality, as seen in Figure 5-6(a). Typically, energy per unit mass of over 7 kJ/g was found to be requisite.
2. There is a significant interaction effect amongst process parameters, attesting to the complexity of the process. For instance, severe porosity will result although the energy supplied is sufficiently high to melt the powder if the amount of powder mass flow rate is insufficient vis-à-vis the volume. For instance, in the case of the settings with powder flow rate of 2 g/min, the level of porosity was inordinately high, despite the highest level of energy supplied (9 kJ/g).

3. The average pore lengths per layer can be broadly demonstrated to fall under two categories, namely, less than 50  $\mu\text{m}$  and over 50  $\mu\text{m}$ . A more granular resolution at three-levels would be the less than 50  $\mu\text{m}$ , between 50  $\mu\text{m}$  and 200  $\mu\text{m}$ , and over 200  $\mu\text{m}$  levels

In the forthcoming section (Sec. 5.5.2), these two-level and three-level demarcations will be invoked as discriminants of layer quality.

### 5.5.2 Online Detection of Defects from In-Process Sensor Data

In this section, the average porosity level in each layer is divided into two and three-level classes, as depicted in Table 5-3, and subsequently, train a linear discriminant support vector machine (SVM) model to predict the porosity-level given the sensor data. To train the SVM model, two different techniques contingent on either including or excluding the knowledge of process conditions were used in the prediction algorithm.

In the first scenario, the data from 30 random layers is selected for each of the ten parts to train the corresponding matrix  $D_c$ . Therefore, using Eq. (5-4), each process condition was associated with a unique dictionary which was a  $30 \times 30$  matrix. The relatively small size of this dictionary was advantageous from a computational perspective. In other words, there are ten dictionaries  $D_c$ ,  $c = \{1, 2, \dots, 10\}$  corresponding to the 10 test parts. The rationale is that the parameters such as laser power (P), powder flow rate (F), and hatch pattern (H), etc., are set by the operator, and will seldom change. Hence, given a stream of sensor data, these parameters were *a priori* information that could be used in the model.

In the second scenario, the dictionary  $D_c$  was built based on the random sampling available from all the 10 test parts. Given that there were 40 layers in each of the 10 test

parts, a total number of 400 layers was used as a base set for our sampling. Then 300 layers from the 400-layer data set are sampled to build our training matrix  $D_c$  which was a  $300 \times 300$  matrix (using Eq. (5-4)). In this scenario, the processing parameters were not included, in that the dictionary was not stratified per the process conditions. Then, following Eq. (5-7), the rest of the 100 layers are used for testing the fidelity of the algorithm.

A representative result of the two training scenarios in the form of a confusion matrix is shown in Table 5-4. From Table 5-4 (a), it is evident that treating the process parameters as known entities led to a statistically higher classification fidelity compared to the scenario where the process parameters were assumed to be unknown (Table 5-4 [b]). Further examination of the confusion matrix in the known process condition scenario revealed, as anticipated, classifying the average pore length in two levels was accomplished with greater statistical fidelity compared to the three-level case.

If the statistical fidelity of classification is expressed in terms of the F-score, the two-level classification fidelity was 85% compared to 70% for the three-level case. The F-score includes both the type I and type II errors where a higher F-score is desirable. Continuing with the analysis, this study is extended to include only statistical features, namely, mean, standard deviation, range, skewness, kurtosis, and interquartile range of the spectrometer and plume camera sensor signatures as features (instead of the graph-theoretic features). The results are juxtaposed in Table 5-5, which reveals, affirming our hypothesis, that using the graph-theoretic features extracted from sensor signatures as discriminants of part quality leads to higher fidelity compared to the traditional statistical features.

Table 5-4: (a) Confusion Matrix for two-level and three-level porosity detection. with graph random-walk technique assuming process conditions are **known**.

Confusion Matrix for two-Level Classification			
True Classes ↓	Predicted Classes		
	<i>Low Porosity</i> Average pore length per layer < 50 μm	<i>High Porosity</i> Average pore length per layer > 50 μm	
<i>Low Porosity</i>	20 (out of 26)	6 (False Alarm)	
<i>High Porosity</i>	12 (Failing to detect)	62 (out of 74)	
Confusion Matrix for Three-Level Classification			
True Classes ↓	Predicted Classes		
	<i>Low Porosity</i> Average pore length per layer < 50 μm	<i>Medium Porosity</i> 50 μm < Average pore length per layer < 200 μm	<i>High Porosity</i> Average pore length per layer > 200 μm
<i>Low Porosity</i>	20 (out of 26)	0	6
<i>Medium Porosity</i>	4	21 (out of 37)	12
<i>High Porosity</i>	6	9	22 (out of 37)

Table 5-4: (b) Confusion Matrix for two-level and three-level porosity detection. with graph random-walk technique assuming process conditions are **unknown**.

Confusion Matrix for two-Level Classification			
True Classes ↓	Predicted Classes		
	<i>Low Porosity</i> Average pore length per layer < 50 μm	<i>High Porosity</i> Average pore length per layer > 50 μm	
<i>Low Porosity</i>	2 (out of 34)	32 (False Alarm)	
<i>High Porosity</i>	7 (Failing to detect)	59 (out of 66)	
Confusion Matrix for Three-Level Classification			
True Classes ↓	Predicted Classes		
	<i>Low Porosity</i> Average pore length per layer < 50 μm	<i>Medium Porosity</i> 50 μm < Average pore length per layer < 200 μm	<i>High Porosity</i> Average pore length per layer > 200 μm
<i>Low Porosity</i>	5 (out of 34)	0	29
<i>Medium Porosity</i>	3	0 (out of 34)	31
<i>High Porosity</i>	5	0	27 (out of 32)

Table 5-5: Performance of the graph classification approach in comparison with the statistical feature's classification for the 2-level and 3-level porosity detection.

Input Data	2-level F Score (%)		3-level F Score (%)	
	Conditions Known	Conditions unknown	Conditions Known	Conditions unknown
Graph Random-Walk	<b>84.6 (6.3)</b>	43.6 (4.6)	<b>71.5 (3.9)</b>	21.2 (3.1)
Statistical Features	40.3 (1.0)	40.1 (1.2)	37.3 (2.5)	36.9 (3.5)

## 5.6 Conclusions

This work developed and applied an approach for combining data from multiple sensors to detect the onset of lack-of-fusion porosity in the DED AM process of titanium alloy (Ti-6Al-4V) parts; it thus takes the first steps towards establishing the following links in the AM process chain:

Process parameters → In-process sensor signatures → Defects (lack-of-fusion)

The specific contribution of this work is enumerated as follows.

1. The effect of three process conditions, namely, the laser power (P), powder flow rate (F), and hatch pattern (H) on the average pore length was quantified. The average pore length was obtained through post-process image analysis of the XCT slices of the part. The resulting analysis of the data showed that all the parameters above (P, F, and H) have a statistically significant effect on the average pore length with the laser power having the largest effect. Broadly, the average pore length is inversely proportional to the energy per unit volume of material flow rate, providing the material flow rate is sufficient per the part volume.

2. Three channels of in-process sensor data were acquired during the build, namely, two channels of line-to-continuum optical emission spectra each obtained at 430 nm and 520 nm wavelengths, and the total area of the melt pool plume from a CCD camera.
3. The data from the two spectrometer wavelengths and plume camera for a layer were combined and represented in the form of a network graph. Further, the data across layers was analyzed using the concept of the Kronecker product (tensor product) of graphs. This approach facilitates online analysis of the data, whereby the inception of lack-of-fusion related porosity in layers is predicted with statistical fidelity (F-score) approaching 75% - 85%. In comparison, the traditional statistical feature-based machine learning had corresponding fidelity of 35% - 40%.

This work lays the foundation for a *qualify-as-you-build* framework in AM processes, whereby impending defects are identified before the next layer is deposited, thus allowing opportune corrective action to be taken in case of a fault. Furthermore, given the availability of hybrid DED systems which include a machining attachment apart from a laser deposition head, it is possible to extend the *qualify-as-you-build* concept to a *correct-as-you-build* paradigm, wherein a defect such as lack-of-fusion porosity is detected using sensor data, and corrected before the next layer is deposited by entirely machining the defect afflicted layer.

## Acknowledgments

This work was partially supported by the Office of Naval Research, under Contract No. N00014-11-1-0668. This work was also partially supported by the Air Force Research Laboratory through America Makes under agreement number FA8650-12-2-7230. Any opinions, findings and conclusions or recommendations expressed in this publication are those of the authors and do not necessarily reflect the views of the Office of Naval Research, Air Force Research Laboratory, or America Makes.

## Appendix

As described in Sec. 5.5.2, the target output is to predict the average pore length in a layer given the sensor data. Additional analysis was also implemented using the maximum pore length in a layer as an output feature; the F-score values for the maximum pore length per layer as an output feature are represented in Table 5-3. While the classification fidelity for the two-level case was nearly identical to those reported in Table 5-4, the three-level results were inferior. This is probably due to the precision required in the data to detect a point statistical measure, such as a maximum length of pores in a layer as opposed to an aggregate measure akin to average pore length.

Table 5-6: Performance of the graph classification approach in comparison with the statistical features classification using the maximum pore length.

Input Data	2-level F-Score (%)		3-level F-Score (%)	
	Conditions Known	Conditions unknown	Conditions Known	Conditions unknown
Graph Random-Walk	<b>84.6 (6.3)</b>	44.4 (5.1)	<b>56.9 (2.7)</b>	25.0 (0.6)
Statistical Features	40.3 (1.0)	40.1 (1.2)	37.3 (2.5)	36.9 (3.5)

## 6 Conclusions and Future Work

### 6.1 Research Summary

The goal of this dissertation is to detect defects in metal parts made using additive manufacturing processes through data acquired from sensors incorporated into the machine. This goal leads towards the expansive, overarching vision of a *smart additive manufacturing* paradigm wherein defects are not only detected as the part is being built, but also immediately repaired inside the machine using a corrective closed-loop control strategy.

The advent of additive manufacturing offers unprecedented flexibility in product design and materials and thus has the potential to revolutionize strategically important sectors of the American manufacturing industry. For instance, in the aerospace sector, it currently takes close to 20 pounds of raw material to make a finished part weighing just one pound. Studies have shown that additive manufacturing when done right, can potentially reduce this 20:1 *buy-to-fly ratio* to less than 7:1, while simultaneously decreasing the product lead time from over a month to less than a week.

However, manufacturers in precision-orientated industries, such as aerospace and defense, are reluctant to use additive manufacturing for mission-critical parts, despite the enormous engineering performance, production cost, and delivery time benefits over conventional manufacturing. The crux of the challenge encumbering the broad acceptance and accelerated deployment of additive manufacturing in industry for making production parts, beyond the current prototype-demonstrative role, lies in lack of process repeatability and poor part consistency; defects afflict as much as 20% of additively manufactured parts.

The large variability in part build properties and high build failure rates in the current class of additive manufacturing systems must be overcome if the technology is applied in strategic industries such as aerospace, defense, automotive, and biomedical where safety is paramount. By providing a pathway to detect incipient defects using sensor data before they become permanently sealed in by subsequent layers, this research takes the critical first-steps towards accelerating the production-scale viability of additive manufacturing in strategic industries important to the national prosperity.

As a step towards the overarching vision of smart additive manufacturing, the objective of this work is to develop and apply a novel type of signal processing approach, rooted in the domain of spectral graph theory to analyze the large volume and variety of data acquired from in-process sensors. The central hypothesis of this dissertation is that the process signatures derived by analyzing the sensor data using the proposed graph-theoretic approach are significantly more statistically accurate in identifying the occurrence and severity of part defects compared to signatures derived from statistical signal processing approaches.

This hypothesis is tested on four separate experimental data sets obtained from collaborators at three institutions – the National Institute of Standards and Technology (Dr. Brandon Lane), Edison Welding Institute (Mr. Paul Boulware), and Applied Research Laboratory at Pennsylvania State University (Dr. Abdalla Nassar). These data sets encompass the laser powder bed fusion and directed energy deposition metal additive manufacturing processes.

In the first step, to study the detectability of design-induced defects by the proposed algorithm, an LPBF machine equipped with three types of sensors, namely, a photodetector, a visible camera, and the thermal camera, has been used at NIST. The test artifact with an overhanging edge was opted to be considered as a design with a heat diffusion problem. The statistical accuracy for isolating the thermal patterns belonging to bulk and overhang features represented the preference of the spectral graph-theoretic approach over the conventional statistical ones in terms of the F-score as follows: (a) F-score of 95% from the SWIR thermal camera signatures; (b) 83% with the high-speed visible camera; (c) 79% with the photodetector. In comparison, conventional signal analysis techniques—e.g., neural networks, support vector machines, and linear discriminant analysis were evaluated with F-scores in the range of 40–60%.

Following other sources of anomalies in metal AM, the feedstock-induced defects have been analyzed by contaminating the metal powder (Inconel alloy 625) using tungsten and Aluminum contaminates. To detect the cross-contamination during the build, the photodetector (with 300 nm to 1100 nm optical wavelength) has been acquired to estimate the sensor signatures in the form of spectral graph transform coefficients. These graph coefficients were subsequently tracked on a Hotelling  $T^2$  statistical control chart. Instances of Type II statistical error, i.e., the probability of failing to detect the onset of material cross-contamination, were verified against X-ray computed tomography (XCT) scans of the part to be within 5% in the case of aluminum contaminant particles. In contrast, traditional stochastic time series modeling approaches, e.g., ARMA, had a corresponding Type II error exceeding 15%. Furthermore, the computation time for the spectral graph

approach was found to be less than one millisecond, compared to nearly 100 ms for the traditional time series models tested.

For the third step, the effect of process parameters including laser power, printing velocity, and hatch space on the porosity formation in Inconel 718 at LPBF has been investigated. The objective of this work is to detect the incipient formation of pores related to lack of material fusion in LPBF through in-process optical emission spectroscopy, and subsequently, to identify the level or severity of porosity in real-time using process signatures derived from the optical spectroscopy signals. Further, the LPBF machine was instrumented with a multispectral photodetector sensor array to measure the line-to-continuum ratio optical emission spectroscopy signatures as the part was being built layer-by-layer. The line-to-continuum optical emission signature for each layer of the part was consequently related to the corresponding level of porosity measured, based on offline X-ray computed tomography scans. Using this proposed graph-theoretic machine learning approach to analyze in-process optical emission signatures, the part severity was quantified with accuracy close to 90% and computation time less than 0.5 seconds; in comparison with traditional statistical moments, such as mean, variation, etc., were used as signal features for prediction, the porosity level was identified with less accuracy ( $\approx 80\%$ ) with computational time exceeding 5 seconds.

To evaluate the fidelity of the spectral graph-theoretic approach in a DED process, the fourth experiment was conducted on an Optomec MR-7 DED machine. In a DED process for fabricating the titanium alloy (Ti-6Al-4V) parts, the data from two types of in-process sensors, namely, a spectrometer and a plume camera had been acquired. To detect lack-of-fusion porosity from this sensor data, an approach is devised to fuse (combine) the data

from the in-process sensors, invoking the concept of Kronecker product of graphs. Specifically, the random walk kernel derived from the graph Kronecker product is used as inputs to a machine learning algorithm to predict the severity (level) of average pore length in a layer, which was obtained from offline X-ray Computed Tomography of the test parts. Consequently, it is demonstrated that the pore severity is classified with statistical fidelity close to 85% (F-score) for a two-level classification of pore severity, and  $\approx 70\%$  F-score for a three-level classification scenario.

## 6.2 Future Work

The sensing and control of AM processes are among the highest priority needs for realizing the technology's potential. This work lays the foundation for a *qualify-as-you-build* Smart Additive Manufacturing framework in AM processes, whereby impending defects are identified before the next layer is deposited, thus allowing the opportune corrective action to be taken in case of a fault. However, regarding the challenges and limitations of this research, there are the following unanswered, open research questions.

- i. What other different types and more relevant defects, such as microstructure heterogeneity, may be detected from in-process sensor data?
- ii. What is the link between specific defects and sensor signal patterns? In other words, is there a one-to-one link between a type of defect and its severity, and the sensor signature it manifests?
- iii. What is the detection lag; does the detection accuracy improve with sensor redundancy?
- iv. What is the effect of sensor noise and position on the detection accuracy?
- v. How is the effectiveness of the approach affected given different geometries and materials?

A major drawback of this work is that it used only a single type of sensor in chapters 2-4 to detect a specific type of defect, namely, heat accumulation, material cross-contamination, and porosity. The efficacy of the approach using multiple sensors for different types of defects is investigated peripherally in chapter 5 but remains to be ascertained. In other words, both sensors captured the identical phenomena, named state-of-the-plume, which prevented the improvement of detecting algorithms by sensor fusion techniques.

Furthermore, different characteristics of the defects like severity or distribution could not be isolated based on the sensor data; and the effect of flaws or a specific phenomenon on the functional mechanical properties needs to be quantified through materials testing. This will allow completing the loop between process phenomena, sensor signatures, and part properties. Researchers in the Laboratory for Advanced Manufacturing Processes and Sensing (LAMPS) will endeavor to address these gaps in their future work in the area.

## References

- [1] Gibson, I., Rosen, D. W., and Stucker, B., 2010, Additive manufacturing technologies: rapid prototyping to direct digital manufacturing, Springer, New York.
- [2] Lipson, H., and Kurman, M., 2013, Fabricated: The new world of 3D printing, John Wiley & Sons.
- [3] Kellner, T., 2017, "An Epiphany Of Disruption: GE Additive Chief Explains How 3D Printing Will Upend Manufacturing," <https://www.ge.com/reports/epiphany-disruption-ge-additive-chief-explains-3d-printing-will-upend-manufacturing/>.
- [4] Huang, R., Riddle, M., Graziano, D., Warren, J., Das, S., Nimbalkar, S., Cresko, J., and Masanet, E., 2016, "Energy and emissions saving potential of additive manufacturing: the case of lightweight aircraft components," *Journal of Cleaner Production*, **135**, pp. 1559-1570. doi: 10.1016/j.jclepro.2015.04.109
- [5] Conner, B. P., Manogharan, G. P., Martof, A. N., Rodomsky, L. M., Rodomsky, C. M., Jordan, D. C., and Limperos, J. W., 2014, "Making sense of 3-D printing: Creating a map of additive manufacturing products and services," *Additive Manufacturing*, **1**, pp. 64-76. doi: 10.1016/j.addma.2014.08.005
- [6] 2015, "ASTM 52900-15 Standard Terminology for Additive Manufacturing," ASTM International.
- [7] 2016, "F3187-16: Standard Guide for Directed Energy Deposition of Metals. ," ASTM International.
- [8] Frazier, W. E., 2014, "Metal additive manufacturing: a review," *Journal of Materials Engineering and Performance*, **23**(6), pp. 1917-1928. doi: 10.1007/s11665-014-0958-z
- [9] 2013, Report to the National Institute of Standards and Technology: Measurement Science Roadmap for Metal-Based Additive Manufacturing, Energetics Corporation, Gaithersburg, MD.
- [10] Cheng, B., and Chou, K., "Deformation Evaluation of Part Overhang Configurations in Electron Beam Additive Manufacturing," Proc. ASME 2015 International Manufacturing Science and Engineering Conference, American Society of Mechanical Engineers, pp. V001T002A072-V001T002A072.
- [11] Huang, S., Kong, Z. J., and Huang, W., 2014, "High-dimensional Process Monitoring and Change Point Detection using Embedding Distributions in Reproducing Kernel Hilbert Space (RKHS)," *IIE Transactions*, **46**(10), pp.999-1016 doi: 10.1080/0740817X.2013.855848
- [12] Huang, Y., Leu, M. C., Mazumder, J., and Donmez, A., 2015, "Additive Manufacturing: Current State, Future Potential, Gaps and Needs, and Recommendations," *Transactions of the ASME, Journal of Manufacturing Science and Engineering*, **137**(1), p. 014001. doi: 10.1115/1.4028725
- [13] Montazeri, M., Yavari, R., Rao, P., and Boulware, P., 2018, "In-Process Monitoring of Material Cross-Contamination Defects in Laser Powder Bed Fusion," *Journal of Manufacturing Science and Engineering*, **140**(11), pp. 111001-111001-111019. doi: 10.1115/1.4040543

- [14] Grasso, M., and Colosimo, B. M., 2017, "Process defects and in situ monitoring methods in metal powder bed fusion: a review," *Measurement Science and Technology*, p. 044005.
- [15] Zarreh, A., Saygin, C., Wan, H., Lee, Y., and Bracho, A., 2018, "Cybersecurity Analysis of Smart Manufacturing System Using Game Theory Approach and Quantal Response Equilibrium," *Procedia Manufacturing*, **17**, pp. 1001-1008. doi: 10.1016/j.promfg.2018.10.087
- [16] Malekipour, E., and El-Mounayri, H., 2018, "Common defects and contributing parameters in powder bed fusion AM process and their classification for online monitoring and control: a review," *The International Journal of Advanced Manufacturing Technology*, **95**(1), pp. 527-550. doi: 10.1007/s00170-017-1172-6
- [17] Malekipour, E., Tovar, A., and El-Mounayri, H., "Heat Conduction and Geometry Topology Optimization of Support Structure in Laser-Based Additive Manufacturing," Springer International Publishing, pp. 17-27.
- [18] Seifi, M., Gorelik, M., Waller, J., Hrabe, N., Shamsaei, N., Daniewicz, S., and Lewandowski, J. J., 2017, "Progress Towards Metal Additive Manufacturing Standardization to Support Qualification and Certification," *JOM*, **69**(3), pp. 439-455. doi: 10.1007/s11837-017-2265-2
- [19] Mazumder, J., 2015, "Design for metallic additive manufacturing machine with capability for "Certify as You Build"," *Procedia CIRP*, **36**, pp. 187-192. doi: 10.1016/j.procir.2015.01.009
- [20] Olakanmi, E. O., Cochrane, R., and Dalgarno, K., 2015, "A review on selective laser sintering/melting (SLS/SLM) of aluminium alloy powders: Processing, microstructure, and properties," *Progress in Materials Science*, **74**, pp. 401-477. doi: 10.1016/j.pmatsci.2015.03.002
- [21] Mies, D., Marsden, W., Dyer, S., and Warde, S., "Data-driven certification of additively manufactured parts," *Proc. Proceedings of 57th AIAA/ASCE/AHSIASC Structures, Structural Dynamics, and Materials Conference*.
- [22] Peralta, A. D., Enright, M., Megahed, M., Gong, J., Roybal, M., and Craig, J., 2016, "Towards rapid qualification of powder-bed laser additively manufactured parts," *Integrating Materials and Manufacturing Innovation*, pp. 1-23. doi: 10.1186/s40192-016-0052-5
- [23] Mazumder, J., and Song, L., 2013, "Advances in Direct Metal Deposition," *ASME International Mechanical Engineering Congress and Exposition San Diego, California*, p. V02AT02A012.
- [24] Schwalbe, M., 2016, *Predictive Theoretical and Computational Approaches for Additive Manufacturing: Proceedings of a Workshop*, National Academies Press.
- [25] Montazeri, M., and Rao, P., 2018, "Sensor-Based Build Condition Monitoring in Laser Powder Bed Fusion Additive Manufacturing Process Using a Spectral Graph Theoretic Approach," *Journal of Manufacturing Science and Engineering*, **140**(9), pp. 091002-091002-091016. doi: 10.1115/1.4040264

- [26] Malekipour, E., and El-Mounayri, H., "Defects, Process Parameters and Signatures for Online Monitoring and Control in Powder-Based Additive Manufacturing," Springer International Publishing, pp. 83-90.
- [27] Zhang, B., Li, Y., and Bai, Q., 2017, "Defect Formation Mechanisms in Selective Laser Melting: A Review," *Chinese Journal of Mechanical Engineering*, **30**(3), pp. 515-527. doi: 10.1007/s10033-017-0121-5
- [28] Khorasani, A. M., Gibson, I., Goldberg, M., and Littlefair, G., 2016, "A survey on mechanisms and critical parameters on solidification of selective laser melting during fabrication of Ti-6Al-4V prosthetic acetabular cup," *Materials & Design*, **103**, pp. 348-355. doi: 10.1016/j.matdes.2016.04.074
- [29] Sames, W. J., List, F., Pannala, S., Dehoff, R. R., and Babu, S. S., 2016, "The metallurgy and processing science of metal additive manufacturing," *International Materials Reviews*, **61**(5), pp. 315-360. doi: 10.1080/09506608.2015.1116649
- [30] Kempen, K., Thijs, L., Vrancken, B., Bols, S., Van Humbeeck, J., and Kruth, J., "Producing crack-free, high density M2 Hss parts by selective laser melting: pre-heating the baseplate," *Proc. Proceedings of the 24th international solid freeform fabrication symposium. Laboratory for freeform fabrication, Austin, TX*, pp. 131-139.
- [31] Sharratt, B. M., 2015, "Non-destructive techniques and technologies for qualification of additive manufactured parts and processes," Sharratt Research and Consulting Inc.
- [32] Montazeri, M., Nassar, A. R., Stutzman, C. B., and Rao, P., 2019, "Heterogeneous sensor-based condition monitoring in directed energy deposition," *Additive Manufacturing*, **30**, p. 100916. doi: 10.1016/j.addma.2019.100916
- [33] Beuth, J., and Klingbeil, N., 2001, "The role of process variables in laser-based direct metal solid freeform fabrication," *JOM*, **53**(9), pp. 36-39. doi: 10.1007/s11837-001-0067-y
- [34] Tang, M., Pistorius, P. C., and Beuth, J. L., 2017, "Prediction of lack-of-fusion porosity for powder bed fusion," *Additive Manufacturing*, **14**, pp. 39-48. doi: 10.1016/j.addma.2016.12.001
- [35] Gong, H., Rafi, K., Gu, H., Starr, T., and Stucker, B., 2014, "Analysis of defect generation in Ti-6Al-4V parts made using powder bed fusion additive manufacturing processes," *Additive Manufacturing*, **1**, pp. 87-98. doi: 10.1016/j.addma.2014.08.002
- [36] Gong, H., Rafi, K., Karthik, N., Starr, T., and Stucker, B., "Defect morphology in Ti-6Al-4V parts fabricated by selective laser melting and electron beam melting," *Proc. Proceedings of the Solid Freeform Fabrication Symposium*, pp. 12-14.
- [37] Vasinonta, A., Beuth, J. L., and Griffith, M., 2007, "Process maps for predicting residual stress and melt pool size in the laser-based fabrication of thin-walled structures," *Journal of Manufacturing Science and Engineering*, **129**(1), pp. 101-109. doi: 10.1115/1.2335852
- [38] Marrey, M., Malekipour, E., El-Mounayri, H., and Faierson, E. J., 2019, "A Framework for Optimizing Process Parameters in Powder Bed Fusion (PBF) Process Using Artificial Neural Network (ANN)," doi:

- [39] Chalancon, A., and Bourell, D., "Measured Energy Densities For Polyamide 12 And Comparison Of Values Calculated For Laser Sintering," Proc. Proceedings of the Solid Freeform Fabrication Symposium, Austin, Texas, USA, pp. 2217-2223.
- [40] Montazeri, M., Nassar, A. R., Dunbar, A. J., and Rao, P., 2019, "In-process monitoring of porosity in additive manufacturing using optical emission spectroscopy," IISE Transactions, pp. 1-16. doi: 10.1080/24725854.2019.1659525
- [41] Ferrar, B., Mullen, L., Jones, E., Stamp, R., and Sutcliffe, C., 2012, "Gas flow effects on selective laser melting (SLM) manufacturing performance," Journal of Materials Processing Technology, **212**(2), pp. 355-364. doi: 10.1016/j.jmatprotec.2011.09.020
- [42] Atzeni, E., and Salmi, A., 2015, "Study on unsupported overhangs of AlSi10Mg parts processed by Direct Metal Laser Sintering (DMLS)," Journal of Manufacturing Processes, **20**, pp. 500-506. doi: 10.1016/j.jmapro.2015.04.004
- [43] Strano, G., Hao, L., Everson, R., and Evans, K., 2013, "A new approach to the design and optimisation of support structures in additive manufacturing," The International Journal of Advanced Manufacturing Technology, **66**(9-12), pp. 1247-1254. doi: 10.1007/s00170-012-4403-x
- [44] Thomas, D., 2009, "The development of design rules for selective laser melting," Ph.D. Dissertation, University of Wales.
- [45] Thompson, M. K., Moroni, G., Vaneker, T., Fadel, G., Campbell, R. I., Gibson, I., Bernard, A., Schulz, J., Graf, P., and Ahuja, B., 2016, "Design for Additive Manufacturing: Trends, opportunities, considerations, and constraints," CIRP annals, **65**(2), pp. 737-760. doi: 10.1016/j.cirp.2016.05.004
- [46] Fox, J. C., Moylan, S. P., and Lane, B. M., 2016, "Effect of process parameters on the surface roughness of overhanging structures in laser powder bed fusion additive manufacturing," Procedia CIRP, **45**, pp. 131-134. doi: 10.1016/j.procir.2016.02.347
- [47] Amini, M., and Chang, S., 2018, "A review of machine learning approaches for high dimensional process monitoring," Proceedings of the 2018 IISE Annual Conference Orlando, FL.
- [48] Zarreh, A., Al Janahi, R., and Lee, Y., 2019, "Factors Contributing to Success in an Introductory Mechanical Engineering Course: A Data-Driven Case Study," doi:
- [49] Clijsters, S., Craeghs, T., Buls, S., Kempen, K., and Kruth, J.-P., 2014, "In situ quality control of the selective laser melting process using a high-speed, real-time melt pool monitoring system," The International Journal of Advanced Manufacturing Technology, **75**(5-8), pp. 1089-1101. doi: 10.1007/s00170-014-6214-8
- [50] Doubenskaia, M., Pavlov, M., Grigoriev, S., Tikhonova, E., and Smurov, I., 2012, "Comprehensive Optical Monitoring of Selective Laser Melting," Journal of Laser Micro/Nanoengineering, **7**(3) doi: 10.2961/jlmn.2012.03.001
- [51] Kanko, J. A., Sibley, A. P., and Fraser, J. M., 2016, "In situ morphology-based defect detection of selective laser melting through inline coherent imaging," Journal of Materials Processing Technology, **231**, pp. 488-500. doi: 10.1016/j.jmatprotec.2015.12.024
- [52] Li, Z., Zhang, Z., Shi, J., and Wu, D., 2019, "Prediction of surface roughness in extrusion-based additive manufacturing with machine learning," Robotics and

- Computer-Integrated Manufacturing, **57**, pp. 488-495. doi: 10.1016/j.rcim.2019.01.004
- [53] Zhang, W., Mehta, A., Desai, P. S., and Higgs, C., "Machine learning enabled powder spreading process map for metal additive manufacturing (AM)," Proc. Int. Solid Free Form Fabr. Symp. Austin, TX, pp. 1235-1249.
- [54] Gobert, C., Reutzel, E. W., Petrich, J., Nassar, A. R., and Phoha, S., 2018, "Application of supervised machine learning for defect detection during metallic powder bed fusion additive manufacturing using high resolution imaging," Additive Manufacturing, **21**, pp. 517-528. doi: 10.1016/j.addma.2018.04.005
- [55] Scime, L., and Beuth, J., 2018, "Anomaly detection and classification in a laser powder bed additive manufacturing process using a trained computer vision algorithm," Additive Manufacturing, **19**, pp. 114-126. doi: 10.1016/j.addma.2017.11.009
- [56] Shevchik, S. A., Kenel, C., Leinenbach, C., and Wasmer, K., 2018, "Acoustic emission for in situ quality monitoring in additive manufacturing using spectral convolutional neural networks," Additive Manufacturing, **21**, pp. 598-604. doi: 10.1016/j.addma.2017.11.012
- [57] GmbH, C. L., "Concept Laser AM Suit," <https://www.concept-laser.de/en/products/quality-management.html>.
- [58] EOS, "EOSTATE Monitoring Suit," <https://www.eos.info/software/monitoring-software/eostate-exposure-ot>.
- [59] Berman, A., and Plemmons, R. J., 1994, Nonnegative matrices in the mathematical sciences, SIAM.
- [60] Belkin, M., and Niyogi, P., 2003, "Laplacian eigenmaps for dimensionality reduction and data representation," Neural computation, **15**(6), pp. 1373-1396. doi: 10.1162/089976603321780317
- [61] Belkin, M., and Niyogi, P., 2004, "Semi-supervised learning on Riemannian manifolds," Machine learning, **56**(1-3), pp. 209-239. doi: 10.1023/B:MACH.0000033120.25363.1e
- [62] Shi, J., and Malik, J., 2000, "Normalized cuts and image segmentation," IEEE Transactions on Pattern Analysis and Machine Intelligence, pp. 888-905.
- [63] Meyer, C., 2000, Matrix analysis and applied linear algebra SIAM, Philadelphia, PA.
- [64] Jamshidinia, M., Boulware, P. C., Cronley, L., Marchal, J., and Mendoza, H., 2017, "Powder handling system for use in powder bed fusion additive manufacturing," Google Patents.
- [65] Boulware, P., 2016, "Final Technical Report to National Institute of Standards and Technology and National Center for Defense Manufacturing and Machining - Measurement Science Innovation Program for Additive Manufacturing ", Edison Welding Institute (EWI), Cincinnati, OH.
- [66] Jacobsmuhlen, J. z., Kleszczynski, S., Schneider, D., and Witt, G., "High resolution imaging for inspection of Laser Beam Melting systems," Proc. 2013 IEEE International Instrumentation and Measurement Technology Conference, IEEE, pp. 707-712.

- [67] Kleszczynski, S., Zur Jacobsmühlen, J., Sehart, J., and Witt, G., "Error detection in laser beam melting systems by high resolution imaging," Proc. Proceedings of the Twenty Third Annual International Solid Freeform Fabrication Symposium.
- [68] Foster, B., Reutzel, E., Nassar, A., Hall, B., Brown, S., and Dickman, C., "Optical, layerwise monitoring of powder bed fusion," Proc. Solid Free. Fabr. Symp. Proc, pp. 295-307.
- [69] Yao, B., Imani, F., Sakpal, A. S., Reutzel, E. W., and Yang, H., 2018, "Multifractal Analysis of Image Profiles for the Characterization and Detection of Defects in Additive Manufacturing," Journal of Manufacturing Science and Engineering, **140**(3), pp. 031014-031014-031013. doi: 10.1115/1.4037891
- [70] Chua, Z. Y., Ahn, I. H., and Moon, S. K., 2017, "Process monitoring and inspection systems in metal additive manufacturing: Status and applications," International Journal of Precision Engineering and Manufacturing-Green Technology, **4**(2), pp. 235-245. doi: 10.1007/s40684-017-0029-7
- [71] Rao, P. K., Liu, J. P., Roberson, D., Kong, Z. J., and Williams, C., 2015, "Online Real-time Quality Monitoring in Additive Manufacturing Processes using Heterogeneous Sensors," Journal of Manufacturing Science and Engineering, **37**(No. 6), pp. 1007-1001 – 1007-1012. doi: 10.1115/1.4029823
- [72] Huang, Y., and Leu, M., 2014, "Frontiers of Additive Manufacturing Research and Education—Report of NSF Additive Manufacturing Workshop."
- [73] Mani, M., Lane, B. M., Donmez, M. A., Feng, S. C., and Moylan, S. P., 2017, "A review on measurement science needs for real-time control of additive manufacturing metal powder bed fusion processes," International Journal of Production Research, **55**(5), pp. 1400-1418. doi: 10.1080/00207543.2016.1223378
- [74] Mani, M., Lane, B., Donmez, A., Feng, S., Moylan, S., and Fesperman, R., 2015, "NISTIR 8036: Measurement Science Needs for Real-time Control of Additive Manufacturing Powder Bed Fusion Processes," NIST, Gaithersburg, MD.
- [75] Liu, Q. C., Elambasseril, J., Sun, S. J., Leary, M., Brandt, M., and Sharp, P. K., "The effect of manufacturing defects on the fatigue behaviour of Ti-6Al-4V specimens fabricated using selective laser melting," Proc. Advanced Materials Research, Trans Tech Publ, pp. 1519-1524.
- [76] Nassar, A., and Reutzel, E., "A proposed digital thread for additive manufacturing," Proc. Proceedings of the Solid Freeform Fabrication Symposium
- [77] Betts, S., 2017, "Evaluation of Quality Signatures™ using In-Situ Process Control during Additive Manufacturing with Aluminum Alloy AlSi10Mg," Sigma Labs.
- [78] Cola, M., and Betts, S., 2018, "In-Situ Process Mapping using Thermal Quality Signatures™ during Additive Manufacturing with Titanium Alloy Ti-6Al-4V," Sigma Labs.
- [79] Repossini, G., Laguzza, V., Grasso, M., and Colosimo, B. M., 2017, "On the use of spatter signature for in-situ Monitoring of Laser Power Bed Fusion," Additive Manufacturing, **16**, pp. 35-48. doi: 10.1016/j.addma.2017.05.004

- [80] Craeghs, T., Clijsters, S., Kruth, J. P., Bechmann, F., and Ebert, M. C., 2012, "Detection of Process Failures in Layerwise Laser Melting with Optical Process Monitoring," *Physics Procedia*, **39**, pp. 753-759. doi: 10.1016/j.phpro.2012.10.097
- [81] Craeghs, T., Clijsters, S., Yasa, E., Bechmann, F., Berumen, S., and Kruth, J.-P., 2011, "Determination of geometrical factors in Layerwise Laser Melting using optical process monitoring," *Optics and Lasers in Engineering*, **49**(12), pp. 1440-1446. doi: 10.1016/j.optlaseng.2011.06.016
- [82] Tapia, G., and Elwany, A., 2014, "A Review on Process Monitoring and Control in Metal-Based Additive Manufacturing," *Transactions of the ASME, Journal of Manufacturing Science and Engineering*, **136**(6), p. 060801. doi: 10.1115/1.4028540
- [83] Foster, B. K., Reutzel, E. W., Nassar, A. R., Dickman, C. J., and Hall, B. T., "A brief survey of sensing for additive manufacturing," *Proc. SPIE Sensing Technology+ Applications*, International Society for Optics and Photonics, pp. 94890B-94890B-94810.
- [84] Purtonen, T., Kalliosaari, A., and Salminen, A., 2014, "Monitoring and Adaptive Control of Laser Processes," *Physics Procedia*, **56**, pp. 1218-1231. doi: 10.1117/12.184751
- [85] Everton, S. K., Hirsch, M., Stravroulakis, P., Leach, R. K., and Clare, A. T., 2016, "Review of in-situ process monitoring and in-situ metrology for metal additive manufacturing," *Materials & Design*, **95**, pp. 431-445. doi: 10.1016/j.matdes.2016.01.099
- [86] Popova, E., Rodgers, T. M., Gong, X., Cecen, A., Madison, J. D., and Kalidindi, S. R., 2017, "Process-Structure Linkages Using a Data Science Approach: Application to Simulated Additive Manufacturing Data," *Integrating Materials and Manufacturing Innovation*, **6**(1), pp. 54-68. doi: 10.1007/s40192-017-0088-1
- [87] Craeghs, T., Bechmann, F., Berumen, S., and Kruth, J.-P., 2010, "Feedback control of Layerwise Laser Melting using optical sensors," *Physics Procedia*, **5**, pp. 505-514. doi: 10.1016/j.phpro.2010.08.078
- [88] Kruth, J. P., Bartscher, M., Carmignato, S., Schmitt, R., De Chiffre, L., and Weckenmann, A., 2011, "Computed tomography for dimensional metrology," *CIRP Annals - Manufacturing Technology*, **60**(2), pp. 821-842. doi: 10.1016/j.cirp.2011.05.006
- [89] Kruth, J. P., Leu, M. C., and Nakagawa, T., 1998, "Progress in Additive Manufacturing and Rapid Prototyping," *CIRP Annals - Manufacturing Technology*, **47**(2), pp. 525-540. doi: 10.1016/S0007-8506(07)63240-5
- [90] Craeghs, T., Clijsters, S., Yasa, E., and Kruth, J.-P., "Online quality control of selective laser melting," *Proc. Proceedings of the Solid Freeform Conference*.
- [91] Amini, M., and Chang, S. I., 2018, "MLCPM: A process monitoring framework for 3D metal printing in industrial scale," *Computers & Industrial Engineering*, **124**, pp. 322-330. doi: 10.1016/j.cie.2018.07.041
- [92] Mahmoudi, M., 2019, "Process Monitoring and Uncertainty Quantification for Laser Powder Bed Fusion Additive Manufacturing."

- [93] Johnson, L., Mahmoudi, M., Zhang, B., Seede, R., Huang, X., Maier, J. T., Maier, H. J., Karaman, I., Elwany, A., and Arróyave, R., 2019, "Assessing printability maps in additive manufacturing of metal alloys," *Acta Materialia*, **176**, pp. 199-210. doi: 10.1016/j.actamat.2019.07.005
- [94] Gu, D., and Shen, Y., 2009, "Balling phenomena in direct laser sintering of stainless steel powder: Metallurgical mechanisms and control methods," *Materials & Design*, **30**(8), pp. 2903-2910. doi: 10.1016/j.matdes.2009.01.013
- [95] Gusarov, A. V., Yadroitsev, I., Bertrand, P., and Smurov, I., 2007, "Heat transfer modelling and stability analysis of selective laser melting," *Applied Surface Science*, **254**(4), pp. 975-979. doi: 10.1016/j.apsusc.2007.08.074
- [96] Chivel, Y., and Smurov, I., 2010, "On-line temperature monitoring in selective laser sintering/melting," *Physics Procedia*, **5**, pp. 515-521. doi: 10.1016/j.phpro.2010.08.079
- [97] Bayle, F., and Doubenskaia, M., "Selective laser melting process monitoring with high speed infra-red camera and pyrometer," *Proc. Fundamentals of laser assisted micro- and nanotechnologies*, International Society for Optics and Photonics, p. 698505.
- [98] Cheng, B., Lydon, J., Cooper, K., Cole, V., Northrop, P., and Chou, K., 2018, "Melt pool sensing and size analysis in laser powder-bed metal additive manufacturing," *Journal of Manufacturing Processes*, **32**, pp. 744-753. doi: 10.1016/j.jmapro.2018.04.002
- [99] Krauss, H., Eschey, C., and Zaeh, M., "Thermography for monitoring the selective laser melting process," *Proc. Proceedings of the 23rd Annual International Solid Freeform Fabrication Symposium*, edited by D. Bourell, R. Crawford, C. Seepersad, J. Beaman, and H. Marcus (The University of Texas at Austin, Austin, TX, 2012).
- [100] Krauss, H., Zeugner, T., and Zaeh, M. F., 2014, "Layerwise Monitoring of the Selective Laser Melting Process by Thermography," *Physics Procedia*, **56**, pp. 64-71. doi: 10.1016/j.phpro.2014.08.097
- [101] Lane, B., Moylan, S., Moylan, S., Whintont, E. P., Whintont, E. P., Ma, L., and Ma, L., 2016, "Thermographic measurements of the commercial laser powder bed fusion process at NIST," *Rapid prototyping journal*, **22**(5), pp. 778-787. doi: 10.1108/RPJ-11-2015-0161
- [102] Lane, B., Whintont, E., and Moylan, S., "Multiple sensor detection of process phenomena in laser powder bed fusion," *Proc. SPIE Commercial+ Scientific Sensing and Imaging*, International Society for Optics and Photonics, pp. 986104-986104-986109.
- [103] Lane, B., and Whintont, E., 2015, "Calibration and measurement procedures for a high magnification thermal camera," National Institute of Standards and Technology, Gaithersburg, MD, NIST Interagency/Internal Report (NISTIR)(submitted, awaiting publication) doi: 10.6028/NIST.IR.8098
- [104] Hammond, D. K., Vanderghenst, P., and Gribonval, R., 2011, "Wavelets on graphs via spectral graph theory," *Applied and Computational Harmonic Analysis*, **30**(2), pp. 129-150. doi: 10.1016/j.acha.2010.04.005

- [105] Sandryhaila, A., and Moura, J. M., 2013, "Discrete signal processing on graphs," *IEEE transactions on signal processing*, **61**, pp. 1644-1656. doi: 10.1109/TSP.2013.2238935
- [106] Shuman, D. I., Narang, S. K., Frossard, P., Ortega, A., and Vandergheynst, P., 2013, "The emerging field of signal processing on graphs: Extending high-dimensional data analysis to networks and other irregular domains," *IEEE Signal Processing Magazine*, **30**(3), pp. 83-98. doi: 10.1109/MSP.2012.2235192
- [107] Shuman, D. I., Ricaud, B., and Vandergheynst, P., "A windowed graph Fourier transform," *Proc. 2012 IEEE Statistical Signal Processing Workshop (SSP)*, Ieee, pp. 133-136.
- [108] Niyogi, P., and He, X., "Locality preserving projections," *Proc. Neural information processing systems*, MIT, p. 153.
- [109] Rao, P., Beyca, O., Bukkapatnam, S., Kong, Z. J., Case, K. E., and Komanduri, R., 2015, "A Graph Theoretic Approach for Quantification of Surface Morphology and its Application to Chemical Mechanical Planarization (CMP) Process," *IIE Transactions*, **47**(10), pp. 1088-1111. doi: 10.1080/0740817X.2014.1001927
- [110] Tootooni, M. S., Liu, C., Roberson, D., Donovan, R., Rao, P. K., Kong, Z. J., and Bukkapatnam, S. T., 2016, "Online non-contact surface finish measurement in machining using graph theory-based image analysis," *Journal of Manufacturing Systems*, **41**, pp. 266-276. doi: 10.1016/j.jmsy.2016.09.007
- [111] Tootooni, M. S., Fan, M., Sivasubramony, R. S., Rao, P., Chou, C.-A., and Miskovic, V., "Graph Theoretic Compressive Sensing Approach for Classification of Global Neurophysiological States from Electroencephalography (EEG) Signals," *Proc. Brain Informatics and Health (BIH)*.
- [112] Tootooni, M. S., Rao, P. K., Chou, C.-A., and Kong, Z., 2016, "A Spectral Graph Theoretic Approach for Monitoring Multivariate Time Series Data From Complex Dynamical Processes," *IEEE Transactions on Automation Science and Engineering* doi: 10.1109/TASE.2016.2598094
- [113] Rao, P. K., Kong, Z., Duty, C. E., and Smith, R. J., "Three Dimensional Point Cloud Measurement Based Dimensional Integrity Assessment for Additive Manufactured Parts Using Spectral Graph Theory," *Proc. ASME 2016 11th International Manufacturing Science and Engineering Conference*, American Society of Mechanical Engineers, pp. V002T004A048-V002T004A048.
- [114] Zhou, B., and Trinajstić, N., 2009, "On resistance-distance and Kirchhoff index," *Journal of mathematical chemistry*, pp. 283-289.
- [115] DeJesús, O., and Hagan, M. T., "Backpropagation through time for a general class of recurrent network," *Proc. 11th International Joint Conference on Neural Networks* Washington, D.C., pp. 2638-2642.
- [116] Crutchfield, J., Farmer, D., Packard, N., Shaw, R., Jones, G., and Donnelly, R. J., 1980, "Power spectral analysis of a dynamical system," *Physics Letters A*, **76**(1), pp. 1-4. doi: 10.1016/0375-9601(80)90130-9
- [117] Brandão, A., Gerard, R., Gumpinger, J., Beretta, S., Makaya, A., Pambaguian, L., and Ghidini, T., 2017, "Challenges in additive manufacturing of space parts: powder

- feedstock cross-contamination and its impact on end products," *Materials*, **10**(5), p. 522. doi: 10.3390/ma10050522
- [118] Montgomery, D. C., 2009, *Statistical quality control*, Wiley New York.
- [119] Tang, H. P., Qian, M., Liu, N., Zhang, X. Z., Yang, G. Y., and Wang, J., 2015, "Effect of Powder Reuse Times on Additive Manufacturing of Ti-6Al-4V by Selective Electron Beam Melting," *JOM*, **67**(3), pp. 555-563. doi: 10.1007/s11837-015-1300-4
- [120] Slotwinski, J. A., Garboczi, E. J., and Hebenstreit, K. M., 2014, "Porosity measurements and analysis for metal additive manufacturing process control," *Journal of research of the National Institute of Standards and Technology*, **119**, p. 494. doi: 10.6028/jres.119.019
- [121] Ardila, L., Garcíandia, F., González-Díaz, J., Álvarez, P., Echeverría, A., Petite, M., Deffley, R., and Ochoa, J., 2014, "Effect of IN718 recycled powder reuse on properties of parts manufactured by means of Selective Laser Melting," *Physics Procedia*, **56**, pp. 99-107. doi: 10.1016/j.phpro.2014.08.152
- [122] Clemon, L., 2017, "Material Quality and Process Monitoring in Metal Additive Manufacturing," University of California, Berkeley.
- [123] Spears, T. G., and Gold, S. A., 2016, "In-process sensing in selective laser melting (SLM) additive manufacturing," *Integrating Materials and Manufacturing Innovation*, **5**(1), pp. 16-40. doi: 10.1186/s40192-016-0045-4
- [124] Nassar, A. R., Reutzel, E. W., Brown, S. W., Morgan, J. P., Morgan, J. P., Natale, D. J., Tutwiler, R. L., Feck, D. P., and Banks, J. C., "Sensing for directed energy deposition and powder bed fusion additive manufacturing at Penn State University," *Proc. SPIE LASE*, SPIE, p. 14.
- [125] Abdelrahman, M., Reutzel, E. W., Nassar, A. R., and Starr, T. L., 2017, "Flaw detection in powder bed fusion using optical imaging," *Additive Manufacturing*, **15**, pp. 1-11. doi: 10.1016/j.addma.2017.02.001
- [126] Dunbar, A. J., and Nassar, A. R., 2018, "Assessment of optical emission analysis for in-process monitoring of powder bed fusion additive manufacturing," *Virtual and Physical Prototyping*, **13**(1), pp. 14-19. doi: 10.1080/17452759.2017.1392683
- [127] Stutzman, C. B., Nassar, A. R., and Reutzel, E. W., 2018, "Multi-sensor investigations of optical emissions and their relations to directed energy deposition processes and quality," *Additive Manufacturing*, **21**, pp. 333-339. doi: 10.1016/j.addma.2018.03.017
- [128] Berumen, S., Bechmann, F., Lindner, S., Kruth, J.-P., and Craeghs, T., 2010, "Quality control of laser- and powder bed-based Additive Manufacturing (AM) technologies," *Physics Procedia*, **5**, pp. 617-622. doi: 10.1016/j.phpro.2010.08.089
- [129] Kleszczynski, S., zur Jacobsmühlen, J., Reinartz, B., Sehrt, J. T., Witt, G., and Merhof, D., "Improving process stability of laser beam melting systems," *Proc. Fraunhofer Direct Digital Manufacturing Conference*.
- [130] Wegner, A., and Witt, G., "Process monitoring in laser sintering using thermal imaging," *Proc. SFF Symposium*, Austin, Texas, USA, pp. 8-10.

- [131] Rieder, H., Alexander, D., Spies, M., Bamberg, J., and Hess, T., "Online Monitoring of Additive Manufacturing Processes Using Ultrasound," Proc. 11th European Conference on Non-Destructive Testing (ECNDT 2014)
- [132] Tootooni, M. S., Dsouza, A., Donovan, R., Rao, P. K., Kong, Z., and Borgesen, P., 2017, "Classifying the Dimensional Variation in Additive Manufactured Parts from Laser-Scanned 3D Point Cloud Data using Machine Learning Approaches," ASME Transactions, Journal of Manufacturing Science and Engineering, **139**, no. 9 doi: 10.1115/1.4036641
- [133] Chung, F. R. K., 1997, Spectral Graph Theory, American Mathematical Society, Providence, RI.
- [134] Zhu, X., and Rabbat, M., "Graph spectral compressed sensing for sensor networks," Proc. IEEE International Conference on Acoustics, Speech and Signal Processing (ICASSP), IEEE, pp. 2865-2868.
- [135] Lee, J. D., and Maggioni, M., "Multiscale analysis of time series of graphs," Proc. Proceedings of The 9th International Conference on Sampling Theory and Applications, Singapore.
- [136] King, W. E., Anderson, A. T., Ferencz, R., Hodge, N., Kamath, C., Khairallah, S. A., and Rubenchik, A. M., 2015, "Laser powder bed fusion additive manufacturing of metals; physics, computational, and materials challenges," Applied Physics Reviews, **2**(4), p. 041304. doi: 10.1063/1.4937809
- [137] Hamilton, J. D., 1994, Time Series Analysis, Princeton University Press, Princeton, NJ.
- [138] Nassar, A., Spurgeon, T., and Reutzel, E., "Sensing defects during directed-energy additive manufacturing of metal parts using optical emissions spectroscopy," Proc. Solid Freeform Fabrication Symposium Proceedings, University of Texas Austin, TX.
- [139] Song, L., Bagavath-Singh, V., Dutta, B., and Mazumder, J., 2012, "Control of melt pool temperature and deposition height during direct metal deposition process," The International Journal of Advanced Manufacturing Technology, **58**(1), pp. 247-256. doi: 10.1007/s00170-011-3395-2
- [140] Mazumder, J., Dutta, D., Kikuchi, N., and Ghosh, A., 2000, "Closed loop direct metal deposition: art to part," Optics and Lasers in Engineering, **34**(4-6), pp. 397-414. doi: 10.1016/S0143-8166(00)00072-5
- [141] Mazumder, J., and Song, L., *Smart additive manufacturing system* Patent: [US20160052086A1](#).
- [142] Mazumder, J., Song, L., and Wang, C., *In-situ identification and control of microstructures produced by phase transformation of a material*, Patent: [US9752988B2](#).
- [143] Song, L., and Mazumder, J., *Real-time implementation of generalized predictive algorithm for direct metal deposition (DMD) process control*, Patent: [US9044827B2](#).
- [144] Canny, J., 1987, "A computational approach to edge detection," Readings in Computer Vision, Elsevier, pp. 184-203.
- [145] Yadollahi, A., Mahtabi, M., Khalili, A., Doude, H., and Newman Jr, J., 2018, "Fatigue life prediction of additively manufactured material: Effects of surface

- roughness, defect size, and shape," *Fatigue & Fracture of Engineering Materials & Structures*, **41**(7), pp. 1602-1614. doi: 10.1111/ffe.12799
- [146] Demuth, H. B., Beale, M. H., De Jesus, O., and Hagan, M. T., 2014, *Neural network design.*, PWS Publishing, Boston, MA.
- [147] Vetter, P., Engel, T., and Fontaine, J., "Laser cladding: the relevant parameters for process control," *Proc. Europto High Power Lasers and Laser Applications V*, International Society for Optics and Photonics, pp. 452-462.
- [148] Reutzel, E. W., and Nassar, A. R., 2015, "A survey of sensing and control systems for machine and process monitoring of directed-energy, metal-based additive manufacturing," *Rapid Prototyping Journal*, **21**(2), pp. 159-167. doi: 10.1108/RPJ-12-2014-0177
- [149] Hu, D., and Kovacevic, R., 2003, "Sensing, modeling and control for laser-based additive manufacturing," *International Journal of Machine Tools and Manufacture*, **43**(1), pp. 51-60. doi: 10.1016/S0890-6955(02)00163-3
- [150] Boddu, M. R., Landers, R. G., Musti, S., Agarwal, S., Ruan, J., and Liou, F. W., "System Integration and Real-Time Control Architecture of a Laser Aided Manufacturing Process 522," *Proc. 2002 International Solid Freeform Fabrication Symposium*.
- [151] Bartkowiak, K., 2010, "Direct laser deposition process within spectrographic analysis in situ," *Physics Procedia*, **5**, pp. 623-629. doi: 10.1016/j.phpro.2010.08.090
- [152] Song, L., and Mazumder, J., 2011, "Feedback Control of Melt Pool Temperature During Laser Cladding Process," *IEEE Transactions on Control Systems Technology*, **19**(6), pp. 1349-1356. doi: 10.1109/TCST.2010.2093901
- [153] Wang, Q., Li, J., Gouge, M., Nassar, A. R., Michaleris, P., and Reutzel, E. W., 2016, "Physics-Based Multivariable Modeling and Feedback Linearization Control of Melt-Pool Geometry and Temperature in Directed Energy Deposition," *Journal of Manufacturing Science and Engineering*, **139**(2), pp. 021013-021013-021012. doi: 10.1115/1.4034304
- [154] Bi, G., Sun, C. N., and Gasser, A., 2013, "Study on influential factors for process monitoring and control in laser aided additive manufacturing," *Journal of Materials Processing Technology*, **213**(3), pp. 463-468. doi: 10.1016/j.jmatprotec.2012.10.006
- [155] Bi, G., Schürmann, B., Gasser, A., Wissenbach, K., and Poprawe, R., 2007, "Development and qualification of a novel laser-cladding head with integrated sensors," *International Journal of Machine Tools and Manufacture*, **47**(3-4), pp. 555-561. doi: 10.1016/j.ijmachtools.2006.05.010
- [156] Khanzadeh, M., Chowdhury, S., Marufuzzaman, M., Tschopp, M. A., and Bian, L., 2018, "Porosity prediction: Supervised-learning of thermal history for direct laser deposition," *Journal of manufacturing systems*, **47**, pp. 69-82. doi: 10.1016/j.jmsy.2018.04.001
- [157] Suplee, C., 2009, "Atomic Spectra Database NIST, (2009)."
- [158] Samatova, N. F., Hendrix, W., Jenkins, J., Padmanabhan, K., and Chakraborty, A., 2013, *Practical graph mining with R*, CRC Press.